



**HAL**  
open science

# Alteration's Control on Frictional Behavior and the Depth of the Ductile Shear Zone in Geothermal Reservoirs in Volcanic Arcs

Barnaby Fryer, Florian Jermann, Patricia Patrier, Bruno Lanson, Stanislav Jelavić, Gabriel Meyer, Stephen E. Grasby, Marie Violay

► **To cite this version:**

Barnaby Fryer, Florian Jermann, Patricia Patrier, Bruno Lanson, Stanislav Jelavić, et al.. Alteration's Control on Frictional Behavior and the Depth of the Ductile Shear Zone in Geothermal Reservoirs in Volcanic Arcs. *Journal of Geophysical Research: Solid Earth*, 2025, 130 (2), 10.1029/2024JB030213 . hal-04916892

**HAL Id: hal-04916892**

**<https://hal.science/hal-04916892v1>**

Submitted on 28 Jan 2025

**HAL** is a multi-disciplinary open access archive for the deposit and dissemination of scientific research documents, whether they are published or not. The documents may come from teaching and research institutions in France or abroad, or from public or private research centers.

L'archive ouverte pluridisciplinaire **HAL**, est destinée au dépôt et à la diffusion de documents scientifiques de niveau recherche, publiés ou non, émanant des établissements d'enseignement et de recherche français ou étrangers, des laboratoires publics ou privés.



Distributed under a Creative Commons Attribution 4.0 International License

1 **Alteration's control on frictional behavior and the depth**  
2 **of the ductile shear zone in geothermal reservoirs in**  
3 **volcanic arcs**

4 **Barnaby Fryer<sup>1</sup>, Florian Jermann<sup>1\*</sup>, Patricia Patrier<sup>2</sup>, Bruno Lanson<sup>3</sup>,**  
5 **Stanislav Jelavic<sup>3</sup>, Gabriel Meyer<sup>1</sup>, Stephen E. Grasby<sup>4</sup>, Marie Violay<sup>1</sup>**

6 <sup>1</sup>Laboratory of Experimental Rock Mechanics, École Polytechnique Fédérale de Lausanne, Lausanne,  
7 Switzerland

8 <sup>2</sup>Département Géosciences, Université de Poitiers, Poitiers, France

9 <sup>3</sup>Univ. Grenoble Alpes, USMB, CNRS, IRD, UGE, ISTerre, France

10 <sup>4</sup>Geological Survey of Canada, 3303 33rd Street NW Calgary, AB T2L-2A7, Canada

11 **Key Points:**

- 12 • Collective phyllosilicate content controls the first-order friction behaviour of an-
- 13 desitic samples from geothermal fields in volcanic arcs
- 14 • Negative frictional healing is observed and thought to be related to the presence
- 15 of expandable clays
- 16 • The transition to a ductile shear zone in volcanic-arc settings is influenced by al-
- 17 teration's control on frictional strength

18 **Key Words:**

- 19 • 8135 Hydrothermal systems
- 20 • 8185 Volcanic arcs
- 21 • 3653 Fluid flow
- 22 • 3617 Alteration and weathering processes
- 23 • 7280 Volcano seismology

---

\*Currently affiliated with BTG Büro für Technische Geologie AG

Corresponding author: Barnaby Fryer, [barnaby.fryer@geoazur.unice.fr](mailto:barnaby.fryer@geoazur.unice.fr)

## Abstract

The majority of geothermal energy is produced in tectonically-active volcanic-arc regions due to their high geothermal gradients. Reservoirs in these settings are often stratified with smectite/kaolinite-, illite-, and chlorite-rich zones, in order of increasing depth and temperature. Eighteen andesitic core and surface samples were taken from five geothermal fields in the Lesser-Antilles and Cascade volcanic arcs. The collected samples have experienced various degrees of alteration and can be considered, in their ensemble, to be representative of the previously-mentioned alteration zones. The influence of the alteration was assessed through biaxial rate-and-state friction experiments on prepared gouge. The samples were each tested at 10, 30, and 50 MPa normal stress in both nominally-dry and nominally-wet conditions. While significant water-induced frictional-strength reduction was observed, phyllosilicate content dominates frictional behaviour, with increased phyllosilicate content reducing frictional strength, promoting velocity-strengthening behaviour, and reducing frictional healing. Negative frictional healing is observed and likely related to the presence of expandable clays, leading to frictional weakness over long time periods. It is suggested that, by controlling frictional strength, phyllosilicate content influences the depth of onset of ductile shear zones, which often underlie these reservoirs and are critical for the horizontal advection and vertical sealing of geothermal fluid. Further, as these types of reservoirs are likely critically stressed, varying degrees of alteration within different reservoir zones can give rise to the formation of stress jumps. Overall, the frictional behavior depended to a first order on overall phyllosilicate content, potentially simplifying engineering studies.

## Plain Language Summary

Altered andesitic core and surface samples were taken from five geothermal fields in volcanic arc environments. The alteration has resulted in the formation of clay-like (phyllosilicate) minerals. Through a large number of friction experiments, it is shown that the amount of clay-like minerals controls frictional properties, irrespective of the specific clay-like minerals present, potentially simplifying induced seismicity studies if all clay-like minerals might be treated frictionally as one species. Increased clay-like mineral content decreases frictional strength (making faults weaker), promotes stable sliding (meaning faults are unlikely to nucleate an earthquake), and reduces frictional healing (meaning faults recover strength slowly). The unusual phenomenon of fault weakening during seismic stasis (negative frictional healing) is also occasionally observed and linked to clay-like minerals. Further, reservoirs in these settings are often rooted in distributed (ductile) shear zones which facilitate horizontal fluid movement. It is suggested that the extent to which clay-like minerals have formed will influence the depth at which this distributed shear zone begins. Finally, it is suggested that the reduced frictional strength of clay-like-mineral-rich zones may lead to the formation of sharp stress changes between highly- and un-altered zones, indicating a strong control of alteration on fracture propagation.

## 1 Introduction

As geothermal energy production greatly benefits from a high geothermal gradient, the preponderance of global geothermal electricity production is located near tectonically-active volcanic- or, equivalently, magmatic-arc regions (Stelling et al., 2016). Some examples include Cerro Pabellón, Chile (Maza et al., 2018), Tolhuaca Geothermal Field, Chile (Melosh et al., 2010), the Awibengkok Geothermal System, Indonesia (Stimac et al., 2008), Darajat, Indonesia (Rejeki et al., 2010), the Ogiri Field, Japan (Goko, 2000), the Copahue Geothermal Reservoir, Argentina-Chile (Barcelona et al., 2019), Los Azufres, Mexico (Cathelineau & Izquierdo, 1988), Bouillante, France (Jaud & Lamethe, 1985), Newberry, USA (MacLeod & Sammel, 1982), and Mount Meager, Canada (Jessop, 2008).

74 These systems located in volcanic- or, in many cases, specifically andesitic-arcs repre-  
75 sent a significant proportion of global geothermal energy production (Stelling et al., 2016).

76 However, our understanding of the structure, fluid pathways, and history of these  
77 reservoirs is generally poor (e.g., Bouchot et al. (2010); Favier, Lardeaux, Corsini, et al.  
78 (2021)). Secondary permeability is thought to be a key factor in the productive poten-  
79 tial of such geothermal systems (Stelling et al., 2016) and is often governed by fractures  
80 and faults in these contexts (Curewitz & Karson, 1997; Goko, 2000; Stimac et al., 2008;  
81 Navelot et al., 2018; Jolie et al., 2021; Favier, Lardeaux, Corsini, et al., 2021). The flu-  
82 ids that flow through these discontinuities often cause the hydrothermal alteration of the  
83 surrounding rock due to chemical disequilibrium (Fenner, 1934; Browne, 1978; Frolova  
84 et al., 2014). As alteration, while dependent on fluid-to-rock (F/R) mass ratio and the  
85 degree of disequilibrium, is strongly dependent on temperature, which often varies di-  
86 rectly with depth, it is not uncommon for alteration to occur in temperature-delimited  
87 zones, albeit with this zonation often appearing during the cooling of the system. For  
88 example, smectite and kaolinite form at relatively low temperatures and therefore gener-  
89 ally form a shallow alteration zone, at times overprinting previous high-temperature  
90 alteration (e.g., Patrier et al. (1997)). Below this, at slightly higher temperatures an illite-  
91 rich or mixed-layer zone may have previously formed. Deeper still, at again higher tem-  
92 peratures, a chlorite-rich alteration zone may be present. The combination of these three  
93 zones leads to a typical geothermal reservoir structure with a smectite/kaolinite zone over-  
94 lying an illite-rich zone, which in turn overlies a chlorite-rich zone (e.g., Cathelineau and  
95 Izquierdo (1988); Mas et al. (2006); Sillitoe (2010); Stimac et al. (2015)). Of course, many  
96 other alteration products will likely form in such reservoirs and the zones themselves may  
97 not be marked by sharp boundaries such that transitions are common. Note, addition-  
98 ally, that it is common to find strong lateral variations of temperature and alteration fa-  
99 cies in these contexts. At any rate, alteration and the formation of secondary minerals  
100 can significantly impact the permeability and porosity of fluid pathways and may lead,  
101 for example, to the zone rich in smectite and kaolinite forming a clay cap, preventing the  
102 loss of heated fluids to the surface through advection (Frolova et al., 2010, 2014; Wyr-  
103 ington et al., 2014; Navelot et al., 2018).

104 Frictional sliding can result in such phenomena as cataclasis and gouge formation,  
105 dilation, and cracking; all of which can have meaningful implications for fluid flow. Ad-  
106 ditionally, considering the high geothermal gradient present in most geothermal fields,  
107 the transition in mode and mechanism of deformation can be anomalously shallow in these  
108 regions (Lucchitta, 1990; Cameli et al., 1993; Ranalli & Rybach, 2005). The "ductile"  
109 shear zones of distributed deformation at the base of many geothermal fields (e.g., Stimac  
110 et al. (2015); Yagupsky et al. (2023)) may serve as a foundation for the sub-vertically-  
111 oriented faults within the reservoir, and act as zones providing horizontal fluid transport  
112 (Knipe & McCaig, 1994; Kohlstedt et al., 1995; Verati et al., 2018; Favier et al., 2019;  
113 Favier, Lardeaux, Corsini, et al., 2021), while acting as vertical seals (Stimac et al., 2015),  
114 Figure 1. The depth of this zone will depend, in part, on the frictional strength of the  
115 rock (Griggs, 1936; Paterson, 1958; Byerlee, 1968; Kohlstedt et al., 1995; Ranalli & Ry-  
116 bach, 2005; Violay et al., 2012; Meyer et al., 2019; Meyer & Violay, 2023). Therefore,  
117 an understanding of how the frictional behaviour of these rocks may change and develop  
118 in these settings throughout the life of the system is important for reconstructing the  
119 entire history of the reservoir, which can in turn improve the exploration process within  
120 that specific field, in particular as these fields have a tendency to migrate and often have  
121 non-monotonic temperature profiles, resulting in potentially hidden high-temperature  
122 zones (e.g., Mas et al. (2003, 2006)). It is further crucial to understand how these faults  
123 control the state of stress of the field and how they respond to engineering operations  
124 influencing stress and pore pressure conditions.

125 Further, geothermal projects have often been burdened by instances of induced seis-  
126 micity. For example, induced seismic events in Basel, Switzerland (Häring et al., 2008),

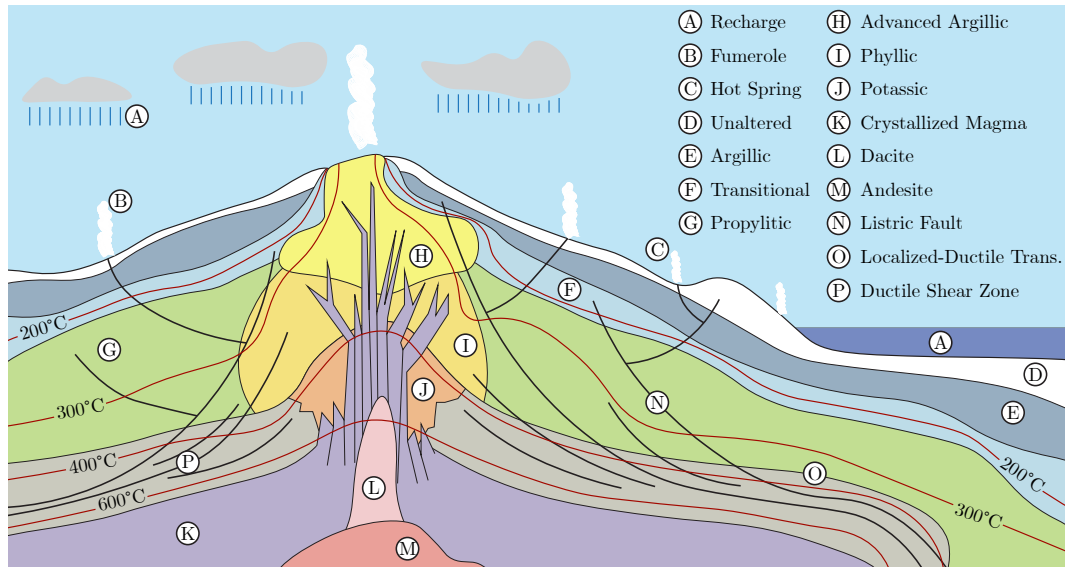


**Figure 1.** A representative example of a volcanic arc system, based on Richards (2011); Stimać et al. (2015); Revil and Gresse (2021). The argillic zone (E) may contain smectite, kaolinite, and/or illite, may overprint higher-temperature alteration, and may act as a clay cap. Propylitic alteration (G) may produce chlorite. Due to a high geothermal gradient, the onset of ductile deformation (i.e., the Localized-to-Ductile Transition) is found at a relatively shallow depth (O) and leads to the formation of a ductile shear zone (P). This zone is comprised of laterally-extensive fractures that connect to listric-like faults and allows for the lateral transfer of fluids, while acting as a vertical seal. As depth and temperature increase, deformation mechanisms shift from brittle to plastic. The onset of this second transition may occur within the ductile shear zone or outside of it. Note that the original *in-situ* rocks may be many different types of volcanic rock (e.g., tuff, ash, lava, etc.) depending on the deposition history of the region. The schematic is not to scale.

127 St. Gallen, Switzerland (Obermann et al., 2015), Darajat Geothermal Field, Indonesia  
 128 (Pramono & Colombo, 2005), Soultz-sous-Forêts, France (Dorbath et al., 2009), and Po-  
 129 h-ang, South Korea (Kim et al., 2018) have in some cases led to significant project dif-  
 130 ficulties. Therefore, an understanding of the frictional properties of rocks is relevant to  
 131 prevent unwanted seismicity and better understand how a reservoir responds to shear  
 132 stimulation, a stimulation technique often applied to Enhanced Geothermal Systems. This  
 133 is particularly true in the case of volcanic arcs, where seismicity may at times be capa-  
 134 ble of inducing debris avalanches (Keefer, 1984; Siebert, 1984) or threatening the integrity  
 135 of the clay cap (Yamaya et al., 2013).

136 Here, 18 samples (15 core samples and 3 surface samples) are collected from two  
 137 volcanic arcs relevant for geothermal energy exploration and exploitation: the Lesser An-  
 138 tilles and Cascade volcanic arcs. The samples are generally andesitic in nature and have  
 139 undergone a wide range of alteration. A general overview of the samples is provided in  
 140 Table 1. Gouges are prepared from the samples and their frictional behaviours are tested  
 141 in a biaxial apparatus in the rate-and-state friction framework (Dieterich, 1979; Ruina,  
 142 1983). It is found that alteration has the potential to significantly influence the friction  
 143 coefficient, velocity-dependence, and inter-seismic healing of this rock type, having con-  
 144 sequences in these settings for geothermal-reservoir-history reconstruction and fluid flow  
 145 (because friction coefficient is related to the depth of onset of any ductile shear zone),  
 146 in-situ stresses (because the stress state is influenced by the friction coefficients along  
 147 critically-stressed faults), and induced seismicity (because friction coefficient, velocity  
 148 dependence, and healing all influence the seismic response of faults).

## 149 2 Sample Sourcing

### 150 2.1 The Lesser Antilles Volcanic Arc

151 The Lesser Antilles form an island volcanic arc and are a result of the subduction  
 152 of the North and South American plates underneath the Caribbean Plate at approxi-  
 153 mately 20 mm per year (Deng & Sykes, 1995; DeMets et al., 2010). The Lesser Antilles  
 154 are home to a number of active volcanoes, Figure 2a, and are considered to have geothermal-  
 155 energy production potential. Despite this, geothermal energy production is currently only  
 156 operative in Guadeloupe, in the Bouillante geothermal field. Other islands, such as Mar-  
 157 tinique, have seen the drilling of a number of exploratory wells. Cores from these wells  
 158 and surface samples from Guadeloupe will be used in this study as representative of the  
 159 potential geothermal systems of the Lesser Antilles.

160 Terre-de-Haut, an island belonging to the Guadeloupe Archipelago, Figure A1, is  
 161 primarily composed of andesitic rocks (Jacques & Maury, 1988), a typical composition  
 162 for the recently-active arc in the Lesser Antilles (Navelot et al., 2018). As with the cur-  
 163 rent Bouillante system, the paleo-geothermal system in the central part of Terre-de-Haut  
 164 is associated with the intersection of two major fault systems (Verati et al., 2016). As  
 165 surface samples from Les Saintes can be considered as analogues to *in-situ* Bouillante  
 166 geothermal reservoir rock (Verati et al., 2016; Navelot et al., 2018; Favier, Lardeaux, Ve-  
 167 rati, et al., 2021), three such samples were used for this study, taken from the center of  
 168 Terre-de-Haut, near Grande Anse, which is comprised of highly-altered andesite (Jacques  
 169 & Maury, 1988; Navelot et al., 2018). Note that, due to this alteration, it is difficult to  
 170 know if these samples were originally lavas, debris, or pyroclastic flows (Jacques & Maury,  
 171 1988; Favier, Lardeaux, Corsini, et al., 2021); however, lavas sampled in this region are  
 172 generally in the basalt-andesite to dacite range (Verati et al., 2016; Favier, Lardeaux,  
 173 Corsini, et al., 2021). These samples will be referred to as S491B, S491I, and B494D.

174 Located on the center-west side of Martinique, the Plain of Lamentin is an allu-  
 175 vial plain surrounded by older volcanic highlands and lain down on a volcanic substratum  
 176 (Mas et al., 2003; Gadalia et al., 2014), Figure A2. The reservoir of Lamentin is cut

177 by large, widespread, and often steeping-dipping normal faults (Genter et al., 2002; Gadalia  
 178 et al., 2014). These faults are thought to be the conduits through which mantle-derived  
 179 gases reach the Lamentin reservoir and even the surface (Gadalia et al., 2019). It is not  
 180 uncommon to find alteration minerals such as kaolinite, chlorite, and calcite within cores  
 181 taken from zones transected by faults (Genter et al., 2002). On the basis of clay-mineral  
 182 signatures and  $\alpha$ -spectrometry, it is thought that the system presented temperatures greater  
 183 than 200°C as recently as 250,000 years ago (Mas et al., 2003; Gadalia et al., 2019). It  
 184 currently presents much more moderate temperatures, less than 100°C. In this study,  
 185 the cores from the LA02 (Carrère) well were taken from 422 m, 541.55 m, and 767.8 m  
 186 and will be referred to as LA02422, LA02541, and LA02767, respectively. Further, two  
 187 cores from the LA03 (Californie) well are studied here from depths of 749.8 m and 758.2  
 188 m and will be referred to as LA03749 and LA03758, respectively. Both of these cores are  
 189 from moderately to slightly fractured zones with calcite fillings (Genter et al., 2002). Fur-  
 190 further information on the field histories of Lamentin and Les Saintes can be found in Ap-  
 191 pendices A01 and A02. Sample photos can be found in Supplementary Material, Fig-  
 192 ures S1-S2.

## 193 **2.2 The Cascade Volcanic Arc**

194 The Cascade Volcanic Arc is located in the Northwestern United States and South-  
 195 western Canada. This continental volcanic arc is related to the spreading of the Juan  
 196 de Fuca Ridge and the subduction of the Juan de Fuca Plate under the North Ameri-  
 197 can Plate (Jessop, 2008). The Cascade Volcanic Arc is home to a number of active vol-  
 198 canoes, Figure 2b, and is considered to have significant geothermal-energy production  
 199 potential. In particular, Mount Meager in Canada and the Newberry Volcano EGS Demon-  
 200 stration Project are thought to represent promising candidates for geothermal energy  
 201 production, and both have been drilled and cored. Further exploration has also occurred  
 202 farther inland in the Summerland Basin, but this resource is likely low enthalpy.

203 Mount Meager is a volcanic complex located in southwest British Columbia in the  
 204 Garibaldi Volcanic Belt, Figure A3. For this study, a core sample of diorite was taken  
 205 from well M-17, drilled across the southern flank of Pylon Peak (Jessop, 2008), in the  
 206 interval from 433.4 m to 437.1 m (1422 ft to 1434 ft). This sample will be referred to as  
 207 M1430.

208 The Summerland Basin is an Eocene volcanic caldera located in the Okanagan Val-  
 209 ley of British Columbia, Figure A4, and has been interpreted to be composed of accreted  
 210 oceanic and island arcs as part of the Intermontane Belt of the Canadian Cordillera (Monger  
 211 & Irving, 1980; Church et al., 1990). The Summerland Basin comprises several major  
 212 units; of particular importance here are the massive volcanic beds of the Marron For-  
 213 mation, principally comprised of alternating ash and lava flows which are largely con-  
 214 tinuous despite being offset by faulting (Michel et al., 2002; Jessop, 2008). For the study  
 215 being performed here, samples were taken from 810.3 m (2658.5 ft), 819.9 m (2690 ft),  
 216 915.9 m (3005 ft), and 954.0 m (3130 ft). These samples will be referred to as G2658,  
 217 G2690, G3005, and G3130, with the numerical portion of the name corresponding to the  
 218 sample depth in feet. All four samples are part of the Marron Formation's Kitley Lake  
 219 Member, which is predominantly composed of chloritized amygdaloidal porphyritic tra-  
 220 chyandesite. While G2658 is considered to be fairly fresh trachyandesite, the rest of these  
 221 samples have undergone alteration. G2690 displays pink oxidation, whereas G3005 has  
 222 undergone carbonate-rich alteration and is light green in color. G3130 is dark green and  
 223 is chloritic clay rich.

224 The Newberry Volcano, Figure A5, is located 60 km east of the Cascade range in  
 225 central Oregon, covers an area of 1200 km<sup>2</sup>, and has been active as recently as 1,300 years  
 226 ago (MacLeod & Sammel, 1982; MacLeod & Sherrod, 1988). While the composition of  
 227 its rocks varies widely at depth, it is thought that it is underlain by a rhyolitic magma

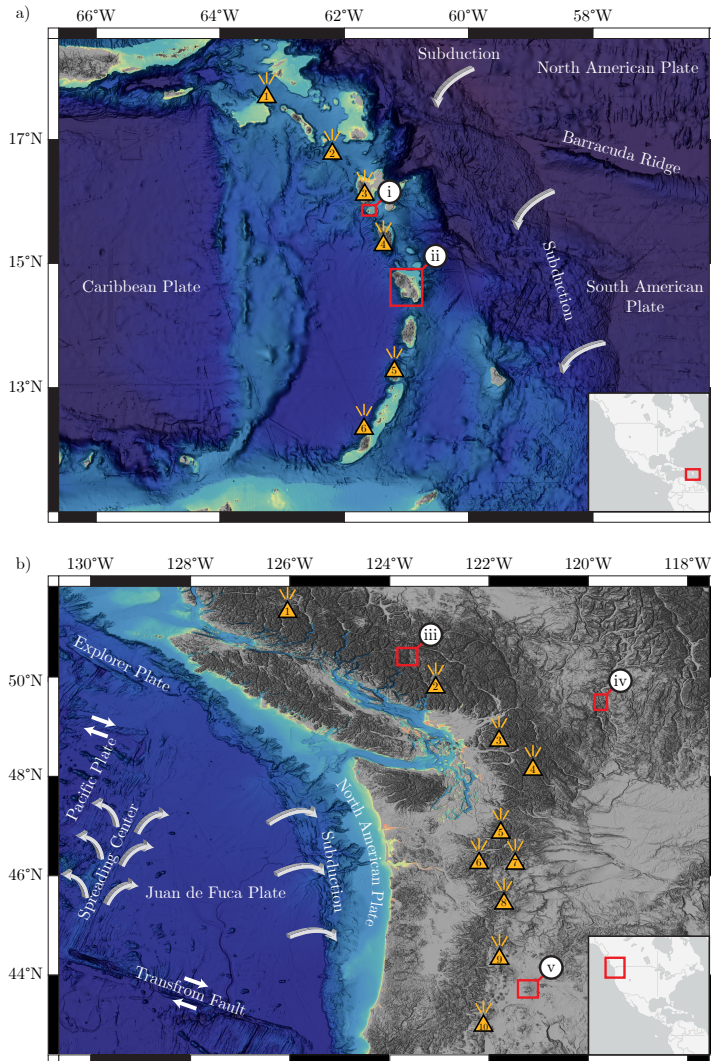


**Figure 2.** The geodynamic contexts of the samples. Detailed geological maps are given in Appendix A. a) A map of the Lesser Antilles Volcanic Arc. Sample sourcing locations are denoted by red boxes, with (i) corresponding to Les Saintes, and (ii) to Lamentin. The listed volcanoes, denoted by orange triangles, are all likely to have been active in the last 11,700 years (Holocene) (Global Volcanism Program, 2024), with the numbers corresponding to (1) Mount Scenery, (2) Soufrière Hills (Montserrat), (3) La Grande Soufrière, (4) Morne Plat Pays, (5) La Soufrière (Saint Vincent), and (6) Kick'em Jenny. These volcanoes are generally related to the subduction of the North and South American plates underneath the Caribbean Plate. b) A map of the Cascade Volcanic Arc. Core samples are taken from locations denoted by the red boxes, with (iii) corresponding to Mount Meager, (iv) Summerland Basin, and (v) to Newberry. The listed volcanoes, denoted by orange triangles, are all likely to have been active in the last 11,700 years (Holocene) (Global Volcanism Program, 2024), with the numbers corresponding to (1) Silverthorne Caldera, (2) Mount Garibaldi, (3) Mount Baker, (4) Glacier Peak, (5) Mount Rainier, (6) Mount St. Helens, (7) Mount Adams, (8) Mount Hood, (9) the Three Sisters, (10) Crater Lake. These volcanoes are generally related to the subduction of the Juan de Fuca Plate underneath the North American Plate. Also shown is the spreading center between the Juan de Fuca and Pacific Plates (i.e., the Juan de Fuca Ridge). The ETOPO 2022 Global Relief Model is used as the base map (NOAA National Centers for Environmental Information, 2022).



**Table 1.** A summary of the samples used for this study. The rock types are taken from Verati et al. (2016); Favier, Lardeaux, Corsini, et al. (2021) for Les Saintes and Mas et al. (2003) for Lamentin; otherwise they are unpublished. Ba is basalt, An is andesite, Dac is dacite, and TrAn is trachyandesite. Depths are measured depths. The temperature,  $T$ , data are taken from Mas et al. (2003) for Lamentin wells, Ghomshei et al. (2004) for Mount Meager, Jessop (2008) for Summerland Basin (based on a linear interpolation of temperature measurements taken at 706 and 946.5 meters depth), and Walkey and Swanberg (1990) for Newberry. Note that these are the modern temperatures for these reservoirs. The predominant alteration type (Pred. Alt. Type) and phyllosilicate content by weight (Phyll.) are given in the last two columns and are based on XRD results (shown in more detail later, see Section 5.1.2), with predominant alteration type noting the principal category of secondary phyllosilicate mineral present. Intermediate means that no one phyllosilicate mineral is responsible for more than 67% of the phyllosilicate minerals present.

Sample	Location (well name)	Rock Type	Depth [m]	$T$ [°C]	Pred. Alt. Type	Phyll. [%]
B494D	Les Saintes (surface)	Ba/An-Dac	-	-	Smectite	23
S491I	Les Saintes (surface)	Ba/An-Dac	-	-	Smectite	29
S491B	Les Saintes (surface)	Ba/An-Dac	-	-	Illite	49
LA02422	Lamentin (LA02)	An	442.0	49	Intermediate	51
LA02541	Lamentin (LA02)	An	541.6	47	Intermediate	44
LA02767	Lamentin (LA02)	An	767.8	47 <sup>b</sup>	Chlorite	10
LA03749	Lamentin (LA03)	An <sup>a</sup>	749.8	77	Al-smectite/Kaolinite	62
LA03758	Lamentin (LA03)	An	758.2	77	Intermediate	19
M1430	Mount Meager (M-17)	Diorite	≈435	167	Intermediate	21
G2658	Summerland Basin (GSC495)	TrAn	810.3	37	Mg-smectite	15
G2690	Summerland Basin (GSC495)	TrAn	819.9	37	Chlorite	17
G3005	Summerland Basin (GSC495)	TrAn	915.9	40	Chlorite	15
G3130	Summerland Basin (GSC495)	TrAn	954.0	41	Chlorite	20
N3583	Newberry (GEO N-2)	Ba-Ba/An	1092.3	134	Mg-smectite	24
N3808	Newberry (GEO N-2)	Ba-Ba/An	1160.7	143	Mg-smectite	22
N4330	Newberry (GEO N-2)	Ba-Ba/An	1319.8	163	Mg-smectite	15
N4343	Newberry (GEO N-2)	Ba-Ba/An	1323.7	164	Intermediate	20
N4422	Newberry (GEO N-2)	Ba-Ba/An	1348.0	166 <sup>c</sup>	Mg-smectite	18

<sup>a</sup> This sample is heavily altered and from a fault zone. The original rock type cannot be stated with certainty. See Genter et al. (2002).

<sup>b</sup> The last depth for which temperature was recorded for this well was 724 m.

<sup>c</sup> The last depth for which temperature was recorded for this well was 1346 m.

228 chamber of approximately 5 km in diameter (MacLeod & Sherrod, 1988). Interest in this  
 229 region is related in particular to an exploration well (USGS N-2) completed in 1981, where  
 230 a temperature of 265°C was encountered at 932 m (MacLeod & Sammel, 1982). For the  
 231 study being performed here, samples were taken from the GEO N-2 (not the USGS N-  
 232 2) well at 1092.3 m (3583.5 ft), 1160.7 m (3808 ft), 1319.8 m (4330 ft), 1323.7 m (4343  
 233 ft), and 1348.0 m (4422.5 ft). These samples will be referred to as N3583, N3808, N4330,  
 234 N4343, and N4422, with the numerical portion of the name corresponding to the sam-  
 235 ple depth in feet. These samples are basaltic to basaltic-andesitic in composition with  
 236 varying degrees of alteration. Further information on the field histories of Mount Mea-  
 237 ger, Summerland Basin, and Newberry can be found in Appendices A03-A05. Sample  
 238 photos can be found in Supplementary Material, Figures S3-S5.

### 3 Methods

#### 3.1 Sample preparation

The samples were first photographed and then cut into more manageable pieces. Two cut pieces of each sample were analysed with X-ray Diffraction (XRD) and as thin sections. The remaining sample material was crushed by hand with first a hammer and then an agate mortar and pestle. Finally, the prepared gouge was passed through a sieve to ensure a particle size of less than 125  $\mu\text{m}$ , later confirmed by granulometry, Supplementary Material, Table S6. The samples were never oven dried to avoid altering the clays present in the sample (Summers & Byerlee, 1977). One gram of each sample was ground with 15 ml of ethanol for 10 minutes using the McCrone mill equipped with agate grinding elements to ensure a nominal average particle size of 1  $\mu\text{m}$ , important for the quantitative phase analysis.

#### 3.2 Sample characterization

##### 3.2.1 Microstructure

Thin sections were prepared by Thin Section Lab and the Institute of Earth Sciences at the Université de Lausanne from virgin samples and then carbon coated and analyzed using scanning electron microscopes (SEMs) at the University of Poitiers (JEOL JSM IT500) and the Ecole Polytechnique Fédérale de Lausanne. These samples were viewed using back-scattered electrons, illustrating density contrasts. In addition, energy-dispersive X-ray spectrometry (EDX) was used to evaluate the mass percentages of elements present in different minerals in the samples. This was then used to calculate the structural formulae of the minerals, which, in conjunction with the density contrasts and particle morphology, led to mineral identification. Specifically, the SEM was equipped with a Bruker Lynxeye EDX spectrometer with a XFlash 4030 Silicon drift detector. The analytical conditions for quantitative EDX analysis were as follows: acceleration voltage 15 kV, current beam 1 nA, counting time 50 s, working distance 11 mm. The standards used for the EDX quantitative analysis consisted of albite (Na, Al, Si), almandine (Mg, Fe), diopside (Ca), orthoclase (K) and spessartite (Mn). Matrix corrections were performed using the Phi-Rho-Z correction.

##### 3.2.2 X-ray Diffraction (XRD) and Quantitative Phase Analysis (QPA)

XRD data was collected on randomly-oriented powders using a Bruker D8 Advance diffractometer operating in Bragg-Brentano geometry and using  $\text{CoK}\alpha$  radiation ( $\lambda = 1.7902 \text{ \AA}$ ; 40 kV – 35 mA). Data was collected from 5-90°  $2\theta$ , counting 6s per 0.026° step. Following identification of the crystalline phases, sample mineralogy was assessed quantitatively with the Rietveld program BGMN and the Profex user-interface (Doebelin & Kleeberg, 2015). Clay minerals were grouped by families (kaolinite, micas, and swelling 2:1). Swelling 2:1 minerals include both discrete smectite and smectite-containing mixed layers (e.g., chlorite/smectite or corrensite). When both species coexist, XRD data was fit using smectite contributions with contrasting hydration states to reproduce the positions of basal reflections. The tri- or di-octahedral character of identified phyllosilicates was derived mainly from the position of (06,33) diffraction bands despite significant overlap with phases such as quartz. XRD analyses were guided by the chemical analyses performed with SEM/EDX, and vice versa. The quantity of amorphous material was determined by adding corundum as an internal standard. The difference between the amount of corundum added and refined was recalculated into the amorphous content.

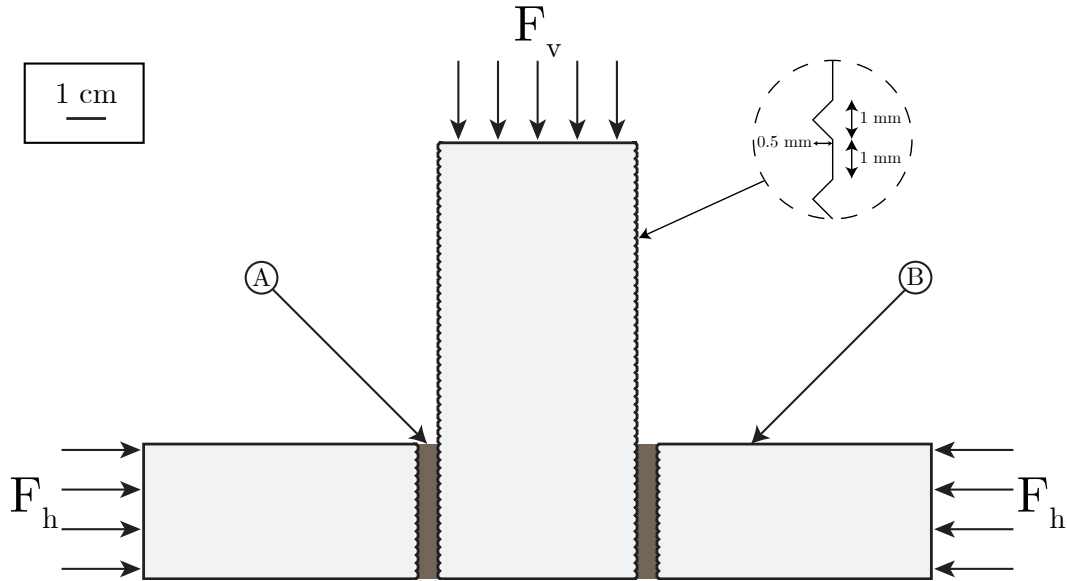


**Figure 3.** Side-on view of double-direct shear arrangement used during the investigation. (A) gouge sample; (B) stainless steel block. A horizontal piston on the right-hand-side of this image applies the horizontal (normal) force. The left-hand-side is supported by the HighSTEPS apparatus' internal wall. The vertical piston applies the vertical (shear) force through the central sample holder.

284

### 3.3 Apparatus

285

286

287

288

289

290

291

292

293

Double-direct shear experiments (Dieterich, 1972) were performed in the HighSTEPS apparatus (Violay et al., 2021), Figure 3, a biaxial apparatus located at the the Ecole Polytechnique Fédérale de Lausanne. The prepared gouge is placed in between one vertical and two horizontal sample holders, with 4.86 mm of gouge on either side, and is then compacted by hand with a steel block and a levelling jig. The surface of the horizontal sample holders on which the gouge is placed and compacted measures 34 mm by 34 mm. Both the horizontal and vertical sample holders are grooved to a depth of 0.5 mm, with the grooves repeating every 2 mm. The grooves ensure shearing occurs inside the gouge layer (Marone et al., 1990).

294

### 3.4 Experimental procedure

295

296

297

298

299

300

301

302

303

304

305

306

307

308

In order to test the frictional behaviour of the gouge samples, the sample holders are placed inside the apparatus and the horizontal piston is moved into contact with the sample holder. After contact is established, the normal load is increased to 1 MPa. At this stage, if the experiment is to be performed under nominally-wet conditions, the impermeable membrane (a plastic bag) containing the sample holders and sample is filled with deionized water, and the normal load of 1 MPa is held for 40 minutes. This corresponds to the time required for the horizontal piston to reach an approximately constant position. If the experiment is to be performed under nominally-dry conditions (room temperature and humidity), this holding period is skipped. Note that while deionized water can take a significant amount of time to reach equilibrium with gouge samples (up to two days with calcite gouge (Carpenter, Colletini, et al., 2016)), here additional XRD analyses were performed on a calcite-rich gouge (N3583) after an experiment to verify that there was no significant loss of calcite or alteration of clay minerals during the experiment, Supplementary Material, Figure S24 and Table S7. Next, the normal load is

309 increased to either 10, 30, or 50 MPa, depending on the experiment. These values cor-  
 310 respond to effective stresses typical of lithostatic burdens at approximately 650, 2000,  
 311 and 3300 m depth, respectively; depths relevant for shallow faults. This normal load is  
 312 then held for 20 minutes to allow for sample compaction, Supplementary Material, Fig-  
 313 ure S8. At this point nominally-wet samples have been equilibrating with the added wa-  
 314 ter for approximately 1.5-2.5 hours, depending on the normal stress of the experiment.  
 315 Then, the vertical piston, which is brought into contact with the vertical sample holder  
 316 at the beginning of the experiment, is lowered at  $10 \frac{\mu\text{m}}{\text{sec}}$  for 11 mm, Figure 4. This con-  
 317 stitutes the run-in phase of the experiment which allows for the development of the shear  
 318 fabric and steady-state friction (e.g., Pozzi et al. (2022); Noël et al. (2023); Noël, Gior-  
 319 getti, et al. (2024)). After the run-in, the velocity-step sequence is begun. Each veloc-  
 320 ity step is 500  $\mu\text{m}$  long, with 3, 10, 30, 100, and 300  $\frac{\mu\text{m}}{\text{sec}}$  being the up-step velocities. Next,  
 321 the slide-hold-slide sequence is begun, where during each slide-hold-slide the sample is  
 322 sheared for 500  $\mu\text{m}$  at  $10 \frac{\mu\text{m}}{\text{sec}}$  before the vertical piston holds a constant position for ei-  
 323 ther 1, 3, 10, 30, 100, 300, 1000, or 3000 seconds, after which the sample is again sheared  
 324 at  $10 \frac{\mu\text{m}}{\text{sec}}$  for 500  $\mu\text{m}$  as the next sliding phase is carried out. Finally, the vertical and  
 325 then horizontal forces are removed by first raising the vertical piston and then retract-  
 326 ing the horizontal piston. At this stage the sheared sample is stored, dried, and then placed  
 327 in epoxy resin to enable later thin section preparation for micro-structural analysis. All  
 328 18 samples were tested at 10, 30, and 50 MPa under both nominally-wet and nominally-  
 329 dry conditions resulting in 108 total experiments. Note that all references to wet and dry  
 330 conditions from this point on refer to nominally-wet (immersed but not necessarily sat-  
 331 urated) and nominally-dry (room humidity, approximately 40%) conditions, respectively.  
 332 All experiments are performed at room temperature, but it should be noted that, at low  
 333 temperatures ( $< 300$  °C), first-order friction characteristics are considered to be rela-  
 334 tively independent of temperature (e.g., Scholz (2019), ch. 2). That said, second-order  
 335 friction characteristics do often show temperature dependence (e.g., Blanpied et al. (1991);  
 336 Kolawole et al. (2019); Jeppson et al. (2023)).

## 337 4 Data Treatment

338 Considering that the gouges present a constant surface area of 34 mm by 34 mm,  
 339 the applied normal stress,  $\sigma$ , and shear stress,  $\tau$ , are calculated based on the applied ver-  
 340 tical and horizontal forces,  $F_v$  and  $F_h$ , respectively. Note that the shear stress is applied  
 341 across an area twice as large as that for the normal stress as the experiments were per-  
 342 formed in double-direct shear. Error in the force measurements was taken as 0.3 kN, based  
 343 on standard levels of noise. The slip,  $\delta$ , is calculated as the difference in vertical posi-  
 344 tion based on the values recorded by the optical encoder attached to the vertical piston  
 345 just above the sample. The layer thickness is calculated based on the values recorded by  
 346 the optical encoder fixed to the horizontal piston. Error in the displacement measure-  
 347 ments was taken as 250 nm, based on standard levels of noise (e.g., Figure 5c). The ef-  
 348 fective error on all single measurements propagates for other derived quantities, see Sup-  
 349plementary Material. Displacement data are corrected based on machine stiffnesses (Violay  
 350 et al., 2021). The data are not filtered and were collected at 10 Hz except during the ve-  
 351locity steps where the recording frequency was 2 kHz.

### 352 4.1 Friction Coefficients

353 Apparent friction,  $\mu^*$ , is defined based on the ratio between  $\tau$  and  $\sigma$ . Apparent fric-  
 354 tion coefficients calculated this way neglect cohesion, layer thinning, and densification  
 355 (Scott et al., 1994).

356

#### 4.1.1 Coefficient of frictional yield, $\mu_y$

357

358

359

360

361

362

363

364

365

366

367

368

369

370

371

372

373

374

375

During the elastic loading of the sample, a stiffness,  $k$ , is defined based on the linear portion of the loading curve, after anelastic deformation, and fit using a least-squares regression. An apparent frictional yield coefficient,  $\mu_y^*$ , is defined for each experiment based on the last moment that the loading curve intersects the line defined by  $k$ , breaking from linearity, Figure 4. This point is also known as the proportional limit. The criterion used for defining the accepted deviation is somewhat arbitrary, meaning application of this parameter to real conditions should be done with care (e.g., Kutz (2009), pg. 445). Instead, this parameter should be treated as a simple proxy for the yield point of the material. Note, however, the yield point is likely dependent on temperature, such that it is difficult to apply these values, found at room temperature, to reservoir conditions. Using the values of  $\mu_y^*$ , a coefficient of frictional yield,  $\mu_y$ , is defined for each rock sample using a least-squares estimate, based on the values of  $\mu_y^*$  from experiments at 10 MPa, 30 MPa, and 50 MPa normal stress, weighted based on the uncertainty of each data point, with cohesion forced to be zero, Figure 4(b,c). Note that this parameter is not necessarily a coefficient, but is presented as such to capture the dependence on normal stress. Details on the fitting and confidence interval are provided in Supplementary Material and Montgomery and Runger (2011). This process is performed for both the wet and dry suites of experiments, yielding a wet,  $\mu_y^w$ , and dry,  $\mu_y^d$ , coefficient of frictional yield for each sample.

376

#### 4.1.2 Dynamic coefficient of friction, $\mu_d$

377

378

379

380

381

382

383

384

385

An apparent dynamic coefficient of friction,  $\mu_d^*$ , is defined for each experiment as the average value of  $\mu^*$  during the last 1.5 mm of the run-in, Figure 4. Then, for each sample, a dynamic coefficient of friction,  $\mu_d$ , is defined using a least-squares estimate, based on the values of  $\mu_d^*$  from experiments at 10 MPa, 30 MPa, and 50 MPa normal stress, weighted based on the uncertainty of each data point, with cohesion forced to be zero, Figure 4(b,c). Details on the fitting and confidence interval are provided in Supplementary Material and Montgomery and Runger (2011). This process is performed for both the wet and dry suites of experiments, yielding a wet,  $\mu_d^w$ , and dry,  $\mu_d^d$ , dynamic coefficient of friction.

386

## 4.2 Velocity Steps

387

388

389

The velocity dependence of friction, a key component of one of the two principal criteria for the nucleation of a dynamic earthquake (Rice & Ruina, 1983; Ruina, 1983), is modelled using the rate-and-state friction constitutive law (Dieterich, 1979),

$$\mu^* = \mu_0^* + a \ln \left( \frac{v}{v_0} \right) + b \ln \left( \frac{v_0 \theta}{D_c} \right), \quad (1)$$

390

391

392

where  $\mu_0^*$  is an initial value of apparent friction prior to a change in velocity from  $v_0$  to  $v$ ,  $a$  is the direct effect,  $b$  is the evolution effect,  $D_c$  is the critical slip distance, and  $\theta$  is a state variable which is given by,

$$\frac{d\theta}{dt} = -\frac{v\theta}{D_c} \ln \left( \frac{v\theta}{D_c} \right), \quad (2)$$

393

394

395

396

397

398

when described by the slip law (Ruina, 1983). Velocity steps are detrended and then fit with RSFit3000 (Skarbek & Savage, 2019), Figure 5. Insight into frictional stability can then be provided by evaluating  $a-b$ , where  $a-b > 0$  represents velocity-strengthening behaviour and  $a-b < 0$  velocity-weakening behaviour. Velocity-weakening behaviour is one of the necessary conditions for unstable fault slip under the assumption of small perturbations (Rice & Ruina, 1983; Ruina, 1983).

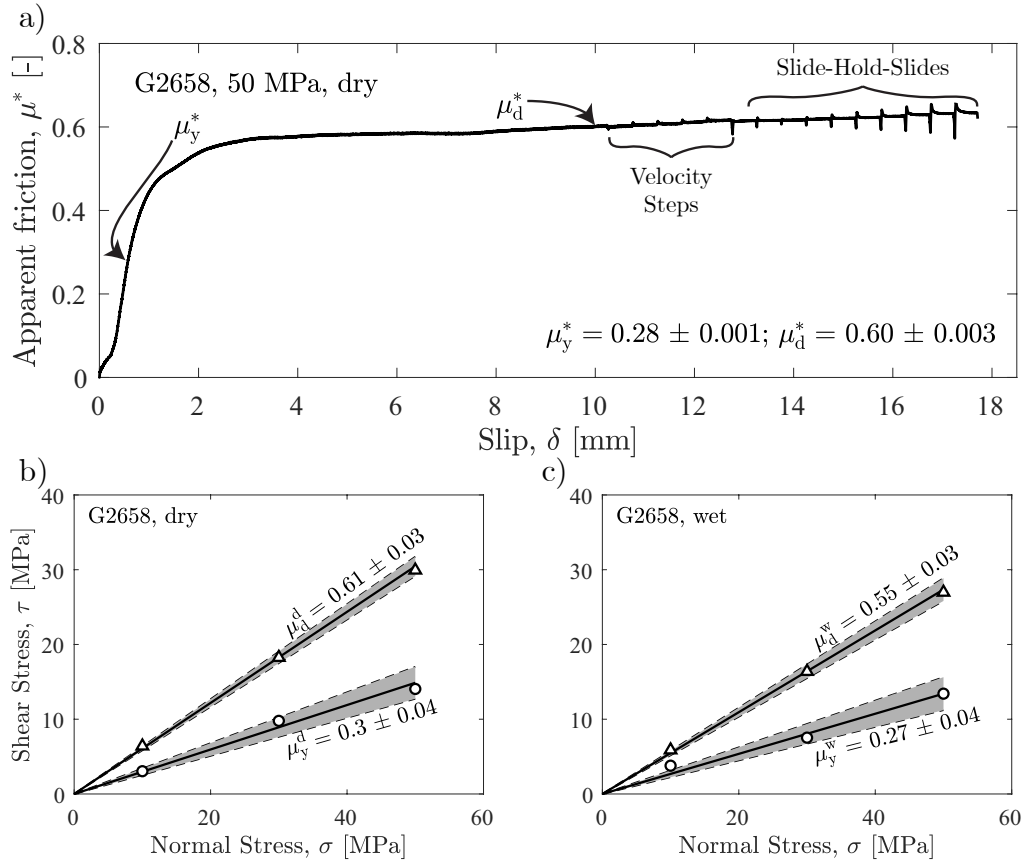


**Figure 4.** a) An example experiment, G2658 at 50 MPa normal stress under dry conditions. (b,c) A demonstration of how the picked values of the apparent frictional yield and dynamic friction coefficients are used to calculate the actual coefficients of frictional yield and dynamic friction coefficients of the samples. The sample G2658 is used as an example.

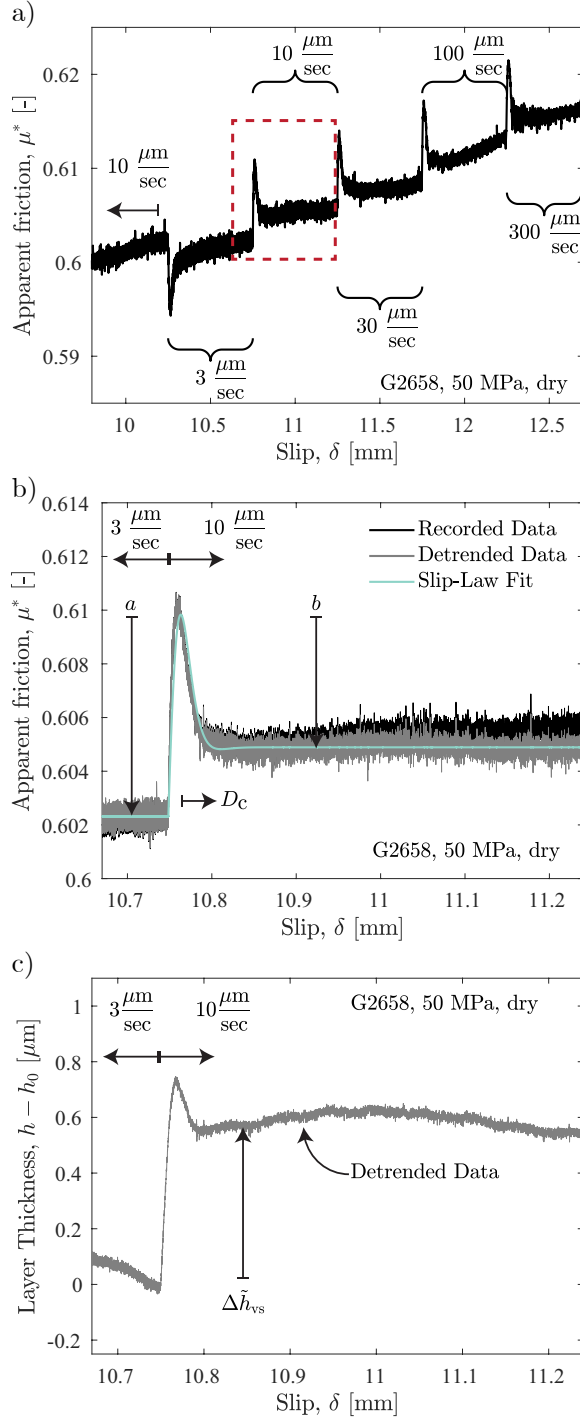


**Figure 5.** A series of velocity steps from an example experiment, G2658 at 50 MPa under dry conditions. a) The full series of velocity steps. After a run-in performed at 10  $\frac{\mu\text{m}}{\text{sec}}$ , velocity steps of 3, 10, 30, 100, and 300  $\frac{\mu\text{m}}{\text{sec}}$  are performed, each for 500  $\mu\text{m}$ . b) A zoom on the region outlined by a dotted red line in (a). The velocity step is fit with both the slip and aging laws, with the slip-law fit shown here. The parameters  $a$ ,  $b$ , and  $D_c$  are illustrated. c) The change in layer thickness based on detrended data. This image illustrates how  $\Delta \tilde{h}_{vs}$  is found.

399

### 4.3 Slide-Hold-Slides

400

401

402

403

404

405

406

407

Inter-seismic healing can be assessed through the use of slide-hold-slides (Dieterich, 1972), providing insight into potential earthquake recurrence time and strength recovery along faults. The healing that occurs during a given slide hold slide,  $\Delta\mu_h^*$ , is found as the difference between the peak in apparent friction achieved upon reshearing and the steady-state value of apparent friction prior to the hold, Figure 6(a, b). Generally, the healing increases with the logarithm of time (Dieterich, 1972). This allows for the definition of a healing rate,  $\beta$ , which is defined based on (Paterson and Wong (2005), pg. 174),

$$\Delta\mu_h^* = \beta \log_{10} \left( 1 + \frac{t_h}{t_c} \right), \quad (3)$$

408

409

410

where  $t_h$  is the hold time and  $t_c$  is the hold time for which the healing can be considered to be zero, taken here as one divided by the recording frequency of 10 Hz. This is then solved for  $\beta$  with a weighted-least-squares estimate using all eight holds, Figure 6d.

411

### 4.4 Dilatancy Measurements

412

#### 4.4.1 Velocity Steps

413

414

415

Based on Marone and Kilgore (1993); Ikari et al. (2009); Giacomel et al. (2021), and analogous to the parameter  $\epsilon$  from Segall and Rice (1995), a parameter  $\alpha$  representing the normalized dilation is defined for each velocity step,

$$\frac{\Delta h_{vs}}{h_0} = \alpha \ln \left( \frac{v}{v_0} \right), \quad (4)$$

416

417

418

419

420

which acts as a measure of the dilatancy response of the gouge to a change in velocity. Then,  $\Delta h_{vs}$  is the near-instantaneous dilatancy that occurs when the velocity changes from  $v_0$  to  $v$  during a velocity step and  $h_0$  the layer thickness just prior to the step. Note that the layer thickness is de-trended prior to this calculation based on the approximately linear steady-state change in layer thickness occurring after the velocity step, Figure 5c.

421

#### 4.4.2 Slide-Hold-Slides

422

423

The change in layer thickness that occurs during a given slide hold slide,  $\Delta h_{shs}$ , is calculated as (e.g., Giacomel et al. (2021)),

$$\Delta h_{shs} = \partial \tilde{h}_h + \partial \tilde{h}_s, \quad (5)$$

424

425

426

427

428

429

where  $\partial \tilde{h}_h$  is the dilation that occurs during the hold phase, based on the average thickness of the gouge (i.e., considering the experiments are performed in double-direct shear), and  $\partial \tilde{h}_s$  is the dilation that occurs upon re-shearing, again based on the average thickness of the gouge. Note that  $\partial \tilde{h}_h$  is a negative value as the gouge compacts during a hold. This allows for the definition of three dilation rates:  $B_h$ ,  $B_s$ ,  $B_{shs}$ , for the hold periods, re-shearing events, and overall slide-hold-slide sequence which are the best-fit slopes of

$$\frac{\partial \tilde{h}_h}{h_0} = B_h \log_{10} \left( 1 + \frac{t_h}{t_c} \right), \quad \frac{\partial \tilde{h}_s}{h_0} = B_s \log_{10} \left( 1 + \frac{t_h}{t_c} \right), \quad \frac{\Delta h_{shs}}{h_0} = B_{shs} \log_{10} \left( 1 + \frac{t_h}{t_c} \right). \quad (6)$$

430

431

432

433

434

435

436

437

An illustration of these calculations can be seen in Figure 6(c, e). Note that, as  $\Delta h_{shs}$  is a linear combination of  $\partial \tilde{h}_h$  and  $\partial \tilde{h}_s$ ,  $B_{shs}$  is also a linear combination of  $B_h$  and  $B_s$ . Therefore,  $B_h$  and  $B_s$ , two different measurements of dilatancy at different parts of the slide-hold-slides, will be presented here to highlight the rate of change in layer thickness during the slide-hold-slides. Other authors have first de-trended the layer thickness to account for monotonic long-term trends in dilation (Giacomel et al., 2021). This was not done here due to the use of load point displacement measurements (as opposed to measurements directly on the fault). Correcting for layer thickness as a function of vertical



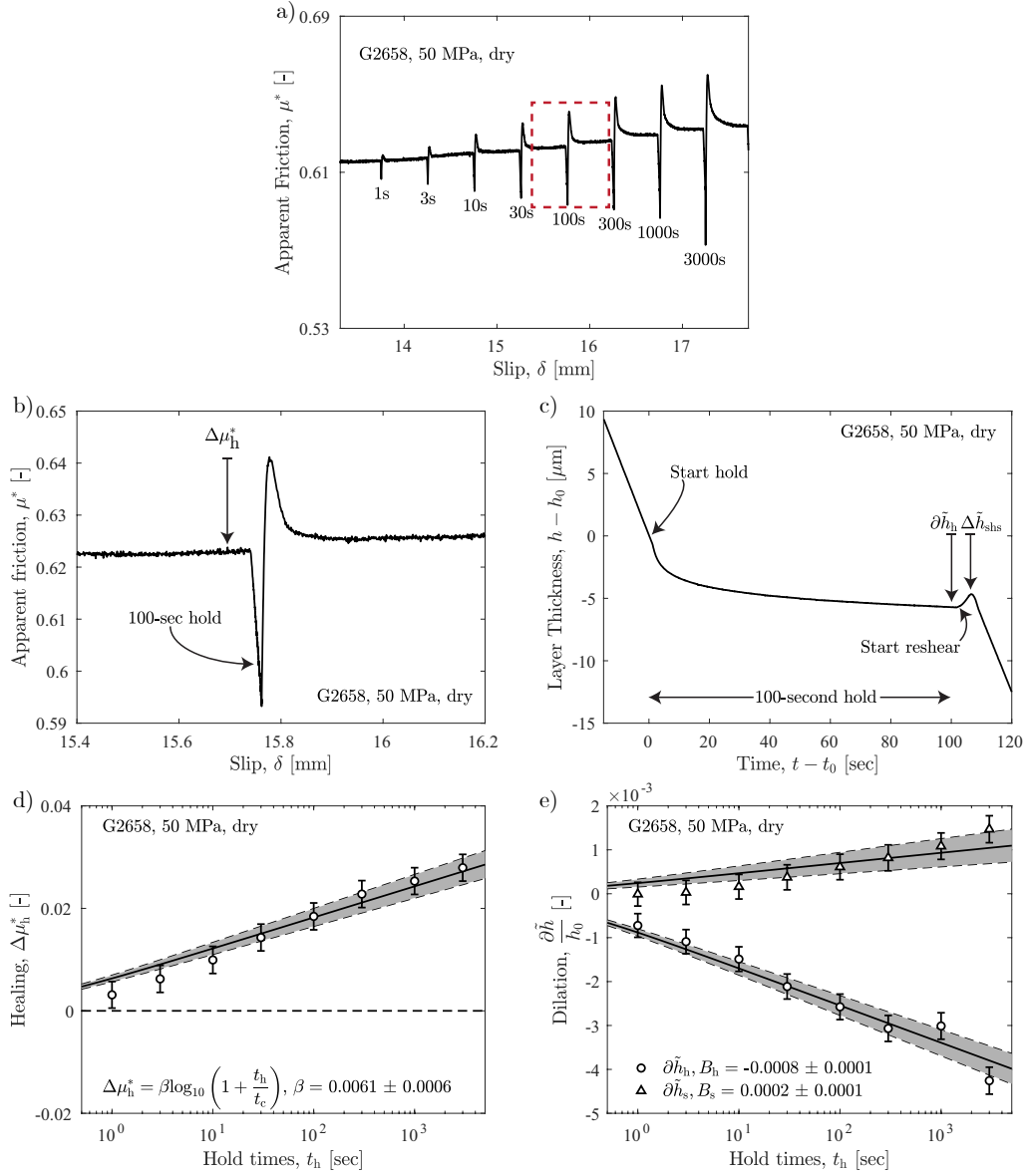


**Figure 6.** a) An example of a sequence of slide-hold-slides for sample G2658 at 50 MPa under dry conditions. The hold periods are written under the minimum value of apparent friction reached during each hold. b) A zoom on the area in (a) delineated by a dotted red box. c) The change in layer thickness occurring during the 100-second hold, corresponding to the dotted red box in (a). Note that, from Equation 5,  $\Delta h_{shs} = \partial\tilde{h}_h + \partial\tilde{h}_s$ . d) The healing incurred after each hold is plotted as points. These points are then fit to find a value for the healing rate,  $\beta$ . The error for the linear fit is weighted based on the error of each value of  $\Delta\mu_h^*$  and fit with a 95 percent confidence interval. e) The normalized dilation incurred during the hold,  $\partial\tilde{h}_h$ , and upon reshear,  $\partial\tilde{h}_s$ . These data are then fit with Equation 6 to find the dilation rates,  $B_h$ ,  $B_s$ , and  $B_{shs}$  (not shown).

438 slip while using load point displacement measurements would incorrectly adjust layer thick-  
 439 ness during the re-shear period prior to the re-initiation of slip. Finally, while the data  
 440 fit to all three measured dilations in Equation 6 are not truly linear, their fitted slopes  
 441 still serve as a useful tool to compare the relative tendencies for dilation in the differ-  
 442 ent experiments.

## 443 5 Results

### 444 5.1 Sample Characteristics

#### 445 5.1.1 Alteration Features

446 SEM analyses showed clear differences in sample mineralogy. In particular, certain  
 447 samples were clearly highly altered presenting many secondary minerals, while others  
 448 were composed almost exclusively of primary minerals. As an example, Figure 7 shows  
 449 four samples: LA02767 (a), LA03749 (b), LA02422 (c), and N4343 (d). While LA02767  
 450 has experienced alteration, in particular with the presence of chlorite and quartz, it is  
 451 one of the least-altered samples in this study, and may therefore be representative of a  
 452 zone which has undergone only limited rock-fluid interaction. LA03749 is an altered sam-  
 453 ple principally composed of phyllosilicates (kaolinite and smectite), with some carbon-  
 454 ate minerals (ankerite). It is likely that the rod-like shapes were originally plagioclase.  
 455 In LA02422, likely coming from an illite-rich or Al-smectite/kaolinite-rich zone, phyllosil-  
 456 icates (kaolinite and illite) and carbonates (siderite) are common. N4343 contains a sig-  
 457 nificant amount of chlorite and is thus likely coming from a chlorite-rich zone. However,  
 458 the presence of other phyllosilicates suggests this sample might represent an intermedi-  
 459 ate state, with multiple alteration phases.

#### 460 5.1.2 XRD

461 The detailed XRD results are presented in Supplementary Material, Tables S1-S5,  
 462 but a simplified version is given here in Table 2. Note that the expandable clays and kaoli-  
 463 nite are typical of the Al-smectite/kaolinite- or Mg-smectite-rich zones (kaolinite is never  
 464 associated to Mg-smectite), the micas are typical of the illite-rich zone (illite is a dioc-  
 465 tahedral mica), and chlorite is typical of the chlorite-rich zone. The samples are classi-  
 466 fied based on both their absolute weight percentage of phyllosilicate content and the rel-  
 467 ative amounts of each phyllosilicate, Table 2. Samples more than 40% by weight phyl-  
 468 losilicate are considered highly altered, between 20% and 40% by weight are moderately  
 469 altered, and below 20% are slightly altered. In this sense, phyllosilicate content is used  
 470 a proxy for the level of alteration as phyllosilicates are secondary minerals in these sam-  
 471 ples. If a sample's phyllosilicate content is made up of more than 67% of a given phyl-  
 472 losilicate type then that sample is considered to be representative of the zone correspond-  
 473 ing to that phyllosilicate. Based on this classification, LA03749 has a mineralogy rep-  
 474 resentative of a highly-altered Al-smectite/kaolinite-rich zone. B494D, S491I, N3583, and  
 475 N3808 have mineralogies which might be representative of Al-smectite/kaolinite- or Mg-  
 476 smectite-rich zones which are moderately altered. G2658, N4330, and N4422 could be  
 477 representative of Mg-smectite zones that are only slightly altered. S491B can be consid-  
 478 ered representative of a highly-altered illite-rich zone. LA02422 and LA02451 can be con-  
 479 sidered highly-altered samples, intermediate between all three zones. M1430 and N4343  
 480 are intermediate between zones but only moderately altered. LA03758 is also interme-  
 481 diate but only lightly altered. LA02767, G2690, G3005, and G3130 can be considered  
 482 to represent the chlorite-rich zone with a low level of alteration.

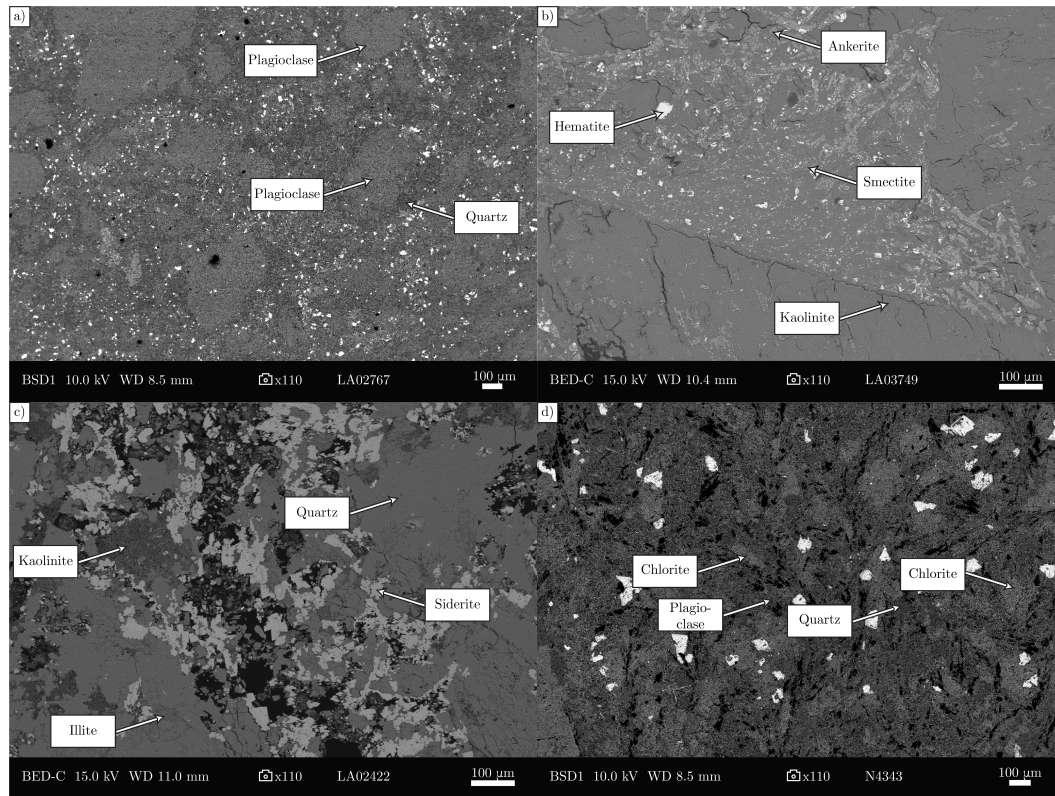


**Figure 7.** Images of polished thin sections made from intact samples taken during SEM analysis with backscattered electrons, illustrating density contrast. a) LA02767 is only lightly altered, with the presence of a small amount of chlorite. b) LA03749 is highly altered, exhibiting secondary minerals almost exclusively. In particular, this sample is marked by the significant presence of smectite and kaolinite, making it representative of the clay cap of a geothermal reservoir in a volcanic arc setting. c) LA02422 is also highly altered, with the most abundant phyllosilicates being dioctahedral micas, as can be seen by the illite present on the SEM image. However, this sample is classified as intermediate due to the presence of kaolinite and 2:1 expandable dioctahedral clays. d) N4343 is only moderately altered, but contains a significant amount of chlorite and is classified as intermediate between alteration zones. In (b) the shapes of replaced primary minerals (in many instances likely plagioclase) can be clearly seen.

**Table 2.** The results of the XRD analysis for all samples. The results here are simplified through the use of an "Other" category. Detailed XRD results can be found in Supplementary Material, Tables S1-S5. Values are given in weight percentage. Uncertainties expressed as standard deviation of the Rietveld refinement only. K-spar - potassium feldspars, Clino-Px - clinopyroxenes, dioc. - dioctahedral (Al - rich for expandables), trioc. - trioctahedral (Mg - rich for expandables), exp. - expandable, i.e., either pure smectite or smectite-containing mixed layer. Samples used for XRD underwent a different grinding procedure than those used for friction tests.

Sample	Location	Pred. Alt. Type	Plagioclase	Clino-Px	K-spar	Quartz	2:1 Exp. dioc.	2:1 Exp. trioct	Kaolinite	Mica dioc.	Mica trioct.	Chlorite	Vermiculite	Other	Amorphous
B494D	Les Saintes	Smectite	33.7 ± 0.5	-	5.9 ± 0.3	28.2 ± 0.4	12.7 ± 0.8	5.4 ± 0.4	-	-	-	4.4 ± 0.5	-	9.9 ± 0.3	5 ± 0
S491I	Les Saintes	Smectite	25.9 ± 0.4	-	5.3 ± 0.2	27.4 ± 0.3	24.8 ± 0.7	3.8 ± 0.4	-	-	-	-	-	13.1 ± 0.5	5 ± 0
S491B	Les Saintes	Illite	-	-	1.7 ± 0.2	43.2 ± 0.4	-	-	-	46.2 ± 0.5	3.2 ± 0.3	-	-	4.7 ± 0.2	-
LA02422	Lamenin	Intermediate	-	-	-	34 ± 0.2	7.4 ± 0.5	-	15.6 ± 0.3	27.9 ± 1.2	-	-	-	15.2 ± 1.3	-
LA02541	Lamenin	Intermediate	13.8 ± 0.2	2.8 ± 0.2	-	19.5 ± 0.2	14.3 ± 0.7	-	-	17.7 ± 0.8	-	11.6 ± 0.4	-	20.3 ± 0.7	-
LA02767	Lamenin	Chlorite	50.7 ± 1.7	-	2.8 ± 0.2	17.3 ± 0.2	-	-	-	0.6 ± 0.2	-	9.5 ± 0.3	-	11.2 ± 0.7	8 ± 0
LA03749	Lamenin	Al-smectite/Kaolinite	11.8 ± 0.2	-	-	0.6 ± 0.1	41.4 ± 0.7	-	19 ± 0.9	-	-	-	1.2 ± 0.2	26.1 ± 1.2	-
LA03758	Lamenin	Intermediate	51.7 ± 0.8	6.9 ± 0.2	3.1 ± 0.2	0.4 ± 0	8.7 ± 0.2	-	1.9 ± 0.2	-	-	8.4 ± 0.5	-	10.5 ± 0.8	8.4 ± 0
M1430	Mount Meager	Intermediate	40.6 ± 0.4	-	10.4 ± 0.3	20.5 ± 0.2	9.2 ± 0.2	-	-	2 ± 0.2	-	9.9 ± 0.6	-	7.3 ± 0.2	-
G2658	Summerland Basin	Mg-smectite	28.3 ± 0.5	15.2 ± 0.5	29 ± 1.15	5.6 ± 0.3	-	13.2 ± 0.5	-	-	1 ± 0.1	1.2 ± 0.3	-	6.5 ± 0.8	-
G2690	Summerland Basin	Chlorite	25.9 ± 0.6	-	30.3 ± 1.5	5.4 ± 0.1	-	3.7 ± 0.6	-	-	-	13.2 ± 0.6	-	20.6 ± 1.2	5 ± 0
G3005	Summerland Basin	Chlorite	21.3 ± 0.3	11.1 ± 0.2	15.9 ± 0.3	-	-	3.4 ± 0.3	-	-	-	11.3 ± 0.8	0.5 ± 0.2	36.5 ± 1.6	-
G3130	Summerland Basin	Chlorite	33.3 ± 2.3	3.5 ± 0.3	20.6 ± 1.4	7.3 ± 0.5	-	1 ± 0.1	-	-	-	18.9 ± 2	-	15.5 ± 1.5	5 ± 0
N3583	Newberry	Mg-smectite	39.8 ± 0.8	-	2.7 ± 0.3	10.2 ± 0.1	-	23.5 ± 0.6	-	-	-	-	-	23.9 ± 0.7	-
N3808	Newberry	Mg-smectite	49.3 ± 0.8	-	2.5 ± 0.2	15.6 ± 0.2	-	21.5 ± 2.3	-	-	-	-	-	11 ± 0.5	-
N4330	Newberry	Mg-smectite	62.4 ± 2.1	10.1 ± 0.4	0.6 ± 0.2	4.4 ± 0.1	-	15.4 ± 0.4	-	-	-	-	-	7.3 ± 0.7	5 ± 0
N4343	Newberry	Intermediate	39.5 ± 1.5	-	4.9 ± 0.2	17.7 ± 0.4	-	9.2 ± 0.9	-	-	-	11.1 ± 2.7	-	17.7 ± 0.9	-
N4422	Newberry	Mg-smectite	55.7 ± 1.4	1.1 ± 1.2	4 ± 0.2	11.2 ± 0.2	-	18.3 ± 1.1	-	-	-	-	-	9.7 ± 0.8	-

**Table 3.** A summary of the friction coefficients. The coefficients of frictional yield for dry and wet conditions are given by  $\mu_y^d$  and  $\mu_y^w$ , respectively. The dynamic coefficients of friction for dry and wet conditions are given by  $\mu_d^d$  and  $\mu_d^w$ , respectively. Each friction coefficient is based on three separate experiments, each at a given normal stress of either 10, 30, or 50 MPa. See Figure 4 for an illustration of this procedure. The error refers to the 90% confidence interval fit, see Supplementary Material. Predominant alteration type is based on Table 2.

Sample	Location	Pred. Alt. Type	$\mu_y^d$ [-]	$\mu_y^w$ [-]	$\mu_d^d$ [-]	$\mu_d^w$ [-]
B494D	Les Saintes	Smectite	0.26 ± 0.02	0.23 ± 0.01	0.57 ± 0.01	0.48 ± 0.01
S491I	Les Saintes	Smectite	0.18 ± 0.04	0.19 ± 0.04	0.56 ± 0.03	0.40 ± 0.01
S491B	Les Saintes	Illite	0.16 ± 0.05	0.18 ± 0.04	0.46 ± 0.01	0.33 ± 0.02
LA02422	Lamentin	Intermediate	0.26 ± 0.02	0.17 ± 0.03	0.48 ± 0.02	0.35 ± 0.01
LA02541	Lamentin	Intermediate	0.21 ± 0.04	0.21 ± 0.07	0.51 ± 0.02	0.37 ± 0.02
LA02767	Lamentin	Chlorite	0.29 ± 0.02	0.23 ± 0.06	0.59 ± 0.03	0.59 ± 0.03
LA03749	Lamentin	Al-smectite/Kaolinite	0.19 ± 0.03	0.15 ± 0.02	0.25 ± 0.05	0.24 ± 0.02
LA03758	Lamentin	Intermediate	0.25 ± 0.04	0.23 ± 0.03	0.59 ± 0.02	0.53 ± 0.03
M1430	Mount Meager	Intermediate	0.22 ± 0.06	0.24 ± 0.05	0.58 ± 0.02	0.50 ± 0.02
G2658	Summerland Basin	Mg-smectite	0.30 ± 0.04	0.27 ± 0.04	0.61 ± 0.03	0.55 ± 0.03
G2690	Summerland Basin	Chlorite	0.28 ± 0.05	0.32 ± 0.07	0.58 ± 0.02	0.51 ± 0.01
G3005	Summerland Basin	Chlorite	0.27 ± 0.05	0.30 ± 0.01	0.60 ± 0.03	0.54 ± 0.02
G3130	Summerland Basin	Chlorite	0.30 ± 0.02	0.28 ± 0.02	0.60 ± 0.02	0.53 ± 0.01
N3583	Newberry	Mg-smectite	0.24 ± 0.05	0.22 ± 0.03	0.55 ± 0.07	0.48 ± 0.09
N3808	Newberry	Mg-smectite	0.22 ± 0.02	0.24 ± 0.06	0.58 ± 0.04	0.48 ± 0.03
N4330	Newberry	Mg-smectite	0.24 ± 0.05	0.28 ± 0.04	0.59 ± 0.04	0.49 ± 0.06
N4343	Newberry	Intermediate	0.27 ± 0.04	0.30 ± 0.11	0.59 ± 0.02	0.49 ± 0.02
N4422	Newberry	Mg-smectite	0.28 ± 0.14	0.25 ± 0.04	0.59 ± 0.03	0.50 ± 0.03

483

## 5.2 Overall summary of friction coefficients

484

485

486

487

488

489

490

491

492

493

494

495

496

497

498

499

Coefficients of frictional yield have a median value of approximately 0.26 in dry conditions and 0.24 in wet conditions, meaning any water weakening that is present is generally within the errors of the calculations of the friction coefficients. Dry dynamic friction coefficients have values which are typically between 0.55 and 0.60, with the lowest value being 0.25, the highest 0.61, and the median 0.58. Sample with more phyllosilicate content generally have low dynamic friction coefficients. Note that these friction coefficients, in particular the dynamic friction coefficients, are generally associated with narrow 90% confidence windows, despite all possible sources of experimental error, Table 3. This acts as justification for cohesion being neglected. Water-induced frictional-strength reduction for the dynamic coefficient of friction is present in all but one sample (LA02767). The median value of water-induced frictional-strength reduction is 0.09, with the most extreme water-induced frictional-strength reduction seen in S491I, a difference of 0.16 or 29%. Water-induced frictional-strength reduction is more common in samples rich in phyllosilicate content. The friction coefficients are summarized in Table 3, with a more detailed look at site-specific results in the Supplementary Material, Section 4 and Figures S9 and S10.

500

## 5.3 Overall summary of velocity steps

501

502

503

504

Of the 18 samples tested, in 14 cases  $a$  is larger in wet conditions than in dry conditions. Similarly, in 11 instances  $b$  is larger in dry conditions than in wet conditions. Ultimately, however,  $a - b$  is larger (more positive) in wet conditions than in dry conditions for 17 of the samples. Regarding the critical slip distance,  $D_c$  is often larger (for

505 15 out of 18 samples) in wet conditions than in dry conditions. Finally,  $\alpha$  is larger in wet  
 506 conditions than in dry conditions for 15 of the samples.

507 As normal stress increases,  $a$  decreases for 14 of the samples. Similarly,  $b$  decreases  
 508 with increasing normal stress for 12 of the samples. Finally, however,  $a-b$  increases with  
 509 increasing normal stress for 4 of the samples, decreases for 3 samples, and displays no  
 510 clear trend with normal stress for 11 samples. The critical slip distance increases with  
 511 increasing normal stress for 6 samples, decreases with increasing normal stress for 1 sam-  
 512 ple, and displays no clear trend with normal stress for 11 samples.  $\alpha$  increases with in-  
 513 creasing normal stress for 1 samples, decreases for 2 samples, but displays no clear trend  
 514 for the other 15 samples. These data can be found in the Supplementary Material, Ta-  
 515 bles S8 to S25, with a description of site-specific results in the Supplementary Material,  
 516 Section 4 and Figures S11-S15.

#### 517 **5.4 Overall summary of frictional healing**

518 The healing rate does not consistently vary with water presence when all of the sam-  
 519 ples are taken together, in some instances it decreases when the experiment was performed  
 520 in wet conditions in others it increases. This effect is clearly composition dependent. When  
 521 the healing rate varies with normal stress, most often it decreases as normal stress in-  
 522 creases, otherwise it remains approximately constant. An increasing healing rate with  
 523 increasing normal stress is rare in these samples. Phyllosilicate-poor (<25%) samples (B494D,  
 524 LA02767, LA03758, M1430, G2658, G2690, G3005, G3130) have a decreasing healing rate  
 525 with increasing normal stress in dry conditions. These data can be found in the Supple-  
 526 mentary Material, Tables S26-S30. Site-specific descriptions of the results can be found  
 527 in the Supplementary Material, Section 4 and Figures S16 and S18.

528 Values for  $B_h$ , the dilation rate (often negative, implying compaction) during the  
 529 hold, are greater (more negative) in wet conditions than in dry conditions for almost all  
 530 of the experiments performed. The values for  $B_s$ , the dilation rate during the reshear,  
 531 are more mixed when compared between dry and wet conditions, and can be considered  
 532 generally similar. For higher normal stresses,  $B_h$  is often greater. A similar, but less con-  
 533 sistent, trend persists for  $B_s$ . These data can be found in the Supplementary Material,  
 534 Tables S26-S30. Site-specific descriptions of the results can be found in the Supplemen-  
 535 tary Material, Section 4 and Figures S17 and S19.

536 Finally, negative healing rates were consistently observed in N3583 in wet condi-  
 537 tions and LA03749 in wet conditions for large hold times. These negative healing rates  
 538 led to negative healing for large hold times, generally at either 1000 or 3000 seconds. Neg-  
 539 ative healing was not observed for these samples in dry conditions. Isolated instances  
 540 of negative healing rates were also observed in LA02422 and N3808. Negative healing  
 541 will be further discussed in Section 6.1.

#### 542 **5.5 Post-Mortem Microstructure**

543 An analysis of the post-mortem sample fabrics, Figure 8, reveals fabric elements  
 544 typical of deformation of brittle fault rocks, particularly when phyllosilicate content is  
 545 low. Phyllosilicate-rich rocks are more likely to develop the S-C-C' fabrics common in  
 546 this type of material and first described for ductilely-deformed mylonites (e.g., Berthé  
 547 et al. (1979); Volpe et al. (2022)), Figures 8(b, d). Conversely, samples with limited amounts  
 548 of phyllosilicates are more likely to develop Y-B-P-R fabrics typical of granular-rich faults  
 549 (e.g., Logan et al. (1992); Volpe et al. (2022)), Figures 8(a-c). In general, the lightly-altered  
 550 samples, limited in their phyllosilicate contents, exhibited the highest levels of localized  
 551 deformation. In samples richer in phyllosilicates, deformation was more distributed (duc-  
 552 tile). This is an indication of a change in mode of deformation, from localized to duc-  
 553 tile, as phyllosilicate content increases. Further, a change in mechanism is also likely, as

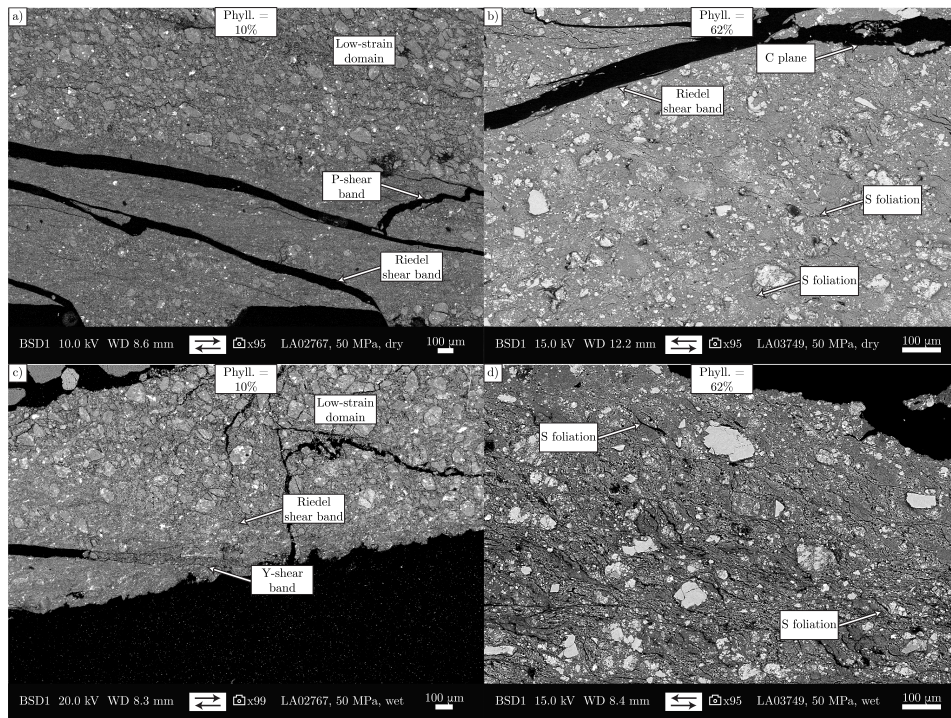


**Figure 8.** SEM images are of samples deformed at 50 MPa under (a, b) dry and (c, d) wet conditions. The samples shown are (a, c) LA02767 and (b, d) LA03749. LA02767 represents a sample exhibiting minimal alteration, with a low (10%) weight percentage of phyllosilicates. LA03749 is a highly-altered sample with significant amounts of kaolinite and smectite (62% by weight phyllosilicates). a) A low-strain domain as well as R- and P-shear bands can be seen. c) A low strain domain along with Y- and R-shear bands can be seen. b) C planes, R-shear bands, as well as S foliations can be seen. d) S foliations can be seen. Generally, while localization still occurs for the sample high in phyllosilicate content (LA03749 in b, d), deformation is more ductile (distributed) in this case compared to the sample low in phyllosilicate content (LA02767 in a, c). These images can be further compared with Figure 10(b-e), which also shows a sample deformed at 50 MPa containing 24% phyllosilicate content by weight. Arrows underneath the images show the far-field shear direction. It should be noted that the part of the thin section near the teeth (e.g., the bottom of (a)) was often not recovered. Additional localization often occurs in this part of the gouge. The pre-mortem images of these samples can be found in Figure 7(a, b).

554 rocks with principally Y-B-P-R fabrics (seen primarily in samples with low phyllosili-  
 555 cate contents) indicate cataclastic processes as the primary deformation mechanism. Con-  
 556 versely, rocks with principally S-C-C' (seen primarily in samples with high phyllosilicate  
 557 contents) fabrics indicate frictional sliding along foliations (Volpe et al., 2022). Note that  
 558 both of these mechanisms are brittle deformation mechanisms. This implies that alter-  
 559 ation, by producing phyllosilicate minerals in these settings, promotes both a change in  
 560 deformation mode and mechanism. Generally, dry experiments also produced increased  
 561 localized deformation compared to wet experiments, with wet experiments also gener-  
 562 ally yielding more widespread grain-size reduction.

## 6 Discussion

### 6.1 Negative frictional healing

Interestingly, while the frictional resistance upon reshear of all of the samples increases with the logarithm of hold time for small hold times (<1000 seconds), for a few samples (N3583, LA03749, LA02422, and N3808), large hold times (>1000 seconds) may result in negative healing rates and even negative healing. This phenomenon is most pronounced in N3583 in wet conditions at all tested normal stresses, Figure 9. This phenomenon is clearly dependent on water presence, as the same sample tested in dry conditions does not result in negative healing, Figure 9. Negative healing rates and negative healing have been previously observed (Boulton et al., 2012; Chen et al., 2015; Tesei et al., 2017; Orellana et al., 2018; Jeppson et al., 2023; Pozzi et al., 2023). Tesei et al. (2017) observed negative healing for bare-surface carbonate samples, relating it to fast-healing gouge patches that ultimately result in the fracturing of the intact rock, yet here experiments were performed on gouge. Orellana et al. (2018), who observed negative healing for small hold times in Opalinus Clay, suggested that their negative healing could be explained by a local overpressure at small hold times; this would result in transiently reduced effective normal stresses and therefore reduced strength. This mechanism is a possible explanation for the negative healing observed here, and was also suggested by Boulton et al. (2012), but is difficult to confirm without on-fault pore pressure measurements. Here, however, negative healing was only observed at large hold times. Jeppson et al. (2023) observed negative healing only at elevated temperatures (200°C) and suggested that the underlying mechanisms was thermally activated. Here, however, negative healing was observed at room temperature. The negative healing for N3583 in wet conditions is associated with an increased compaction during the hold (negative dilation) relative to dry experiments, Figure 9(d), but the dilation upon reshear is quite similar for both wet and dry cases, Supplementary Material, Figure S21. Reversing the hold times still resulted in only large hold times yielding negative healing, indicating a limited effect of strain, Supplementary Material, Figure S22.

The post-mortem microstructures of N3583 can be observed in Figure 10, with Figure 10(a) showing an undeformed sample. In Figure 10(b, d), the sample deformed in dry conditions and did not demonstrate negative healing. In Figure 10(c, e) the sample deformed in wet conditions and did exhibit negative healing. Clearly, a significant difference in grain size can be observed between the two cases. This suggests that the sample deformed in wet conditions experiences significantly more cataclasis than the sample deformed under dry conditions; however, this is a common effect observed in many samples. Further, the grains are more rounded and less angular when N3583 is deformed in wet conditions, which can be indicative of dissolution.

Indeed, Jeppson et al. (2023) speculated that the development of alteration products, such as phyllosilicates, and solution-transfer processes may have lowered the strength of the rock in their case; however, XRD analyses performed after the experiment reveal that the gouge composition did not change during the experiment, at least not on the scale of the bulk, Supplementary Material, Figure S24 and Table S7. It can be noted in Table 2 that N3583 has the most 2:1 expandable trioctahedral clays of all the samples. N3808, a sample which also showed limited negative healing, also has a significant amount of 2:1 expandable trioctahedral clays. These clays were not measured in LA03749 and LA02422, with instead the presence of 2:1 expandable dioctahedral clays. Why other samples with significant amounts of expandable clays, such as S491I, did not show negative healing is unclear, however. Alternatively, N3583 has more calcite (15.7% by weight, Supplementary Material, Figure S5) than any other sample (no other sample has more than 10% by weight). Because expandable clays absorb  $\text{Ca}^{2+}$  ions, it may be that calcite is dissolved during long hold times in wet conditions and, due to its absorption by clay minerals (which have a negative charge), is not able to be re-precipitated, resulting in loss of strength and negative healing. To test this hypothesis, an experiment on N3583 at 50



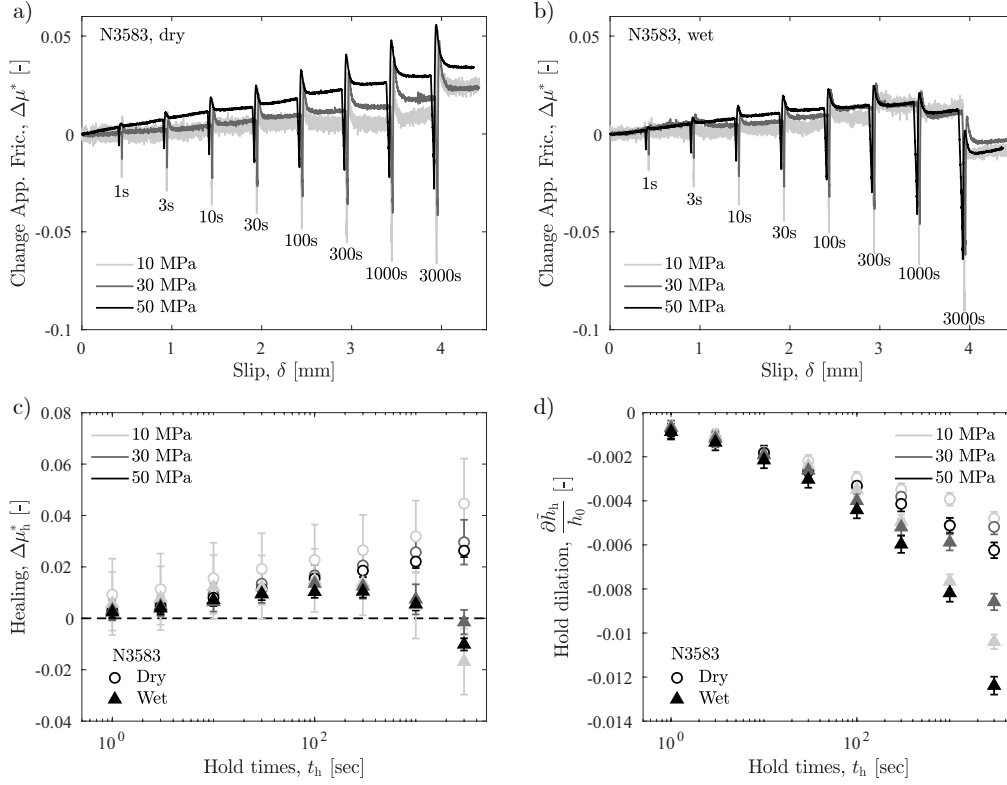


**Figure 9.** Slide-hold-slides for N3583 in both dry (a) and wet (b) conditions. The length of the hold is written under the minimum value of apparent friction reached during each hold. Importantly, this sample exhibits negative frictional healing, but only in wet conditions for large ( $>1000$  seconds) hold times. The (c) healing,  $\Delta\mu_h^*$ , and (d) normalized dilation during the hold,  $\frac{\partial h_h}{h_0}$ , as a function of hold time,  $t_h$ , for these cases (a, b).

616 MPa was run using acid fluid (HCl solution 0.1 M diluted by a factor of ten yielding a  
 617 pH of 2). Negative healing was slightly enhanced, but the difference was within exper-  
 618 imental error such that the test was inconclusive, Supplementary Material, Figure S23.  
 619 XRD analyses, including analyses on the extracted clay fraction, performed on the post-  
 620 mortem sample revealed that calcite concentrations did not change before and after the  
 621 test, nor did the clay mineral species, Supplementary Material, Figure S24 and Table S7.

622 A further possibility may be related to the platy structure of phyllosilicates, which  
 623 cause the accelerated saturation of real contact areas (Saffer & Marone, 2003; Carpen-  
 624 ter et al., 2011; Tesei et al., 2012; Carpenter, Ikari, & Marone, 2016; Ikari et al., 2016;  
 625 Collettini et al., 2019). It may be, for example, that the grain rotation of phyllosilicates  
 626 results in a texture with pronounced preferred orientation during longer holds which in  
 627 turn inhibits or even reduces asperity expansion, ultimately reducing either real contact  
 628 area or the quality of contact, resulting in reduced healing. As dry samples have under-  
 629 gone less cataclasis, larger grains are still intact. For this reason a granular load-bearing  
 630 framework may still be in place in dry experiments, such that real contact still increases  
 631 during long holds and negative healing does not result. Further investigation is clearly  
 632 required.

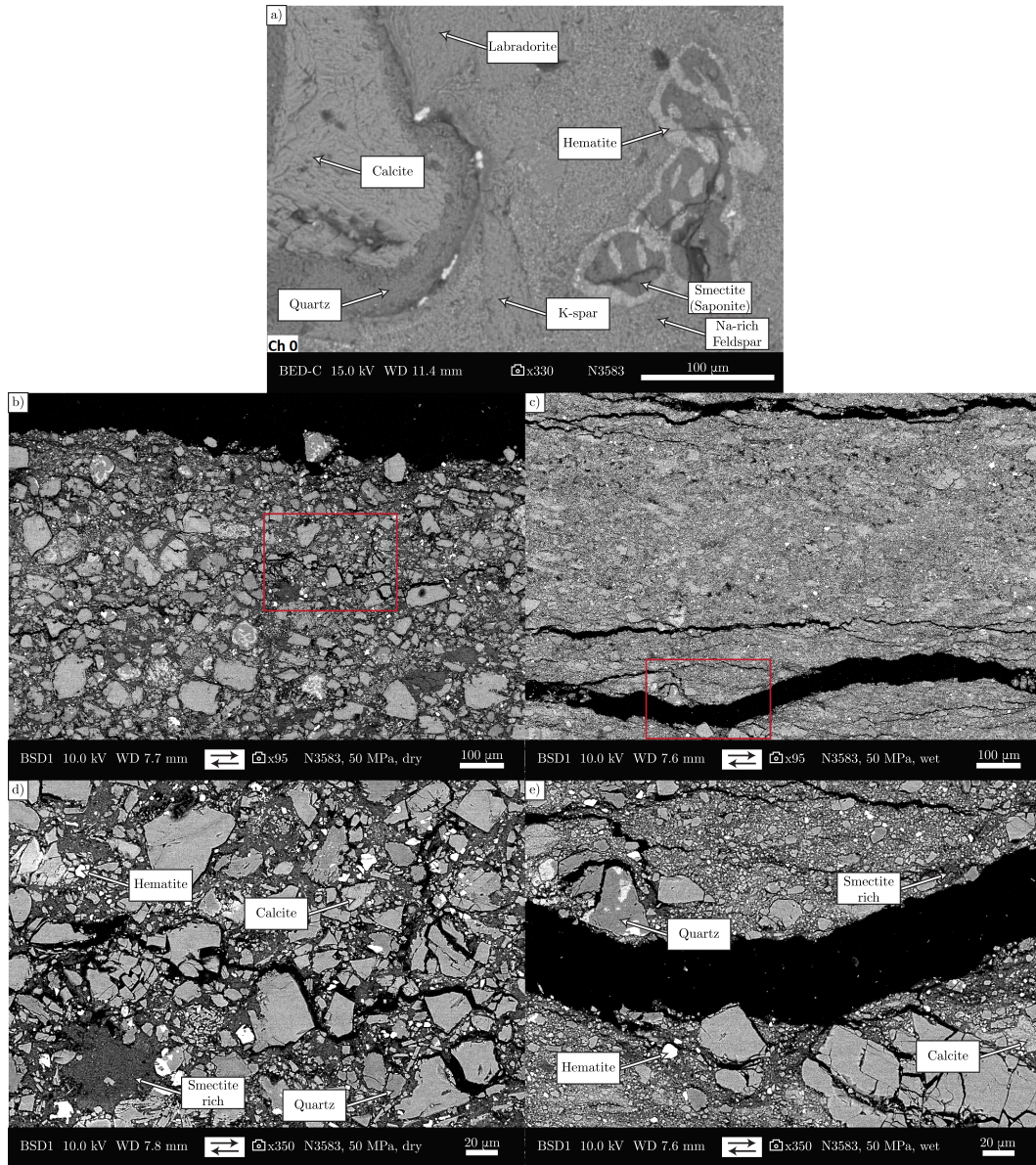


**Figure 10.** a) An intact sample of N3583. (b-e) N3583 deformed at 50 MPa under (b, d) dry conditions and (c, e) wet conditions. N3583 exhibited negative healing under wet conditions. Arrows underneath the images show the far-field shear direction.

633

## 6.2 Velocity dependence and dilatancy

634

635

636

637

638

639

640

641

642

643

When all of the velocity steps are taken together, it can be seen that  $a$  and, in particular,  $b$  do not have a clear relationship with the dilation occurring during the velocity step, Figure 11(a-d). However, the overall velocity dependence,  $a-b$ , does seem to correlate directly with  $\alpha$ , Figure 11(e, f). As seen previously (e.g., Ikari et al. (2009)) the value of  $\alpha$  does not seem to depend on upstep velocity. Indeed in Figure 11 it was not necessary to separate the results based on velocity, with all velocity steps plotted together. Certain samples, in particular those with high phyllosilicate contents, displayed negative values of  $b$ . This is likely due to the saturation of contact area, as previously seen in experiments on phyllosilicate-rich samples (Saffer & Marone, 2003; Ikari et al., 2009; Carpenter, Ikari, & Marone, 2016; Collettini et al., 2019).

644

## 6.3 Frictional healing and dilatancy

645

646

647

648

649

650

651

652

653

654

655

656

657

658

659

660

661

662

663

664

665

666

667

668

669

Generally slightly smaller healing rates are seen at larger normal stresses, Figure 12. However, this trend may be well or poorly pronounced depending on the type of sample. Some samples (in particular those rich in phyllosilicates) do not clearly show this trend at all. Samples also tend to show greater dilation rates at higher normal stresses, maybe counter-intuitively implying that on a per-sample basis more sample compaction during a hold and more sample dilation during reshear yields less healing. This is unexpected as dilatancy should depend on the grain size of the fabric that controls the shear strength (e.g., the boundary shear, in the case of granular materials). At higher stress, less dilation is expected as less grain climbing and rigid body rotation of the grains can be attained without grain fracturing (e.g., Bos and Spiers (2001); Giorgetti et al. (2015)). However, it should be noted that the dilation rates  $B_s$  and  $B_h$  are both normalized by the gouge thickness prior to the start of a hold, which is significantly less at the start of a hold for experiments at higher normal stresses. Indeed, by simply plotting the healing,  $\Delta\mu_h^*$ , versus the dilation upon reshear,  $\partial\tilde{h}_s$ , for all holds performed in all experiments, it can be clearly seen that more dilation corresponds to more healing, Figure 12(a, b). As a matter of fact, normalizing the dilation by layer thickness and replotting results in a less collapsed trend. This implies that the anticorrelation between sample dilation during reshear and healing is an artifact of the normalization and that gouge thickness at the start of a hold is not the correct normalization parameter for dilation rates. It is likely that the correct normalization involves a micro-scale measurement local to the experimental fault and not a macro-scale measurement at the load cells of the machine's pistons. A similar argument can be made for the larger dilation rates seen in wet conditions, as the gouge has a larger tendency to compact under wet conditions. That said, there still exists a positive trend between healing rate and dilation-upon-reshear rate, Figure 12(c, d).

670

## 6.4 The influence of water

671

672

673

674

675

676

677

678

679

680

681

682

683

As previously mentioned, wet samples tend to have compacted more than dry samples at any given landmark in the experiment. Based on microstructure, for example Figures 8 and 10, deforming gouge under wet conditions leads to more distributed cataclasis and a more significant reduction in grain size than when the same sample is deformed at the same normal stress but dry. This is likely due to the increased localization occurring during dry experiments, resulting in large low-strain domains and only local cataclasis. Alternative explanations include local overpressure, the Rehbinder effect, fault lubrication, or general water weakening (e.g., Noël et al. (2021); Noël, Fryer, et al. (2024)) leading to an increased ease in grain sliding; however, it may also be due to the period of sample wetting at the start of all wet experiments. Sample wetting is performed for 40 minutes at low normal stress (1 MPa), but the samples continuously compact during this time. Wet conditions further affect healing rate; however, whether or not healing is increased or decreased in wet conditions is sample dependent. Finally, note here

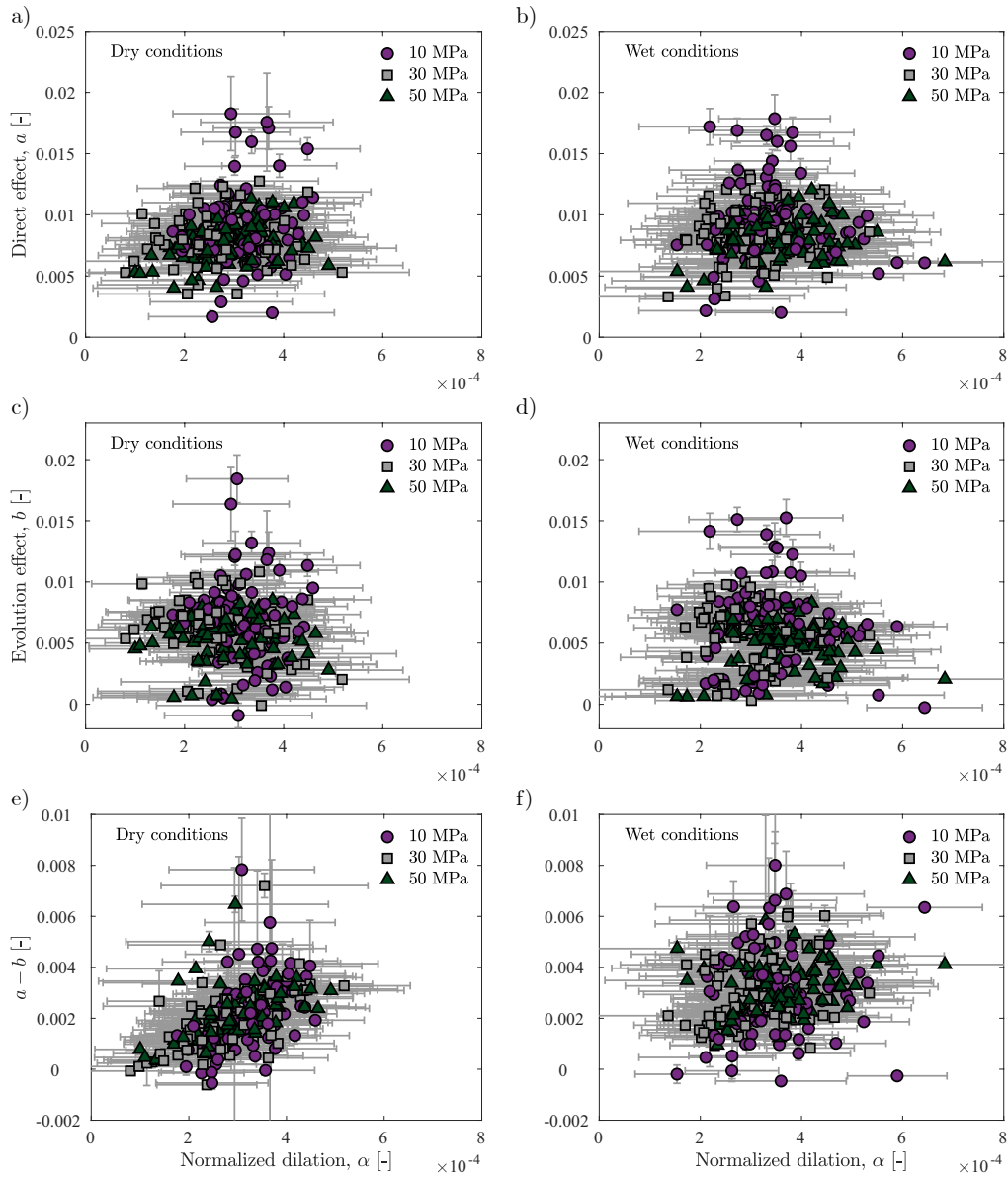


**Figure 11.** A demonstration of how  $a - b$  scales with the normalized dilation upon a velocity step,  $\alpha$ , for (a, c, e) dry and (b, d, f) wet conditions. The correlation between  $\alpha$  and (a, b)  $a$ , (c, d)  $b$ , and (e, f)  $a - b$ . It can be seen that the correlation between  $\alpha$  and  $a - b$  principally stems from  $\alpha$ 's correlation with  $a$ . The more a fault gouge must dilate to increase its sliding velocity the more velocity strengthening that gouge generally is. Velocity steps where either  $a$  or  $b$  was found to be above 0.02 were excluded because they were considered to be anomalous values related to difficulties in keeping a constant normal stress at high velocities.

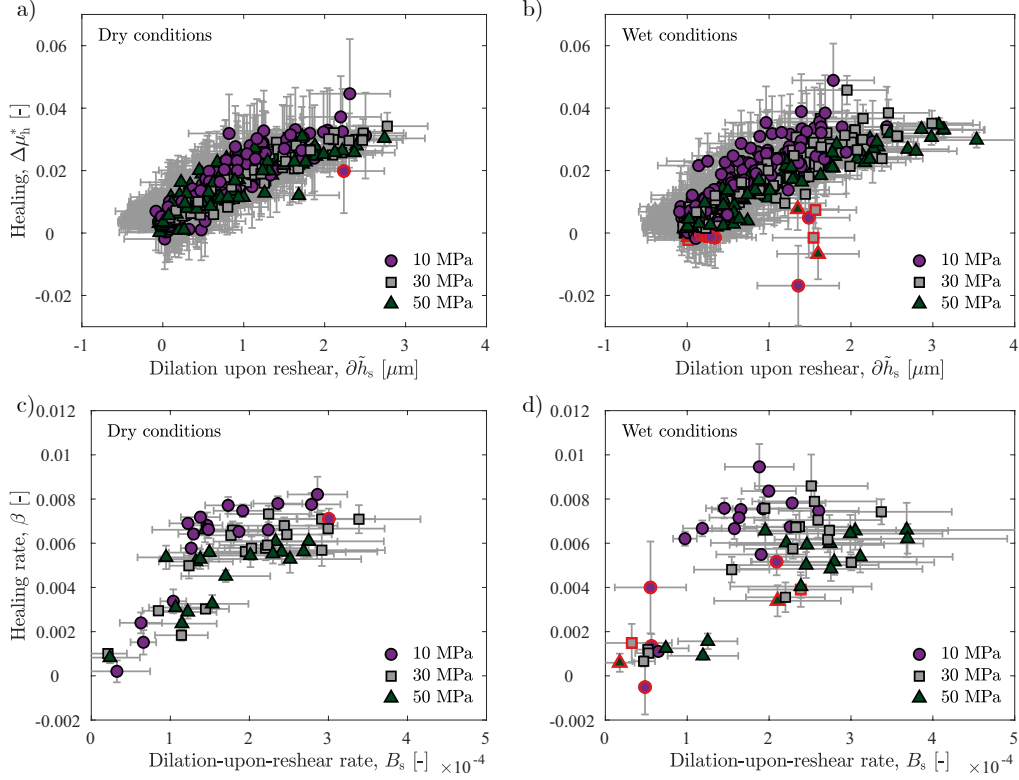


**Figure 12.** (a, b) The healing,  $\mu_h^*$ , versus the dilation upon reshear,  $\partial\tilde{h}_s$ , for holds performed in (a) dry and (b) wet conditions. In the case that the healing is negative (or represents a negative healing rate compared to smaller hold times), the data point is outlined in red. (c, d) The healing rate,  $\beta$ , versus the dilation-upon-reshear rate,  $B_s$ , for experiments performed in (c) dry and (d) wet conditions. In the case that the healing becomes negative for large hold times, the data point is outlined in red.

684 that deionized water was used during the experiments and that pore-fluid chemistry can  
685 affect second-order friction characteristics (e.g., Carpenter, Collettini, et al. (2016)).

## 686 **6.5 The influence of phyllosilicate content**

687 The alteration of volcanic samples can lead to the existence of a variety of phyl-  
688 losilicate minerals within the rock matrix. It has long been recognized that the presence  
689 of phyllosilicate minerals has a tendency to either mechanically or chemically reduce the  
690 frictional resistance of gouge samples, with initial work focusing on soils (Skempton, 1964;  
691 Lupini et al., 1981). More recently, a large number of authors have demonstrated this  
692 phenomenon for a wide variety of conditions, rock types, and gouge compositions (e.g.,  
693 Summers and Byerlee (1977); Logan and Rauenzahn (1987); Moore et al. (1997); Mor-  
694 row et al. (2000); Brown et al. (2003); Saffer and Marone (2003); Moore and Lockner (2004,  
695 2007); Ikari et al. (2009); Tembe et al. (2010); Ikari et al. (2011); Saffer et al. (2012); Te-  
696 sei et al. (2012); Giorgetti et al. (2015); Carpenter, Ikari, and Marone (2016); Fang et  
697 al. (2016); Zhang et al. (2022); Ashman and Faulkner (2023)). Additionally, the frictional  
698 healing (Bos & Spiers, 2000; Carpenter et al., 2011; Tesei et al., 2012; Giorgetti et al.,  
699 2015; Carpenter, Ikari, & Marone, 2016; Ikari et al., 2016; Shreedhara et al., 2022) and  
700 velocity-dependence (Summers & Byerlee, 1977; Giorgetti et al., 2015; Phillips et al., 2020)  
701 of gouge samples has been shown to be influenced by phyllosilicate content.

702 The strong influence of phyllosilicate content on frictional behavior and common  
703 occurrence of phyllosilicates in fault gouge have led to the questioning of the use of unaltered-  
704 rock or monomineralic friction results, without considering phyllosilicate content, to model  
705 natural fault gouge (Bos & Spiers, 2000). This may be particularly true for hydrother-  
706 mal systems where alteration products are common. Indeed, all eighteen samples col-  
707 lected here *in-situ* contain phyllosilicates and other secondary minerals.

708 While the presence of phyllosilicates generally reduces frictional strength, decreases  
709 frictional healing, and promotes velocity-strengthening behavior, different phyllosilicate  
710 minerals produce these effects to a variety of degrees and magnitudes (Summers & By-  
711 erlee, 1977; Morrow et al., 1992; Moore et al., 1997; Morrow et al., 2000; Moore & Lock-  
712 ner, 2004; Ikari et al., 2009). Despite this, direct comparisons between frictional param-  
713 eters and the general phyllosilicate content have been performed on numerous occasions  
714 (e.g., Brown et al. (2003); Tembe et al. (2010); Tesei et al. (2012); Giorgetti et al. (2015)),  
715 and it has further been suggested by some authors that the overall phyllosilicate con-  
716 tent controls the friction coefficient to a first order (Morrow et al., 1992; Brown et al.,  
717 2003; Saffer et al., 2012). Similarly, here, the dynamic friction coefficient is shown to be  
718 a first-order function of phyllosilicate content in andesite-like volcanic rocks from vol-  
719 canic arc settings, despite the wide variety of mineralogies of the samples, Figure 13. It  
720 should be noted that, as shown by other workers mentioned above, different phyllosil-  
721 icate minerals are still expected to have different influences on the friction characteris-  
722 tics of a given gouge. The emphasis here is on the first-order behavior, with a view to  
723 simplify engineering and hazard studies. A less clear trend is also present for the coef-  
724 ficient of frictional yield. The weakening with increased phyllosilicate content is present  
725 in both wet and dry conditions, but is more significant in wet conditions. Generally, the  
726 higher the phyllosilicate content the larger the difference in weakening between wet and  
727 dry conditions, as seen by other authors (Morrow et al., 1992). This trend may reverse  
728 for very large phyllosilicate contents ( $> 0.6$ ), Figure 13f, but it is also likely that the nominally-  
729 dry samples at such high phyllosilicate contents are sufficiently wet (due to, for exam-  
730 ple, room humidity) to behave as (partially) wet samples.

731 Further, as seen by previous workers in other rock types and gouge compositions  
732 (Logan & Rauenzahn, 1987; Niemeijer & Spiers, 2006; Ikari et al., 2007, 2009; Tembe et  
733 al., 2010; Ikari et al., 2011, 2016; Fang et al., 2016; Zhang et al., 2022), the velocity de-  
734 pendence of these andesitic-like volcanic arc samples is affected by phyllosilicate content,

735 Figure 14. The direct effect,  $a$ , slightly decreases with increased phyllosilicate content,  
 736 but the evolution effect,  $b$ , decreases significantly. Overall this results in an increase in  
 737  $a-b$  and therefore increased velocity-strengthening behaviour. A decrease in  $b$  has been  
 738 previously associated with a transition from brittle to "semi-brittle" behaviour (Carpenter,  
 739 Colletini, et al., 2016). The dilation that occurs during a velocity step also generally  
 740 decreases with increasing phyllosilicate content, similar to previous observations (Ashman  
 741 & Faulkner, 2023).

742 Additionally, as shown previously in other rock types (Bos & Spiers, 2000; Carpen-  
 743 ter et al., 2011; Tesei et al., 2012; Carpenter, Ikari, & Marone, 2016; Ikari et al., 2016;  
 744 Shreedhara et al., 2022), the healing rate is reduced in samples with higher phyllosili-  
 745 cate contents, Figure 15. As seen by Bos and Spiers (2000), dilation upon reshear is re-  
 746 duced for higher phyllosilicate contents and might be related to observations of perme-  
 747 ability decrease during shear slip in phyllosilicate-rich crystalline samples (Meng et al.,  
 748 2022).

749 While difficult to constrain precisely, it seems that phyllosilicate content begins hav-  
 750 ing a significant influence on frictional behaviour at weight contents larger than approx-  
 751 imately 20%. Previous operators, in a variety different geological contexts, have reported  
 752 a range of values for the onset of a significant influence of phyllosilicate content. Giorgetti  
 753 et al. (2015) reported that as little as 5% talc content was already enough to significantly  
 754 influence the behaviour of talc-calcite mixtures; whereas Brown et al. (2003) report be-  
 755 haviour similar to that reported here for samples relevant to subduction zones. Similar  
 756 results were also reported by Tembe et al. (2010) for quartz-clay mixtures. Tesei et al.  
 757 (2012) report a still higher value of phyllosilicate content, albeit with a more stringent  
 758 criterion for weakening. While a relative independence of first- and second-order frictional  
 759 behavior on the specific phyllosilicate mineral is generally shown here, this data set lacks  
 760 a sample with a large (>40% by weight) amount of chlorite, such that phyllosilicate-mineral-  
 761 specific behavior may appear for highly-altered chlorite-rich samples. Additionally, it should  
 762 be noted that while the temperature independence of first-order friction characteristics  
 763 is accepted at low (<300 °C) temperatures (e.g., Scholz (2019), ch. 2), second-order fric-  
 764 tion characteristics are often dependent on temperature (e.g., Blanpied et al. (1991); Ko-  
 765 lawole et al. (2019); Jeppson et al. (2023)).

766 The evolution effect,  $b$ , in the measurement of the velocity-dependence of friction  
 767 reflects the evolution and renewal of contact area (Dieterich, 1979; Ikari et al., 2016; Scholz,  
 768 2019). As shown here and elsewhere, phyllosilicate-rich rocks often exhibit very low, or  
 769 even negative, values of  $b$  (Saffer & Marone, 2003; Ikari et al., 2009, 2016). This is be-  
 770 cause clay gouge particles are in complete contact and the contact area does not change  
 771 upon a step in velocity (Saffer & Marone, 2003; Ikari et al., 2016). Interestingly, how-  
 772 ever, it has been shown here that phyllosilicate-rich gouge can also exhibit negative heal-  
 773 ing, likely due to either (1) the saturation and even reduction of real contact area dur-  
 774 ing periods of very low slip velocities (during the hold periods of slide-hold-slides the stress  
 775 reduction is due to slip, despite the far field slip rate being maintained at zero (Marone,  
 776 1998)), or (2) due to a reduction in the quality of contacts, for example through the de-  
 777 velopment of a preferred orientation. Although the sliding velocities during the veloc-  
 778 ity steps performed here and by other operators are too high for this effect to be evident  
 779 during laboratory velocity steps (the time scale of contact renewal due to slip is shorter  
 780 than the time scale for contact area/quality reduction), tectonic strain rates are orders  
 781 of magnitudes lower and may be more comparable to the slip rate during slide-hold-slide  
 782 holds. It may be that, at tectonic strain rates, these phyllosilicate-rich samples would  
 783 undergo contact area/quality reduction as far-field stresses cause mineral reorientation.  
 784 Depending on relative time scales between contact area reduction and contact resatu-  
 785 ration during slip, it may be therefore that - at very low strain rates - these samples ex-  
 786 hibit higher values of  $b$  than those measured in the laboratory, potentially leading to ve-  
 787 locity weakening at tectonic strain rates. Indeed, bulk rate-strengthening phyllosilicate-

rich samples have recently been connected to slow-slipping earthquakes (Volpe et al., 2024). We caution that this phenomenon, while plausible, is highly speculative.

## 6.6 Implications

### 6.6.1 Geothermal reservoirs

Geothermal reservoirs in volcanic arc settings often have a general, albeit simplified, structure consisting of, from shallowest to deepest, a smectite-kaolinite zone, an illite-rich zone, a chlorite-rich zone, and finally a ductile shear zone (Cathelineau & Izquierdo, 1988; Stimac et al., 2015; Verati et al., 2018). Examples of this hydrothermal alteration pattern, either in part or in full, include Bouillante, France (Beauchamps et al., 2019), Terre-de-Haut, France (Beauchamps et al., 2019), the Ogiri Field, Japan (Goko, 2000), Pauzhetskoe geothermal field, Russia (Frolova et al., 2006), Okeanskoe geothermal field, Russia (Frolova et al., 2006), the Cophau geothermal reservoir, Argentina (Barcelona et al., 2019; Yagupsky et al., 2023), Darajat, Indonesia (Rejeki et al., 2010), Cerro Pabellón, Chile (Maza et al., 2018), Tolhuaca, Chile (Melosh et al., 2010; Sanchez-Alfaro et al., 2016), Mount Meager, Canada (Hormozzade Ghalati et al., 2023), and the Awibengkok Geothermal System, Indonesia (Stimac et al., 2008). The literature also contains examples of ductile shear zones acting as vertical fluid barriers (Stimac et al., 2015; Yagupsky et al., 2023) and horizontal fluid conduits (Favier, Lardeaux, Verati, et al., 2021; Favier, Lardeaux, Corsini, et al., 2021). The samples tested here can provide insight into the likely frictional properties of the smectite- and kaolinite-rich, illite-rich, and chlorite-rich zones. In particular, samples B494D, S491I, LA03749, N3808, and N3583 are likely representative of smectite- and kaolinite-rich zones, sample S491B is likely representative of illite-rich zones. G3130 may represent chlorite-rich zones, although the degree of alteration is somewhat low compared to previously-listed examples. LA02541, LA02422, M1430, and N4343 may represent mixed or transitional layers, with multiple types of alteration present. Other samples may be interpreted to represent these zones in cases where the alteration is less developed.

The frictional properties of the samples have been shown to depend, to a first order, on the general phyllosilicate contents of the samples. It is therefore not expected that the different zones mentioned above have significantly different frictional properties based solely on their relative phyllosilicate compositions. This should facilitate the numerical modelling of frictional phenomena in these regions; however, a given geothermal system may have different propensities for producing certain alteration minerals, meaning that high phyllosilicate contents may be more or less likely to be found in a given zone resulting in differing frictional properties depending on the zone being modelled.

The ductile shear zones which provide lateral fluid transport in these settings can only occur when the primary mode of deformation is delocalized or, equivalently, ductile (e.g., Rutter (1986); Knipe and McCaig (1994); Meyer and Violay (2023)). For this to occur, the bulk yield stress of a given rock mass as it experiences a far-field stress must be lower than its frictional strength. As the frictional strength has been shown here and elsewhere to be dependent on the phyllosilicate content of the rock, the localized-to-ductile transition (LDT) is predicted to be dependent on the phyllosilicate content (e.g., Koroknai et al. (2008)), and therefore alteration, of the *in-situ* rock, Figure 16. While increasing phyllosilicate content lowers the frictional strength of fault gouge, it is not necessarily the case that the LDT will occur at a greater stress (and therefore greater depth). Indeed, it may be that the higher the phyllosilicate content the lower the yield stress of the rock. However, there is currently no systematic study of the impact of phyllosilicates on the yield (onset of yield) of volcanic rocks, and the effect of phyllosilicate content on bulk yield stress (which can be expected to be temperature dependent) was only tested here at room temperature. Yet, the LDT depends on the competition between the frictional strength and the yield stress of the material. Hence, despite the apparent decrease



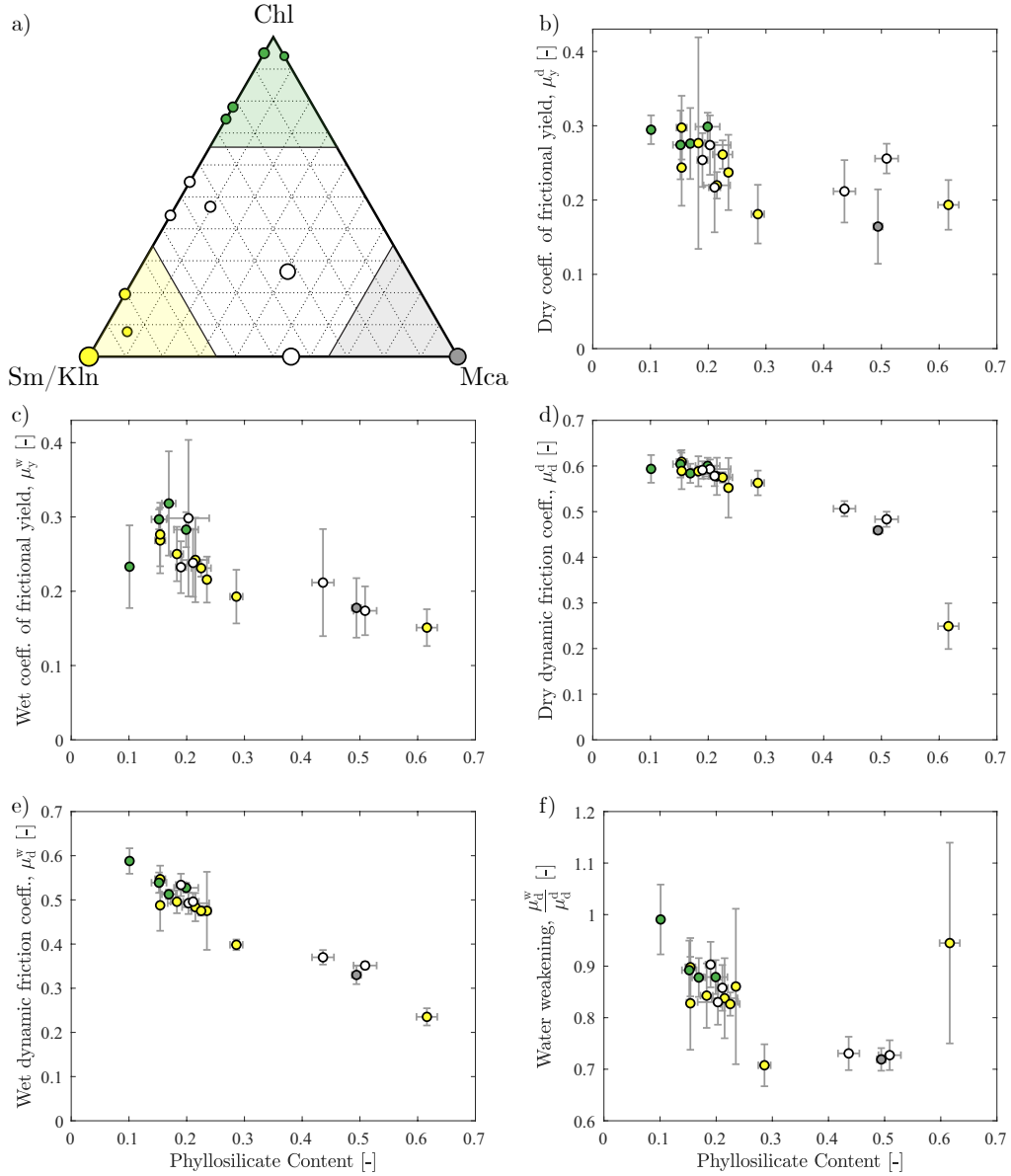


**Figure 13.** a) A ternary diagram illustrating the relative proportions of phyllosilicate minerals, Table 2. For simplicity, 2:1 expandable clays, kaolinite, vermiculite are all grouped together in the category "Sm/Kln"; taken as representative of a smectite- and/or kaolinite-rich zone. Similarly, both dioctahedral and trioctahedral micas are grouped together in the "Mca" category; considered representative of the illite-rich zone, as illites are dioctahedral micas. "Chl" stands for chlorite. A sample is considered to belong to one of these three groups when the relative proportion is greater than 0.67. Samples belonging to the Sm/Kln category are denoted with yellow points, those belonging to the Mca category with grey points, and those belonging to the Chl category with green points. Intermediate cases are left white. The marker size corresponds to the total phyllosilicate content. The (b) dry and (c) wet coefficients of frictional yield. The (d) dry and (e) wet coefficients of dynamic friction as a function of phyllosilicate content for all samples. The coefficients of dynamic friction are calculated as demonstrated in Figure 4. f) The water-induced frictional-strength reduction of the dynamic friction coefficient as a function of the phyllosilicate content.

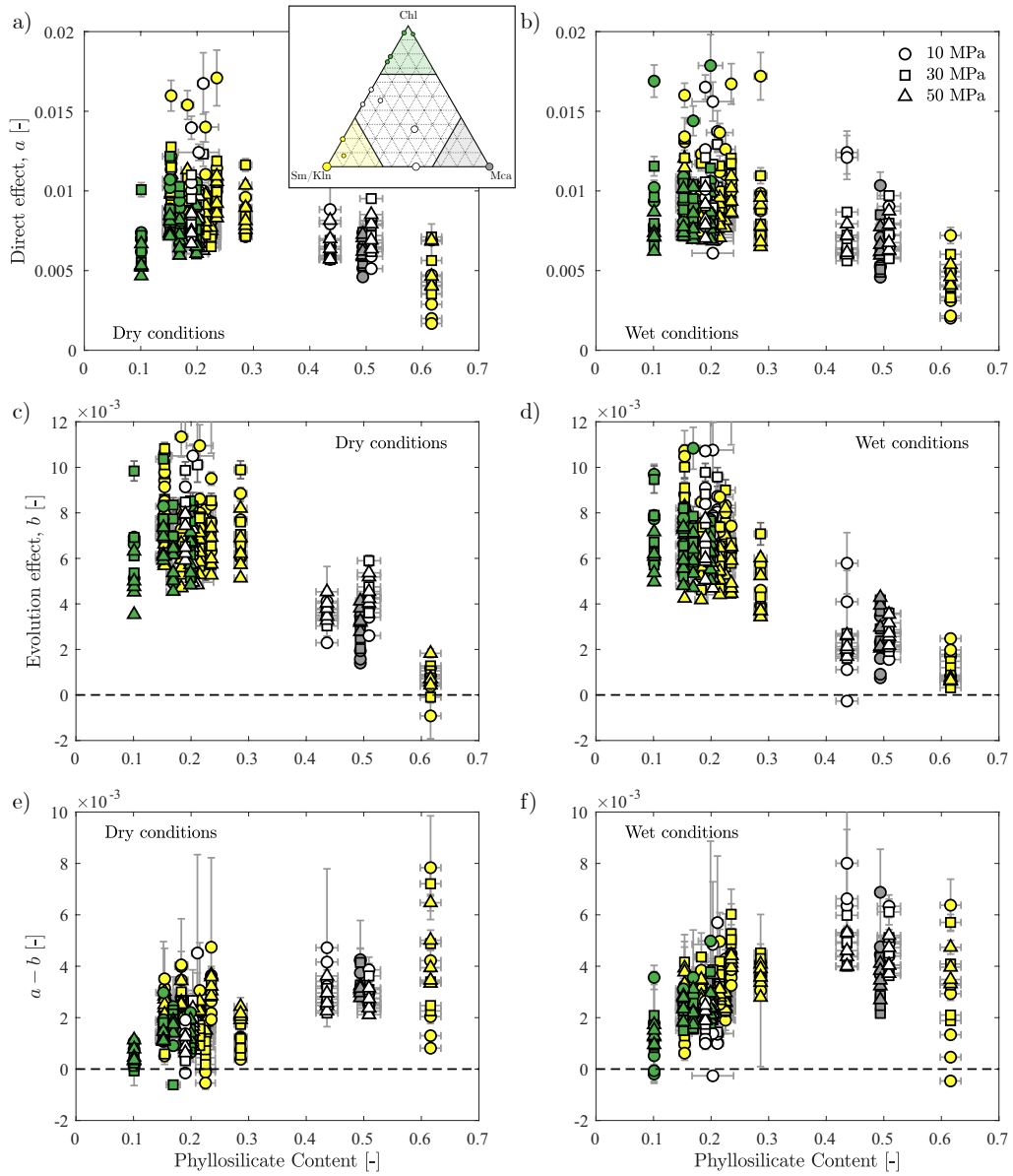


**Figure 14.** The velocity dependence as a function of the phyllosilicate content of each sample. The normal stress of each point is indicated by the shape of the marker. (a, b) The direct effect,  $a$ . (c, d) The evolution effect,  $b$ . (e, f) The velocity dependence,  $a - b$ . The results are shown for dry (a, c, e) and wet (b, d, f) experiments. Points are colored in accordance with Figure 13a (repeated as an inset here in (a)), where yellow is representative of the smectite/kaolinite zone, grey of the illite-rich zone (illites are dioctahedral micas), green of the chlorite-rich zone, and white is intermediate between two or more zones.

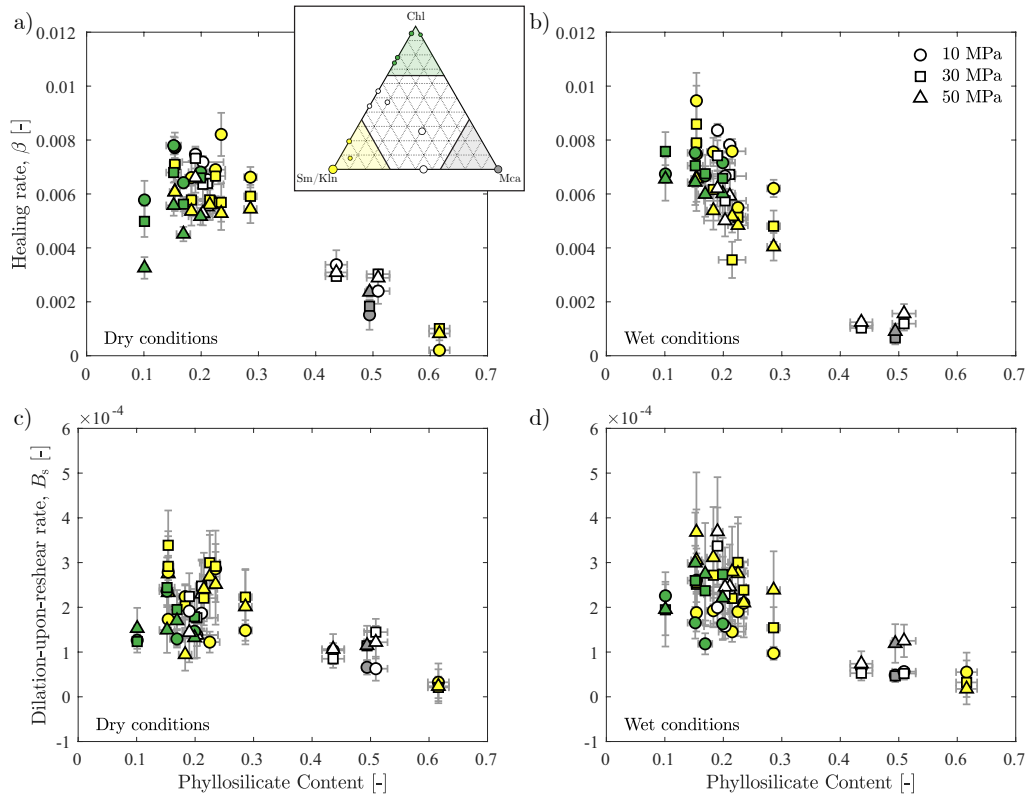


**Figure 15.** (a, b) The frictional healing rate,  $\beta$ , as a function of the phyllosilicate content of each sample in both dry (a) and wet (b) conditions. Note that experiments which exhibited negative healing rates for longer holds are not plotted here. (c, d) The dilation-upon-reshear rate as a function of phyllosilicate content for dry (c) and wet (d) conditions. Points are colored in accordance with Figure 13a (repeated as an inset here in (a)), where yellow is representative of the smectite/kaolinite zone, grey of the illite-rich zone, green of the chlorite-rich zone, and white is intermediate between two or more zones.

839 in frictional yield coefficient with increasing phyllosilicate content (and supporting mi-  
 840 crostructural observations), we are unable to assess the relative impact of clays on fric-  
 841 tional strength and bulk yield stress at reservoir conditions and therefore unable to as-  
 842 sess whether the LDT will shift to shallower or greater depths with increasing alteration.  
 843 It should be noted, however, that alteration resulting in an increased proportion of phyl-  
 844 losilicate minerals has been suggested as a mechanism resulting in a shallower brittle-  
 845 ductile transition along tectonic faults (Shea & Kronenberg, 1992; Imber et al., 2001).

846 The alteration of a given zone is reliant on the ability of hydrothermal fluids to reach  
 847 that zone, typically through fluid conduits such as faults and fractures. It is therefore  
 848 possible that certain zones of a given reservoir remain fairly unaltered. This can be seen,  
 849 for example, in the samples from Lamentin where the relatively unaltered LA03758 oc-  
 850 curs in close proximity to the highly altered LA03749, or in the Tolhuaca-1 wellbore in  
 851 the Tolhuaca Geothermal Field (Melosh et al., 2010). As these reservoirs occur in regions  
 852 which are tectonically active and likely critically stressed, it can be thought that the stress  
 853 present in a given reservoir horizon will depend on the frictional resistance of that hori-  
 854 zon (e.g., Harrison et al. (1954); Brudy et al. (1997); Townend and Zoback (2000); Zoback  
 855 and Townend (2001); Zoback et al. (2002); Evans et al. (2012)). Therefore, zones which  
 856 are frictionally weak will be able to support smaller differential stresses. An implication  
 857 of this idea is the prediction that, in normal-faulting stress regimes (where the maximum  
 858 principal stress is fixed by the overburden), such as that recently active in Les Saintes  
 859 (Verati et al., 2016), the minimum principal stress will be larger in phyllosilicate-rich zones  
 860 and smaller in unaltered zones if the environment is critically stressed, leading to the for-  
 861 mation of stress jumps when altered and unaltered zones are vertically adjacent, Figure 16.  
 862 This has been previously implied for the Soultz-sous-Forêts reservoir (Meller & Kohl, 2014),  
 863 albeit in a different tectonic setting. While stress jumps have been observed and mea-  
 864 sured in a number of instances, particularly in sedimentary basins (e.g., Kry and Gron-  
 865 seth (1983); Teufel (1989); Lucier et al. (2006); Wileveau et al. (2007)), to the authors’  
 866 knowledge they have not yet been observed in a volcanic-arc setting in igneous rock. The  
 867 presence of a stress jump would have significant influence on natural and induced frac-  
 868 ture propagation and containment, as a jump in minimum principal stress can signifi-  
 869 cantly inhibit a propagating fracture (e.g., Adachi et al. (2010)).

870 In summary, it can be expected that, for geo-reservoirs in volcanic arc settings, the  
 871 degree of alteration controls (1) the ability of faults within and around the reservoir to  
 872 nucleate seismic slip (by influencing their velocity dependence; i.e.,  $a-b$ ) as well as their  
 873 sliding strength ( $\mu_d$ ) and strength recovery ( $\beta$ ), (2) the depth of ductile shear zones, which  
 874 are crucial for the horizontal movement of fluid, and (3) the vertical propagation of nat-  
 875 ural and induced fractures through phyllosilicate content’s influence on the minimum prin-  
 876 cipal stress.

### 877 **6.6.2 Seismicity in volcanic arcs**

878 Volcanic arcs are found in areas of active plate tectonics and are therefore likely  
 879 to be seismically-active regions. For example, a significant number of on- and off-shore  
 880 faults in the Guadeloupe archipelago are seismically active and are thought to control  
 881 the volcanic activity, fluid flow, and superficial earthquakes in the area (Verati et al., 2016).  
 882 The results presented here can be used to help with the understanding of active volca-  
 883 noes, where alteration has been previously suggested to potentially lead to explosive vol-  
 884 canic behaviour by reducing the permeability of pore and micro-fracture pathways (Heap  
 885 et al., 2019).

886 Further, geothermal projects are often concerned with induced seismicity. For ex-  
 887 ample, a risk assessment related to induced seismicity has been commissioned for the New-  
 888 berry EGS Demonstration project (Wong et al., 2010). The frictional data presented here  
 889 suggest that zones which are highly-altered and rich in phyllosilicates are less likely to

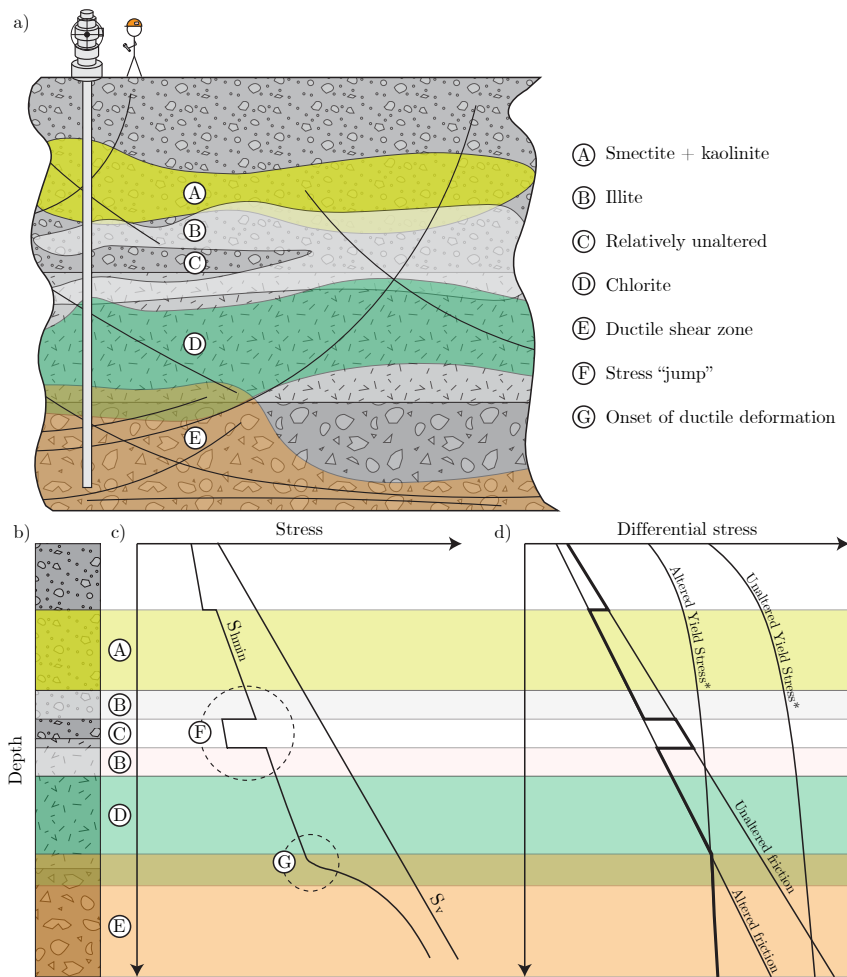


**Figure 16.** An example stress profile and localized-ductile transition resulting from the alteration profiles of a hypothetical geothermal reservoir in a volcanic arc setting. a) A cross-section illustrating the wellpath and the alteration zones present. b) The example stratigraphic profile comprised of (A) a smectite-kaolinite-rich zone, (B) an illite-rich zone, (C) an unaltered zone, (D) a chlorite-rich zone, and (E) a ductile shear zone. Note the faults/fractures represented by black curved lines. The presence of these fluid conduits allows for alteration to occur in these zones. The unaltered zone, which may be equivalently present within the clay cap or chlorite-rich zone, is a result of the lack of faults and fractures crossing this zone. Further note that the ductile shear zone does not necessarily coincide with the end of the chlorite-rich zone. c) The stress profile in a normal-faulting stress regime. The vertical stress increases linearly with depth. As these zones are often critically-stressed, the magnitude of the minimum horizontal stress depends on the friction coefficient. In altered zones, phyllosilicate content is high and the differential stress is low. This may result in stress jumps (F). The onset of the localized to ductile transition will result in a relative increase in the minimum horizontal stress (G). d) The differential stress as a function of depth based on frictional strength and yield stress of each zone. The ductile to localized transition begins when the frictional strength is larger than the yield stress (Rutter, 1986; Meyer et al., 2019). The frictional strength of the rock has been shown here to depend on the phyllosilicate content, meaning alteration may affect the depth of the localized-to-ductile transition and therefore the depth of the ductile shear zone and its proximity to the acting geothermal reservoir. Note that the yield stresses of the samples were not measured here at reservoir conditions and likely also depend on alteration.

890 produce a large seismic event, despite being frictionally weak (Meller & Kohl, 2014; Fang  
 891 et al., 2016). However, slip induced in these zones may act to transfer stress to a stronger,  
 892 less-altered patch of a given fault. In general, care should be taken to contain the foot-  
 893 print of a given operation to as small a region as possible within a phyllosilicate-rich zone.  
 894 This not only means limiting pore pressure increases to a small region, but also ensur-  
 895 ing that aseismic-slip and thermo- and poro-elastic stress changes associated with fluid  
 896 injection and stress transfer due to fault slip are also constrained.

## 897 7 Conclusion

898 The frictional properties of eighteen core and surface samples from five geother-  
 899 mal reservoirs in volcanic arc settings have been explored through 108 biaxial experiments.  
 900 It has been shown that, despite the previously-demonstrated differences in the frictional  
 901 behaviour of different phyllosilicate minerals in monomineralic experiments, the over-  
 902 all combined phyllosilicate content controls the frictional behaviour in these settings to  
 903 a first order. This simplification may facilitate the numerical modelling of these geother-  
 904 mal reservoirs which often have stratified alteration zones in which different phyllosil-  
 905 icate minerals dominate. Specifically, larger phyllosilicate contents result in reduced fric-  
 906 tional strength, an increased tendency for velocity-strengthening behaviour, and reduced  
 907 frictional healing. Further, negative healing was observed, in particular in one sample  
 908 which was rich in calcite and 2:1 expandable trioctahedral clays under wet conditions  
 909 (deionized water), and warrants further investigation. The faults and fracture networks  
 910 which make up these reservoirs are often rooted in ductile shear zones, crucial for the  
 911 horizontal advection of geothermal fluids, and it is suggested here that the depth of on-  
 912 set for these zones will depend on the level of alteration and may therefore shift in time  
 913 as alteration continues. Finally, the critically-stressed nature of these reservoirs and the  
 914 varying degrees of alteration in their constituent horizons implies that stress jumps may  
 915 develop, with important implications for fracture propagation.

## 916 Appendix A Field histories

### 917 *A01 Les Saintes*

918 The western coast of Basse Terre on the island of Guadeloupe presents a number  
 919 of hydrothermal expressions near the town of Bouillante, including hot springs, mud pools,  
 920 steaming ground, and fumaroles (Correia et al., 2000). This led to geothermal exploration  
 921 of the area by the BRGM in the 1960's (Jaud & Lamethe, 1985) and ultimately the drilling  
 922 of four exploration wells by Eurafrep and la Société de Production d'Electricité de Guade-  
 923 loupe (SPDEG) between 1969 and 1977 (Jaud & Lamethe, 1985). These wells encoun-  
 924 tered high-temperature conditions (approximately 245°C), but only one well (BO-2) showed  
 925 potential for economical steam production (Jaud & Lamethe, 1985; Correia et al., 2000).  
 926 Two other wells were plugged and a fourth, deeper well (BO-4) was deemed to have too  
 927 low of a productivity to warrant production (Correia et al., 2000). Initially, only BO-  
 928 2 was connected to a 4.7 MWe-capacity power plant which was brought online in 1987  
 929 (Correia et al., 2000). Following a slight decline in production from BO-2, BO-4 was stim-  
 930 ulated with the injection of cold fluid; while the area was monitored for induced seismic-  
 931 ity during the stimulation activities, no seismic events were recorded (Correia et al., 2000).  
 932 In 2001, three further wells were drilled from the platform of BO-4. Two of these wells  
 933 (BO-5 and BO-6) were connected to a new geothermal power plant, raising the produc-  
 934 tivity of the field to 15 MWe (Mas et al., 2006). The geothermal field is comprised of pre-  
 935 dominately andesitic volcanic horizons (Bouchot et al., 2010), and is considered to be  
 936 located at the junction between a major transcurrent fault and a perpendicular network  
 937 of steeply-dipping normal faults (Verati et al., 2014; Navelot et al., 2018).

938 Les Saintes is an island archipelago of Guadeloupe located South of Basse Terre,  
 939 Figure A1. One of its principal islands, Terre-de-Haut, is considered to contain outcrops

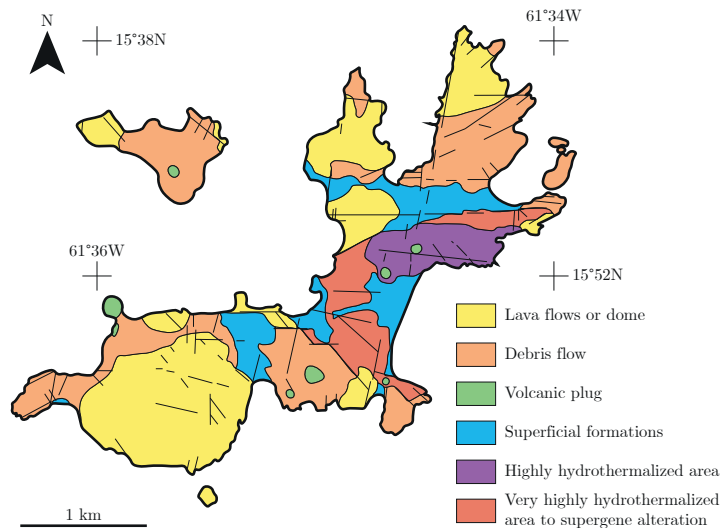


**Figure A1.** A geological map of Terre-de-Haut; modified from Favier, Lardeaux, Verati, et al. (2021). Les Saintes samples are taken from the central very highly hydrothermalized area.

940 which represent an exhumed geothermal paleo-system, active between 2.4 and 2.0 Ma,  
 941 which may act as an analogue for the modern-day Bouillante geothermal reservoir (Verati  
 942 et al., 2016; Navelot et al., 2018; Favier, Lardeaux, Verati, et al., 2021). While there have  
 943 been no exploration wells drilled in this area, it is thought that the paleo-gradient was  
 944 likely in the range of 90 to 140  $\frac{^{\circ}\text{C}}{\text{km}}$ , with the deepest part of the paleo-reservoir at ap-  
 945 proximately 2.5 km (Favier, Lardeaux, Verati, et al., 2021). The present day geother-  
 946 mal gradient of the area is not known, but near the Gaudeloupe archipelago a gradient  
 947 in the range of 69 to 98  $\frac{^{\circ}\text{C}}{\text{km}}$  may be considered reasonable (Manga et al., 2012).

#### 948 **A02 Lamentin**

949 The presence of thermal springs in the area of Le Lamentin motivated a first geother-  
 950 mal exploration phase in the late 1960s (Gadalia et al., 2014), with a relatively deep ex-  
 951 ploration well, LA-101, drilled in 1970 to a depth of 771 m; this well presented a max-  
 952 imum temperature of approximately 90°C at 250 m depth (Genter et al., 2002). Sub-  
 953 sequent surface investigations and drilling programs in the 1980's and early 2000's fur-  
 954 ther explored the area (Gadalia et al., 2014). In particular, three exploratory wells were  
 955 drilled in 2001 by the Compagnie Française de Géothermie (CFG) with the goal of in-  
 956 vestigating the possibility of developing a high-enthalpy reservoir at depth and to im-  
 957 prove the data coverage of the existing geothermal reservoir between 200 and 400 me-  
 958 ters depth (Genter et al., 2002). Accompanying this drilling program was a scientific pro-  
 959 gram headed by the Bureau de Recherches Géologiques et Minières (BRGM) (Sanjuan,  
 960 Genter, et al., 2002). Ultimately, this exploration program found that there was no ma-  
 961 jor evidence of a high-temperature geothermal reservoir. However, while this system is  
 962 a low-temperature hydrothermal system with a maximum recorded temperature of ap-  
 963 proximately 90°C, evidence (such as clay mineral structure, for example) of a fossil high-  
 964 temperature system is present (Genter et al., 2002; Mas et al., 2003). Additionally, while  
 965 there are currently no active geothermal wells at Lamentin, a new round of investiga-  
 966 tions has begun to probe key uncertainties regarding the geothermal system with the hope  
 967 of updating its conceptual model and proposing new sites for exploration (Gadalia et al.,  
 968 2019). To this end, cores from two of the three exploration wells drilled in the early 2000's  
 969 are used in this study, Figure A2.

970 The Habitation Carrère well, also known as LA02, was drilled in an area of ther-  
971 mal springs. The drilling was performed in a destructive manner until a depth of 386.7  
972 m after which the well was cored to a depth of 816.15 m (Genter et al., 2002; Mas et al.,  
973 2003). LA02422 comes from a permeable zone characterized by mud losses (between the  
974 depths of 412 and 428 meters) which is also considered to be one of the main aquifers  
975 of this well (Genter et al., 2002; Sanjuan, Traîneau, et al., 2002). The bottom hole tem-  
976 perature of this well was 47°C at the time of measurement. Further measurements at  
977 100 m and 350-375 m indicate temperatures of 40°C and 50°C, respectively (Genter et  
978 al., 2002).

979 The Californie Well, also known as LA03, was drilled destructively to 398.14 m and  
980 then cored to 1000.25 m (Genter et al., 2002). The maximum temperature of this well  
981 is thought to be 88°C at around 400 meters depth; temperature below this depth is slightly  
982 lower, with a bottom-hole temperature reading of 83°C at 997 m (Genter et al., 2002).  
983 The formations encountered by this well are more permeable but less fractured than those  
984 in the Carrère well (Genter et al., 2002).

### 985 ***A03 Mount Meager***

986 In the Mount Meager area, the Meager Creek Hot Springs were first drilled in 1974  
987 as part of a scientific project aimed at investigating local thermal springs (Jessop, 2008).  
988 These initial shallow wells then led to the drilling of deeper exploration wells in the early  
989 1980's. These wells encountered temperatures sufficient for a producing geothermal sys-  
990 tem (approximately 290°C at 3000 m), but the flow rates were deemed insufficient for  
991 economic power production (Jessop, 2008). Further drilling occurred in the 1990's and  
992 2000's, including three cored holes drilled in 2001 and 2002. One of these cored holes,  
993 M-17, Figure A3, was drilled to a total depth of 1186 m and exhibited a maximum tem-  
994 perature of 197°C at 1100 m depth (Jessop, 2008). The other two wells both recorded  
995 temperatures of over 200°C (Jessop, 2008). Despite these results, and further deeper drilling  
996 in the mid-2000's, power production never materialized beyond a pilot geothermal power  
997 facility. Interest has recently been renewed in Mount Meager, however, with Geoscience  
998 BC and the Geological Survey of Canada commissioning a study to reduce exploration  
999 risk for geothermal energy associated with volcanic systems of Canada (Grasby et al.,  
1000 2020; Hormozzade Ghalati et al., 2023).

### 1001 ***A04 Summerland Basin***

1002 In 1990, the EPB/GSC495 well was drilled to a depth of 712 m in the Summer-  
1003 land Basin, Figure A4, being cored from 544 to 712 m (Church et al., 1990; Jessop, 2008).  
1004 This well was extended and cored in 1992 to a depth of 956 m (Jessop, 2008). The orig-  
1005 inal purpose of this wellbore was exploratory geothermal research; however the highest  
1006 temperature recorded in the well was approximately 41°C at 946.5 m (Jessop, 2008). Al-  
1007 though the temperatures measured were sufficient for the low-temperature geothermal  
1008 system proposed, no usable water was found and the project was largely abandoned (Jessop,  
1009 2008). The cores have since been stored at the Geological Survey of Canada - Calgary  
1010 core storage facility. Indeed, this region has long been thought to be a potential geother-  
1011 mal resource (e.g., Jessop (2008) and references within), and, with renewed interest in  
1012 geothermal energy, British Columbia is being revisited with an aim to reduce the explo-  
1013 ration risk for geothermal resources associated with volcanic systems (e.g., Grasby et al.  
1014 (2022)).

### 1015 ***A05 Newberry***

1016 The Newberry Volcano cores used in this study were taken from an exploratory well  
1017 (GEO N-2, sometimes referred to as GNC-2) drilled by Geo Newberry Crater, Inc. to  
1018 a depth of approximately 1370 m and with a maximum temperature of 167°C (Walkey



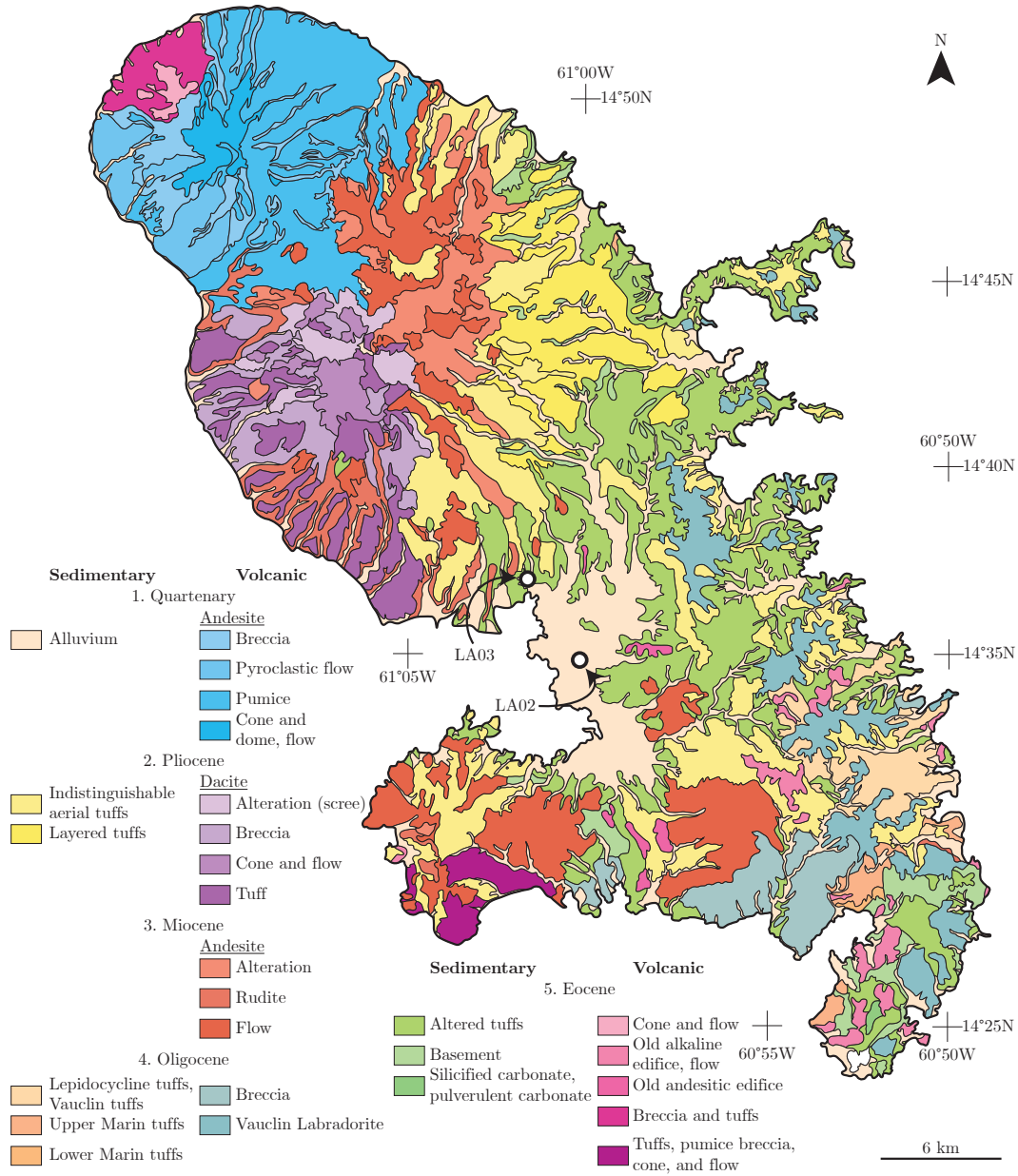


**Figure A2.** A geological map of Martinique with the locations of the wells LA02 and LA03 marked; modified from IRD (2014); Zaiss (2014). Well locations from Sanjuan, Traineau, et al. (2002); Mas et al. (2003).

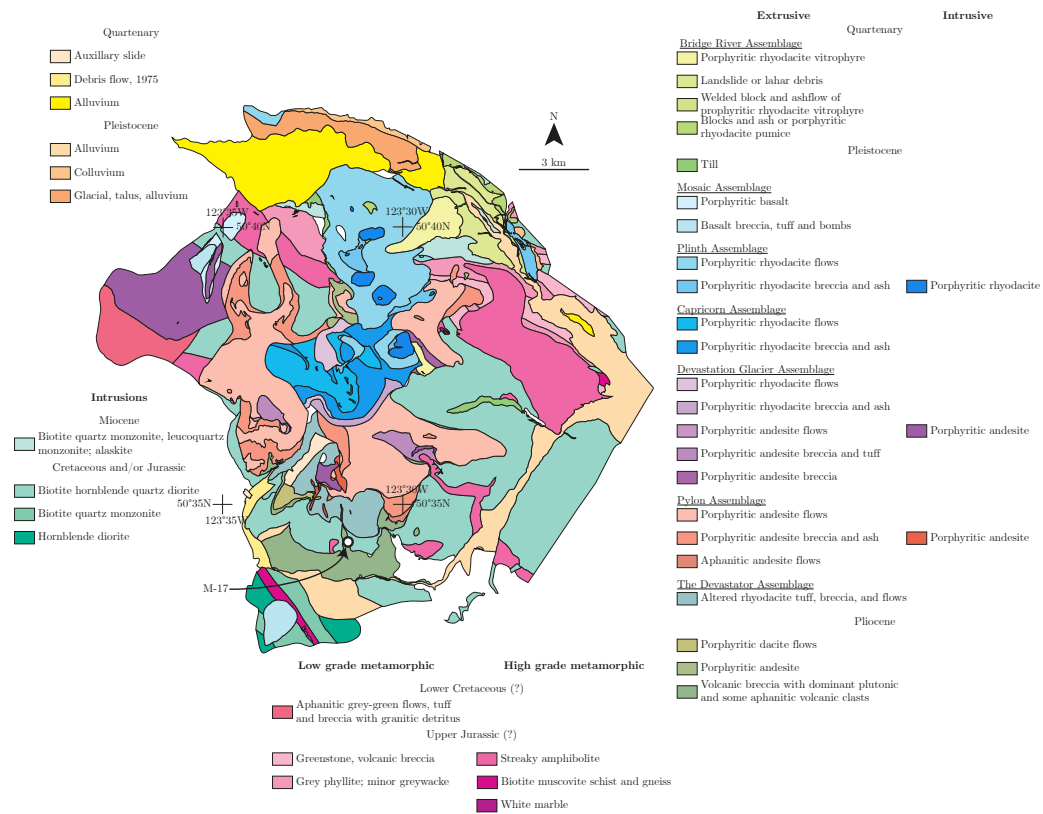


**Figure A3.** A geological map of Meager Creek Geothermal Area with the location of the well M-17 marked; modified from Read (1979). Well location from Ghomshei et al. (2004).

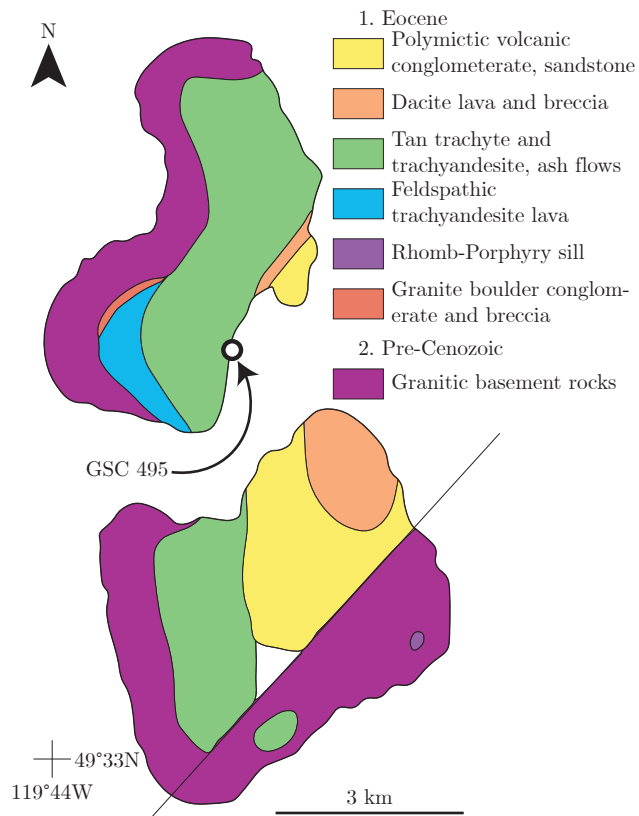


**Figure A4.** A geological map of the Summerland Basin well location with the location of GSC 495 marked; modified from Church et al. (1990).

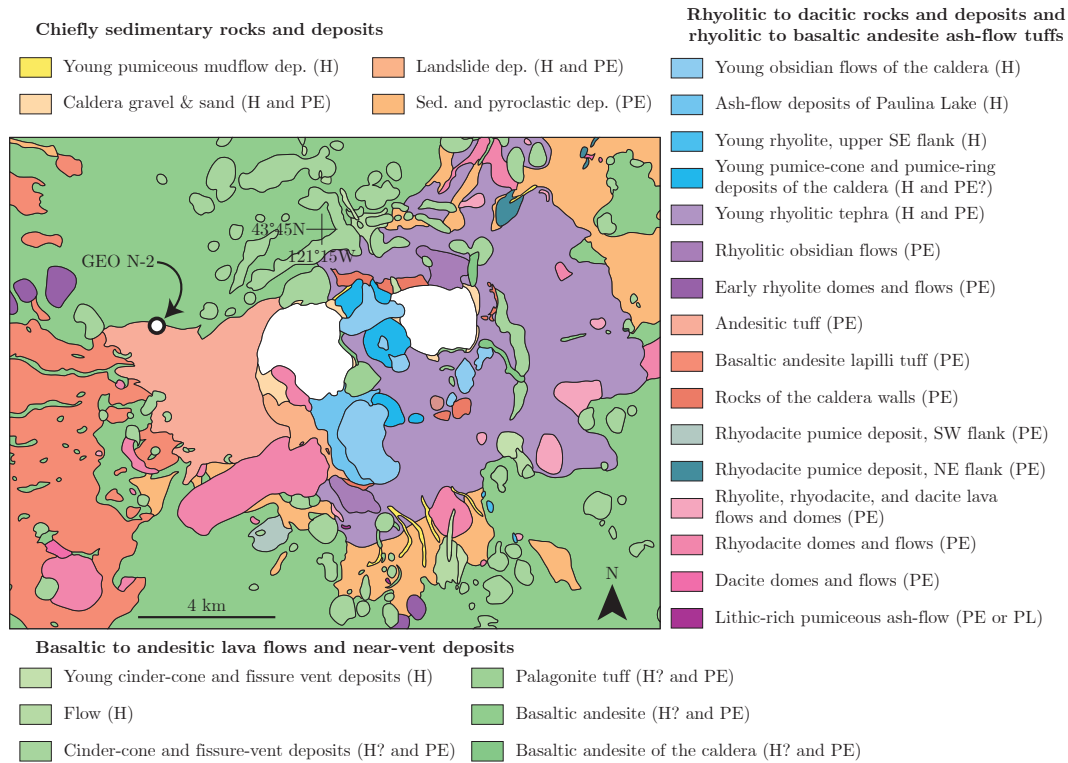


**Figure A5.** A geological map of Newberry Volcano with the location of the well GEO-N2 marked; modified from MacLeod et al. (1995). The age abbreviations are H for Holocene, PE for Pleistocene, and PL for Pliocene.

1019 & Swanberg, 1990; Ayling et al., 2012). This well is located approximately 2.8 km from  
 1020 the western flank of the Newberry caldera and was one of a number of exploratory wells  
 1021 drilled in the area (Bargar & Keith, 1999). Core from the GEO N-2 well has been pre-  
 1022 viously described by Bargar and Keith (1999) and used in fracture characterization (Ayling  
 1023 et al., 2012), geophysical (Fetterman & Davatzes, 2011), and geomechanical (Li et al.,  
 1024 2012; Wang et al., 2016) studies among others.

1025 Approximately 30 years after the drilling of GEO N-2, in 2008 a further well NWG  
 1026 55-29, located approximately 1 km from GEO N-2, Figure A5, was drilled and targeted  
 1027 for shear stimulation by AltaRock Energy (Cladouhos et al., 2016). This well was drilled  
 1028 to a measured depth of 3067 m and recorded an equilibrated static bottom hole temper-  
 1029 ature of 331°C (Cladouhos et al., 2016). Shear stimulation occurred across of 1200-meter  
 1030 stretch of uncased hole (Fang et al., 2016), and concerns about related induced seismic-  
 1031 ity, have led AltaRock Energy to commission a risk assessment report related to induced  
 1032 seismicity (Wong et al., 2010) and perform seismic monitoring (Cladouhos et al., 2013).  
 1033 The potential for induced seismicity due to this project has been the subject of labora-  
 1034 tory studies using core from NWG 55-29 (Fang et al., 2016).

1035

### **Conflict of Interest**

1036

1037

1038

1039

1040

1041

1042

1043

The authors BF and GM are funded by AltaRock Energy who also provided five cores for this study from the GEO N-2 well, a well located near to and relevant for the Newberry EGS Demonstration Project run by AltaRock Energy. The frictional properties of their samples have implications for the potential of induced seismicity related to the Newberry EGS Demonstration Project, an issue of concern for AltaRock Energy. Similarly, SG is employed by the Geological Survey of Canada who are actively investigating the geothermal potential of the Mount Meager Volcanic Complex and provided five cores for this study.

## 1044 Appendix B Open Research

1045 The raw data files, the MATLAB scripts used to treat them, and the resulting data  
 1046 summaries have been made available online for the samples from the Lesser Antilles Vol-  
 1047 canic Arc (Fryer et al., 2024b) and the Cascade Volcanic Arc (Fryer et al., 2024a).

## 1048 Acknowledgments

1049 BF and GM acknowledge funding from AltaRock Energy. MV acknowledges support by  
 1050 the European Research Council Starting Grant project 757290-BEFINE.

1051 The authors would like to thank Laurent Morier, Michael Monnet, Michel Teuscher,  
 1052 Laurent Gastaldo, and Carolina Giorgetti for their help and guidance with the mechan-  
 1053 ical aspects of the HighSTEPS apparatus, and Felix Aeschmann and Lukas Koepfli for  
 1054 their help with the HighSTEPS software. Lionel Sofia is thanked for performing the gran-  
 1055 ulometric analysis. Youness Zangui and Thin Section Lab are thanked for their careful  
 1056 preparation of the thin sections. Amaury Annoye and Yasser Tahiri are thanked for their  
 1057 help in the grinding of five of the samples. Grégoire Baroz and Daniel Beaufort are ac-  
 1058 knowledged for their help in using the SEM at EPFL and the Université de Poitiers, re-  
 1059 spectively. The Geological Survey of Canada, AltaRock Energy, Geoffrey Garrison, and  
 1060 Bernard Sanjuan are recognized for their willingness to provide samples. Quaise Energy  
 1061 and Carlos Araque are acknowledged. Randy Hughes is thanked for help providing data  
 1062 for the Mount Meager geological map and Corentin Noël is thanked for his helping pre-  
 1063 pare it.

1064 XRD analyses were performed on the instruments from the Mineralogy platform  
 1065 of the Institut des Sciences de la Terre (ISTerre – Grenoble, France), which is part of Labex  
 1066 OSUG@2020 (ANR10-LABX56).

1067 The two reviewers, Brett Carpenter and Telemaco Tesei, and an anonymous asso-  
 1068 ciate editor are thanked for their insightful comments and feedback.

## 1069 References

- 1070 Adachi, J., Detournay, E., & Peirce, A. (2010). Analysis of the classical pseudo-3D  
 1071 model for hydraulic fracture with equilibrium height growth across stress barriers. *International Journal of Rock Mechanics & Mining Sciences*, *47*, 625-639.  
 1072 doi: 10.1016/j.ijrmms.2010.03.008  
 1073  
 1074 Ashman, I., & Faulkner, D. (2023). The effect of clay content on the dilatancy  
 1075 and frictional properties of fault gouge. *Journal of Geophysical Research: Solid*  
 1076 *Earth*, *128*. (<https://doi.org/10.1029/2022JB025878>)  
 1077  
 1078 Ayling, B., Rose, P., Petty, S., Zemach, E., & Drakos, P. (2012). QEMSCAN (quan-  
 1079 titative evaluation of minerals by scanning electron microscopy): Capability  
 1080 and application to fracture characterization in geothermal systems. In *Proceed-*  
 1081 *ings: Thirty-Seventh Workshop on Geothermal Reservoir Engineering, Stanford*  
 1082 *University, Stanford, California, January 30 - February 1, 2012*.  
 1083  
 1084 Barcelona, H., Yagupsky, D., & Agosto, M. (2019). The layered model of  
 1085 the Copahue geothermal reservoir, Argentina. *Geothermal Energy*, *7*.  
 1086 (<https://doi.org/10.1186/s40517-019-0124-9>)  
 1087  
 1088 Bargar, K., & Keith, T. (1999). *Hydrothermal mineralogy of core geothermal drill*  
 1089 *holes at newberry volcano, oregon* (No. 1578).  
 1090  
 1091 Beauchamps, G., Ledésert, B., Hébert, R., Navelot, V., & Favier, A. (2019).  
 1092 The characterisation of an exhumed high-temperature paleo-geothermal  
 system on Terre-de-Haut Island (the Les Saintes archipelago, Guade-  
 loupe) in terms of clay minerals and properties. *Geothermal Energy*, *7*.  
 (<https://doi.org/10.1186/s40517-019-0122-y>)  
 Berthé, D., Choukroune, P., & Jegouzo, P. (1979). Orthogneiss, mylonite and non

- 1093 coaxial deformation of granites: the example of the South Armoricain Shear  
1094 Zone. *Journal of Structural Geology*, *1*, 31-42. (<https://doi.org/10.1016/0191->  
1095 8141(79)90019-1)
- 1096 Blanpied, M., Lockner, D., & Byerlee, J. (1991). Fault stability inferred from granite  
1097 sliding experiments at hydrothermal conditions. *Geophysical Research Letters*,  
1098 *18*, 609-612. (<https://doi.org/10.1029/91GL00469>)
- 1099 Bos, B., & Spiers, C. (2000). Effect of phyllosilicates on fluid-assisted healing of  
1100 gouge-bearing faults. *Earth and Planetary Science Letters*, *184*, 199-210.  
1101 ([https://doi.org/10.1016/S0012-821X\(00\)00304-6](https://doi.org/10.1016/S0012-821X(00)00304-6))
- 1102 Bos, B., & Spiers, C. (2001). Experimental investigation into the microstructural  
1103 and mechanical evolution of phyllosilicate-bearing fault rock under conditions  
1104 favoring pressure solution. *Journal of Structural Geology*, *23*, 1187-1202.  
1105 ([https://doi.org/10.1016/S0191-8141\(00\)00184-X](https://doi.org/10.1016/S0191-8141(00)00184-X))
- 1106 Bouchot, V., Sanjuan, B., Traineau, H., Guillou-Frottier, L., Thinon, I., Baltassat,  
1107 J., ... Lasne, E. (2010). Assessment of the Bouillante Geothermal Field  
1108 (Guadeloupe, French West Indies): Toward a conceptual model of the high  
1109 temperature geothermal system. In *Proceedings World Geothermal Congress*  
1110 *2010*.
- 1111 Boulton, C., Carpenter, B., Toy, V., & Marone, C. (2012). Physical proper-  
1112 ties of surface outcrop cataclastic fault rocks, Alpine Fault, New Zealand.  
1113 *Geochemistry Geophysics Geosystems*, *13*. doi: [https://doi.org/10.1029/](https://doi.org/10.1029/2011GC003872)  
1114 2011GC003872
- 1115 Brown, K., Kopf, A., Underwood, M., & Weinberger, J. (2003). Compositional and  
1116 fluid pressure controls on the state of stress on the Nankai subduction thrust:  
1117 A weak plate boundary. *Earth and Planetary Science Letters*, *214*, 589-603.  
1118 ([https://doi.org/10.1016/S0012-821X\(03\)00388-1](https://doi.org/10.1016/S0012-821X(03)00388-1))
- 1119 Browne, P. (1978). Hydrothermal alteration in active geothermal  
1120 fields. *Annual Review of Earth and Planetary Sciences*, *6*, 229-250.  
1121 (<https://doi.org/10.1146/annurev.ea.06.050178.001305>)
- 1122 Brudy, M., Zoback, M., Fuchs, K., Rummel, F., & Baumgärtner, J. (1997). Esti-  
1123 mation of the complete stress tensor to 8 km depth in the KTB scientific drill  
1124 holes: Implications for crustal strength. *Journal of Geophysical Research*, *102*,  
1125 18453-18475. ([10.1029/96JB02942](https://doi.org/10.1029/96JB02942))
- 1126 Byerlee, J. (1968). Brittle-ductile transition in rocks. *Journal of Geophysical Re-*  
1127 *search*, *73*, 4741-4750. (<https://doi.org/10.1029/JB073i014p04741>)
- 1128 Cameli, G., Dini, I., & Liotta, D. (1993). Upper crustal structure of the Larderello  
1129 geothermal field as a feature of post-collisional extensional tectonics (Southern  
1130 Tuscany, Italy). *Tectonophysics*, *224*, 413-423. (<https://doi.org/10.1016/0040->  
1131 1951(93)90041-H)
- 1132 Carpenter, B., Collettini, C., Viti, C., & Cavallo, A. (2016). The influence of  
1133 normal stress and sliding velocity on the frictional behaviour of calcite at  
1134 room temperature: insights from laboratory experiments and microstruc-  
1135 tural observations. *Geophysical Journal International*, *205*, 548-561.  
1136 (<https://doi.org/10.1093/gji/ggw038>)
- 1137 Carpenter, B., Ikari, M., & Marone, C. (2016). Laboratory observations of time-  
1138 dependent frictional strengthening and stress relaxation in natural and syn-  
1139 thetic fault gouges. *Journal of Geophysical Research: Solid Earth*, *121*, 1183-  
1140 1201. (<https://doi.org/10.1002/2015JB012136>)
- 1141 Carpenter, B., Marone, C., & Saffer, D. (2011). Weakness of the San Andreas Fault  
1142 revealed by samples from the active fault zone. *Nature Geoscience*, *4*, 251-254.  
1143 (<https://doi.org/10.1038/NCEO1089>)
- 1144 Cathelineau, M., & Izquierdo, G. (1988). Temperature - composition rela-  
1145 tionships of authigenic micaceous minerals in the Los Azufres geother-  
1146 mal system. *Contributions to Mineralogy and Petrology*, *100*, 418-428.  
1147 (<https://doi.org/10.1007/BF00371372>)

- 1148 Chen, J., Verberne, B., & Spiers, C. (2015). Effects of healing on the seismogenic  
1149 potential of carbonate fault rocks: Experiments on samples from the Longmen-  
1150 shan Fault, Sichuan, China. *Journal of Geophysical Research: Solid Earth*,  
1151 *120*, 5479-5506. (<https://doi.org/10.1002/2015JB012051>)
- 1152 Church, B., Jessop, A., Bell, R., & Pettipas, A. (1990). Tertiary outlier studies:  
1153 Recent investigations in the Summerland Basin, South Okanagan Area, B.C.  
1154 (82E/12). *Geological Fieldwork*, 163-170.
- 1155 Cladouhos, T., Petty, S., Nordin, Y., Moore, M., Grasso, K., Uddenberg, M., &  
1156 Swyer, M. (2013). Stimulation results from the Newberry Volcano EGS  
1157 Demonstration. *Geothermal Research Council Transactions*, *37*, 133-140.
- 1158 Cladouhos, T., Petty, S., Swyer, M., Uddenberg, M., Grasso, K.,  
1159 & Nordin, Y. (2016). Results from Newberry Volcano  
1160 EGS Demonstration, 2010-2014. *Geothermics*, *63*, 44-61.  
1161 (<https://dx.doi.org/10.1016/j.geothermics.2015.08.009>)
- 1162 Collettini, C., Tesei, T., Scuderi, M., Carpenter, B., & Viti, C. (2019). Beyond Byer-  
1163 lee friction, weak faults and implications for slip behavior. *Earth and Planetary  
1164 Science Letters*, *519*, 245-263. (<https://doi.org/10.1016/j.epsl.2019.05.011>)
- 1165 Correia, H., Sigurdsson, O., Sanjuan, B., Tulinius, H., & Lasne, E. (2000). Stimu-  
1166 lation of a high-enthalpy geothermal well by cold water injection. *Geothermal  
1167 Resources Council Transactions*, *24*, 129-136.
- 1168 Curewitz, D., & Karson, J. (1997). Structural settings of hydrothermal out-  
1169 flow: Fracture permeability maintained by fault propagation and inter-  
1170 action. *Journal of Volcanology and Geothermal Research*, *79*, 149-168.  
1171 ([https://doi.org/10.1016/S0377-0273\(97\)00027-9](https://doi.org/10.1016/S0377-0273(97)00027-9))
- 1172 DeMets, C., Gordon, R., & Argus, D. (2010). Geologically current plate motions.  
1173 *Geophysical Journal International*, *181*, 1-80. (<https://doi.org/10.1111/j.1365-246X.2009.04491.x>)
- 1174
- 1175 Deng, J., & Sykes, L. (1995). Determination of Euler pole for contemporary relative  
1176 motion of Caribbean and North American plates using slip vectors of inter-  
1177 plate earthquakes. *Tectonics*, *14*, 39-53. (<https://doi.org/10.1029/94TC02547>)
- 1178 Dieterich, J. (1972). Time-dependent friction in rocks. *Journal of Geophysical Re-  
1179 search*, *77*, 3690-3697. (<https://doi.org/10.1007/BF00876539>)
- 1180 Dieterich, J. (1979). Modeling of rock friction 1. Experimental results and  
1181 constitutive equations. *Journal of Geophysical Research*, *84*, 2161-2168.  
1182 (<https://doi.org/10.1029/JB084iB05p02161>)
- 1183 Doebelin, N., & Kleeberg, R. (2015). *Profex*: a graphical user interface for the  
1184 Rietveld refinement program *BGMN*. *Journal of Applied Crystallography*, *48*,  
1185 1573-1580. (<http://dx.doi.org/10.1107/S1600576715014685>)
- 1186 Dorbath, L., Cuenot, N., Genter, A., & Frogneux, M. (2009). Seismic response of  
1187 the fractured and faulted granite of Soultz-sous-Forêts (France) to 5 km deep  
1188 massive water injections. *Geophysical Journal International*, *177*, 653-675.  
1189 (<https://doi.org/10.1111/j.1365-246X.2009.04030.x>)
- 1190 Evans, K., Zappone, A., Kraft, T., Deichmann, N., & Moia, F. (2012). A  
1191 survey of the induced seismic responses to fluid injection in geother-  
1192 mal and CO<sub>2</sub> reservoirs in Europe. *Geothermics*, *41*, 30-54.  
1193 (<https://doi.org/10.1016/j.geothermics.2011.08.002>)
- 1194 Fang, Y., den Hartog, S., Elsworth, D., Marone, C., & Cladouhos, T. (2016).  
1195 Anomalous distribution of microearthquakes in the Newberry Geother-  
1196 mal Reservoir: Mechanisms and implications. *Geothermics*, *63*, 62-73.  
1197 (<https://dx.doi.org/10.1016/j.geothermics.2015.04.005>)
- 1198 Favier, A., Lardeaux, J., Corsini, M., Verati, C., Navelot, V., Géraud, Y., ...  
1199 Voitus, E. (2021). Characterization of an exhumed high-temperature hydro-  
1200 thermal system and its application for deep geothermal exploration: An  
1201 example from Terre-de-Haut Island (Guadeloupe archipelago, Lesser An-  
1202 tilles volcanic arc). *Journal of Volcanology and Geothermal Research*, *418*.



- (<https://doi.org/10.1016/j.jvolgeores.2021.107256>)
- 1203 Favier, A., Lardeaux, J., Legendre, L., Verati, C., Philippon, M., Corsini, M., . . .  
 1204 Ventalon, S. (2019). Tectono-metamorphic evolution of shallow crustal lev-  
 1205 els within active volcanic arcs. Insights from the exhumed Basal Complex of  
 1206 Basse-Terre (Guadeloupe, French West Indies). *Earth Sciences Bulletin*, *190*.  
 1207 (<https://doi.org/10.1051/bsgf/2019011>)
- 1208 Favier, A., Lardeaux, J., Verati, C., Corsini, M., Münch, P., & Ventalon, S. (2021).  
 1209 The concept of exhumed analogue for characterization of high-energy geother-  
 1210 mal reservoir: An example from Les Saintes Island (Guadeloupe Archipelago,  
 1211 Lesser Antilles) and consequences for exploration. In *Proceedings World*  
 1212 *Geothermal Congress 2020+1*.
- 1213 Fenner, C. (1934). Hydrothermal metamorphism in geyser-basins of Yellowstone  
 1214 Park, as shown by deep drilling. *Eos, Transactions American Geophysical*  
 1215 *Union*, *15*, 240-243. (<https://doi.org/10.1029/TR015i001p00240-2>)
- 1216 Fetterman, J., & Davatzes, N. (2011). Evolution of porosity in fractures in the  
 1217 Newberry Volcano Geothermal System, Oregon, USA: Feedback between de-  
 1218 formation and alteration. *Geothermal Research Council Transactions*, *35*,  
 1219 339-346.
- 1220 Frolova, J., Ladygin, V., & Rychagov, S. (2006). Petrophysical indicators of argilliza-  
 1221 tion zone in geothermal fields. *Geothermal Resource Council Transactions*, *30*,  
 1222 909-912.
- 1223 Frolova, J., Ladygin, V., & Rychagov, S. (2010). Petrophysical alteration of volcanic  
 1224 rocks in hydrothermal systems of the Kuril-Kamchatka Island Arc. In *Proceed-*  
 1225 *ings World Geothermal Congress 2010*.
- 1226 Frolova, J., Ladygin, V., Rychagov, S., & Zukhubaya, D. (2014). Effects of  
 1227 hydrothermal alterations on physical and mechanical properties of rocks  
 1228 in the Kuril-Kamchatka island arc. *Engineering Geology*, *183*, 80-95.  
 1229 (<https://dx.doi.org/10.1016/j.enggeo.2014.10.011>)
- 1230 Fryer, B., Jermann, F., Patrier, P., Lanson, B., Jelavic, S., Meyer, G., . . . Violay, M.  
 1231 (2024a). *Data Set for "Alteration's control on frictional behavior and the depth*  
 1232 *of the ductile shear zone in geothermal reservoirs in volcanic arcs" I: Cascade*  
 1233 *Volcanic Arc* [dataset]. Zenodo. doi: 10.5281/zenodo.10964935
- 1234 Fryer, B., Jermann, F., Patrier, P., Lanson, B., Jelavic, S., Meyer, G., & Violay, M.  
 1235 (2024b). *Data Set for "Alteration's control on frictional behavior and the depth*  
 1236 *of the ductile shear zone in geothermal reservoirs in volcanic arcs" I: Lesser*  
 1237 *Antilles Volcanic Arc* [dataset]. Zenodo. doi: 10.5281/zenodo.10912444
- 1238 Gadalia, A., Baltassat, J., Bouchot, V., Caritg, S., Coppo, N., Gal, F., . . . Zam-  
 1239 mit, C. (2014). *Compléments d'exploration géothermique en Martinique:*  
 1240 *Conclusions et recommandations pour les zones de la Montagne Pelée, des*  
 1241 *Anses-d'Arlet, des Pitons du Carbet et du Lamentin*.
- 1242 Gadalia, A., Bouchot, V., Calcagno, P., Caritg, S., Courrioux, G., Darnet, M., . . .  
 1243 Vittecoq, B. (2019). Multimodal geothermal exploration in the Lesser Antilles  
 1244 Arc at the Lamentin lowland (Martinique). In *Iop conf. series: Earth and*  
 1245 *environmental science*.
- 1246 Genter, A., Traineau, H., Degouy, M., Correia, H., Mas, A., Patrier, P., . . . Sanjuan,  
 1247 B. (2002). Preliminary geological results of recent exploratory drillings in a  
 1248 geothermal fractured reservoir at Lamentin (French West Indies, Martinique). In  
 1249 *Proceedings: Twenty-Seventh Workshop on Geothermal Reservoir Engineering*  
 1250 *Stanford University, Stanford, California, January 28-30, 2002*.
- 1251 Ghomshei, M., Sanyal, S., MacLeod, K., Henneberger, R., Ryder, A., Meech, J., &  
 1252 Fainbank, B. (2004). Status of the South Meager Geothermal Project British  
 1253 Columbia, Canada: Resource evaluation and plans for development. *Geother-*  
 1254 *mal Resources Council Transactions*, *28*, 339-344.
- 1255 Giacomel, P., Ruggieri, R., Scuderi, M., Spagnuolo, E., Di Toro, G., & Colletini,  
 1256 C. (2021). Frictional properties of basalt experimental faults and implica-  
 1257

- 1258 tions for volcano-tectonic settings and geo-energy sites. *Tectonophysics*, 881.  
 1259 (<https://doi.org/10.1016/j.tecto.2021.228883>)
- 1260 Giorgetti, C., Carpenter, B., & Collettini, C. (2015). Frictional behavior of talc-  
 1261 calcite mixtures. *Journal of Geophysical Research: Solid Earth*, 120, 6614-  
 1262 6633. (<https://dx.doi.org/10.1002/2015JB011970>)
- 1263 Global Volcanism Program. (2024). *Volcanoes of the World (v. 5.2.1; 3 Jul 2024)*.  
 1264 (Smithsonian Institution, compiled by Venzke, [https://doi.org/10.5479/  
 1265 si.GVP.VOTW5-2024.5.2](https://doi.org/10.5479/si.GVP.VOTW5-2024.5.2))
- 1266 Goko, K. (2000). Structure and hydrology of the Ogiri field, West  
 1267 Kirishima geothermal area, Kyushu, Japan. *Geothermics*, 29, 127-149.  
 1268 ([https://doi.org/10.1016/S0375-6505\(99\)00055-3](https://doi.org/10.1016/S0375-6505(99)00055-3))
- 1269 Grasby, S., Ansari, S., Bryant, R., Calahorrano-DiPatre, A., Chen, Z., Craven, J.,  
 1270 J. and Dettmer, ... Williamson, A. (2020). *Garibaldi Geothermal Energy  
 1271 Project - Mount Meager 2019 Field Program* (No. 2020-09).
- 1272 Grasby, S., Calahorrano-Di Patre, A., Chen, Z., Dettmer, J., Gilbert, H., Hanneson,  
 1273 C., ... Yuan, W. (2022). Geothermal resource potential of the Garibaldi Vol-  
 1274 canic Belt, Southwestern British Columbia (Part of NTS 092J): Phase 2. In  
 1275 *Geoscience BC Summary of Activities 2021: Energy and Water, Geoscience  
 1276 BC, Report 2022-02* (p. 75-80). Geoscience BC.
- 1277 Griggs, D. (1936). Deformation of rocks under high confining pressures: I. Ex-  
 1278 periments at room temperature. *The Journal of Geology*, 44, 541-577.  
 1279 (<https://doi.org/10.1086/624455>)
- 1280 Häring, M., Schanz, U., Ladner, F., & Dyer, B. (2008). Characterisation of  
 1281 the Basel 1 enhanced geothermal system. *Geothermics*, 37, 469-495.  
 1282 (<https://doi.org/10.1016/j.geothermics.2008.06.002>)
- 1283 Harrison, E., Kieschnick, W., & McGuire, W. (1954). The mechanics of fracture in-  
 1284 duction and extension. *Petroleum Transactions*, 201, 252-263.
- 1285 Heap, M., Troll, V., Kushnir, A., Gilg, A., Collinson, A., Deegan, F., ... Wal-  
 1286 ter, T. (2019). Hydrothermal alteration of andesitic lava domes can  
 1287 lead to explosive volcanic behaviour. *Nature Communications*, 10.  
 1288 (<https://doi.org/10.1038/s41467-019-13102-8>)
- 1289 Hormozzade Ghalati, F., Craven, J., Motazedian, D., Grasby, S., Roots, E.,  
 1290 Tschirhart, V., ... Liu, X. (2023). Analysis of fluid flow pathways in  
 1291 the Mount Meager Volcanic Complex, Southwestern Canada, utilizing  
 1292 AMT and petrophysical data. *Geochemistry, Geophysics, Geosystems*, 24.  
 1293 (<https://doi.org/10.1029/2022GC010814>)
- 1294 Ikari, M., Carpenter, B., & Marone, C. (2016). A microphysical interpretation of  
 1295 rate- and state-dependent friction for fault gouge. *Geochemistry, Geophysics,  
 1296 Geosystems*, 17, 1660-1677. (<https://doi.org/10.1002/2016GC006286>)
- 1297 Ikari, M., Marone, C., & Saffer, D. (2011). On the relation be-  
 1298 tween fault strength and frictional stability. *Geology*, 39, 83-86.  
 1299 (<https://doi.org/10.1130/G31416.1>)
- 1300 Ikari, M., Saffer, D., & Marone, C. (2007). Effect of hydration state on the fric-  
 1301 tional properties of montmorillonite-based fault gouge. *Journal of Geophysical  
 1302 Research*, 112. (<https://doi.org/10.1029/2006JB004748>)
- 1303 Ikari, M., Saffer, D., & Marone, C. (2009). Frictional and hydrologic  
 1304 properties of clay-rich fault gouge. *Journal of Geophysical Research*.  
 1305 (<https://doi.org/10.1029/2008JB006089>)
- 1306 Imber, J., Holdsworth, R., Butler, C., & Strachan, R. (2001). A reap-  
 1307 praisal of the Sibson-Scholz fault zone model: The nature of the  
 1308 frictional to viscous ("brittle-ductile") transition along a long-lived  
 1309 crustal-scale fault, Outer Hebrides, Scotland. *Tectonics*, 20, 601-624.  
 1310 (<https://doi.org/10.1029/2000TC001250>)
- 1311 IRD. (2014). *Les ressources en eau de surface de la Martinique. A set of 9 map  
 1312 sheets. Scale of 1:100000. Date of publication: 1974-1975. Project NumeriSud*

- 1313 *SPHAERA-GEO*. Bondy, France.
- 1314 Jacques, D., & Maury, R. (1988). L'archipel des Saintes (Guadeloupe, Petites An-
- 1315 tilles): Géologie et pétrologie. *Géologie de la France*, *2*, 89-99.
- 1316 Jaud, P., & Lamethe, D. (1985). Les installations géothermiques de Bouillante. *La*
- 1317 *Houille Blanche*, *71*, 347-352. (<https://doi.org/10.1051/lhb/1985025>)
- 1318 Jeppson, T., Lockner, D., Beeler, N., & Moore, D. (2023). Time-dependent weak-
- 1319 ening of granite at hydrothermal conditions. *Geophysical Research Letters*, *50*.
- 1320 (<https://doi.org/10.1029/2023GL105517>)
- 1321 Jessop, A. (2008). *Review of the National Geothermal Energy Program Phase 2 -*
- 1322 *Geothermal potential of the Cordillera* (No. 5906).
- 1323 Jolie, E., Scott, S., Faulds, J., Chambefort, I., Axelsson, G., Gutiérrez-Negrín, L.,
- 1324 ... Zemedkun, M. (2021). Geological controls on geothermal resources
- 1325 for power generation. *Nature Reviews Earth & Environment*, *2*, 324-339.
- 1326 (<https://doi.org/10.1038/s43017-021-00154-y>)
- 1327 Keefer, D. (1984). Rock avalanches caused by earthquakes: Source characteristics.
- 1328 *Science*, *223*, 1288-1290. (<https://doi.org/10.1126/science.223.4642.1288>)
- 1329 Kim, K., Ree, J., Kim, Y., Kim, S., Kang, S., & Seo, W. (2018). Assessing whether
- 1330 the 2017  $M_w$  5.4 Pohang earthquake in South Korea was an induced event.
- 1331 *Science*, *360*, 1007-1009. (<https://doi.org/10.1126/science.aat6081>)
- 1332 Knipe, R., & McCaig, A. (1994). Microstructural and microchemical consequences of
- 1333 fluid flow in deforming rocks. In J. Parnell (Ed.), *Geofluids: Origin, migration*
- 1334 *and evolution of fluids in sedimentary basins* (p. 99-111). Geological Society.
- 1335 Kohlstedt, D., Evans, B., & Mackwell, S. (1995). Strength of the lithosphere: Con-
- 1336 straints imposed by laboratory experiments. *Journal of Geophysical Research*,
- 1337 *100*, 17587-17602. (<https://doi.org/10.1029/95JB01460>)
- 1338 Kolawole, F., Johnston, C., Morgan, C., Chang, J., Marfurt, K., Lockner, D., ...
- 1339 Carpenter, B. (2019). The susceptibility of Oklahoma's basement to seismic
- 1340 reactivation. *Nature Geoscience*, *12*, 839-844. ([https://doi.org/10.1038/s41561-](https://doi.org/10.1038/s41561-019-0440-5)
- 1341 [019-0440-5](https://doi.org/10.1038/s41561-019-0440-5))
- 1342 Koroknai, B., Árkai, P., Horváth, P., & Balogh, K. (2008). Anatomy of a tran-
- 1343 sitional brittle-ductile shear zone developed in a low-T meta-andesite tuff:
- 1344 A microstructural, petrological and geochronological case study from the
- 1345 Bükk Mts. (NE Hungary). *Journal of Structural Geology*, *30*, 159-176.
- 1346 (<https://doi.org/10.1016/j.jsg.2007.10.007>)
- 1347 Kry, P., & Gronseth, J. (1983). In-situ stresses and hydraulic fractur-
- 1348 ing in the Deep Basin. *Journal of Canadian Petroleum Technology*,
- 1349 <https://doi.org/10.2118/83-06-02>.
- 1350 Kutz, M. (2009). *Eshbach's Handbook of Engineering Fundamentals*. John Wiley &
- 1351 Sons, Inc.
- 1352 Li, Y., Wang, J., Jung, W., & Ghassemi, A. (2012). Mechanical properties of in-
- 1353 tact rock and fractures in welded tuff from Newberry Volcano. In *Proceedings,*
- 1354 *Thirty-Seventh Workshop on Geothermal Reservoir Engineering, Stanford*
- 1355 *University, Stanford, California, January 30 - February 1, 2012*.
- 1356 Logan, J., Dengo, C., Higgs, N., & Wang, Z. (1992). Fabrics of experimental fault
- 1357 zones: their development and relationship to mechanical behavior. *Interna-*
- 1358 *tional Geophysics*, *51*, 33-67. ([https://doi.org/10.1016/S0074-6142\(08\)62814-](https://doi.org/10.1016/S0074-6142(08)62814-4)
- 1359 [4](https://doi.org/10.1016/S0074-6142(08)62814-4))
- 1360 Logan, J., & Rauenzahn, K. (1987). Frictional dependence of gouge mixtures of
- 1361 quartz and montmorillonite on velocity, composition and fabric. *Tectono-*
- 1362 *physics*, *144*, 87-108. ([https://doi.org/10.1016/0040-1951\(87\)90010-2](https://doi.org/10.1016/0040-1951(87)90010-2))
- 1363 Lucchitta, I. (1990). Role of heat and detachment in continental extension as viewed
- 1364 from the eastern Basin and Range Province in Arizona. *Tectonophysics*, *174*,
- 1365 77-114. ([https://doi.org/10.1016/0040-1951\(90\)90385-L](https://doi.org/10.1016/0040-1951(90)90385-L))
- 1366 Lucier, A., Zoback, M., Gupta, N., & Ramakrishnan, T. (2006). Geome-
- 1367 chanical aspects of CO<sub>2</sub> sequestration in a deep saline reservoir in the

- 1368 Ohio River Valley region. *Environmental Geosciences*, *13*, 85-103.  
 1369 (<https://doi.org/10.1306/eg.11230505010>)
- 1370 Lupini, J., Skinner, A., & Vaughan, P. (1981). The drained resid-  
 1371 ual strength of cohesive soils. *Géotechnique*, *31*, 181-213.  
 1372 (<https://doi.org/10.1680/geot.1981.31.2.181>)
- 1373 MacLeod, N., & Sammel, E. (1982). Newberry Volcano, Oregon: A Cascade Range  
 1374 geothermal prospect. *Oregon Geology*, *44*, 123-131.
- 1375 MacLeod, N., & Sherrod, D. (1988). Geologic evidence for a magma chamber be-  
 1376 neath Newberry Volcano, Oregon. *Journal of Geophysical Research*, *93*, 10067-  
 1377 10079. (<https://doi.org/10.1029/JB093iB09p10067>)
- 1378 MacLeod, N., Sherrod, D., Chitwood, L., & Jensen, R. (1995). *Geologic map of New-*  
 1379 *berry Volcano, Deschutes, Klamath, and Lake Counties, Oregon.*
- 1380 Manga, M., Hornbach, M., Le Friant, A., Ishizuka, O., Stroncik, N., Adachi, T.,  
 1381 ... Wang, F. (2012). Heat flow in the Lesser Antilles Island Arc and ad-  
 1382 jacent back arc Grenada Basin. *Geochemistry Geophysics Geosystems*, *13*.  
 1383 (<https://doi.org/10.1029/2012GC004260>)
- 1384 Marone, C. (1998). Laboratory-derived friction laws and their application to seis-  
 1385 mic faulting. *Annual Review of Earth and Planetary Sciences*, *26*, 643-696.  
 1386 (<https://doi.org/10.1146/annurev.earth.26.1.643>)
- 1387 Marone, C., & Kilgore, B. (1993). Scaling of the critical slip distance for  
 1388 seismic faulting with shear strain in fault zones. *Nature*, *362*, 618-621.  
 1389 (<https://doi.org/10.1038/362618a0>)
- 1390 Marone, C., Raleigh, C., & Scholz, C. (1990). Frictional behavior and constitutive  
 1391 modeling of simulated fault gouge. *Journal of Geophysical Research*, *95*, 7007-  
 1392 7025. (<https://doi.org/10.1029/JB095iB05p07007>)
- 1393 Mas, A., Guisseau, D., Patrier, P., Beaufort, D., Genter, A., Sanjuan, B., & Girard,  
 1394 J. (2006). Clay minerals related to the hydrothermal activity of the Bouil-  
 1395 lante geothermal field (Guadeloupe). *Journal of Volcanology and Geothermal*  
 1396 *Research*, *158*, 380-400. (<https://doi.org/10.1016/j.jvolgeores.2006.07.010>)
- 1397 Mas, A., Patrier, P., Beaufort, D., & Genter, A. (2003). Clay-mineral signatures  
 1398 of fossil and active hydrothermal circulations in the geothermal system of  
 1399 Lamentin Plain, Martinique. *Journal of Volcanology and Geothermal Research*,  
 1400 *124*, 195-218. ([https://doi.org/10.1016/S0377-0273\(03\)00044-1](https://doi.org/10.1016/S0377-0273(03)00044-1))
- 1401 Maza, S., Collo, G., Morata, D., Lizana, C., Camus, E., Taussi, M., ... Rivera, G.  
 1402 (2018). Clay mineral associations in the clay cap from the Cerro Pabellón  
 1403 blind geothermal system, Andean Cordillera, Northern Chile. *Clay Minerals*,  
 1404 *53*, 117-141. (<https://doi.org/10.1180/clm.2018.9>)
- 1405 Meller, C., & Kohl, T. (2014). The significance of hydrothermal alteration zones  
 1406 for the mechanical behavior of a geothermal reservoir. *Geothermal Energy*, *2*.  
 1407 (<https://doi.org/10.1186/s40517-014-0012-2>)
- 1408 Melosh, G., Cumming, W., Benoit, D., Wilmarth, M., Colvin, A., Winick, J., ...  
 1409 Peretz, A. (2010). Exploration results and resource conceptual model of the  
 1410 Tolhuaca Geothermal Field, Chile. In *Proceedings world geothermal congress*  
 1411 *2010*.
- 1412 Meng, M., Frash, L., Li, W., Welch, N., Carey, J., Morris, J., ... Kneafsey, T.  
 1413 (2022). Hydro-mechanical measurements of sheared crystalline rock fractures  
 1414 with applications for EGS Collab Experiments 1 and 2. *Journal of Geophysical*  
 1415 *Research: Solid Earth*, *127*. (<https://doi.org/10.1029/2021JB023000>)
- 1416 Meyer, G., Brantut, N., Mitchell, T., & Meredith, P. (2019). Fault reactivation and  
 1417 strain partitioning across the brittle-ductile transition. *Geology*, *47*, 1127-1130.  
 1418 (<https://doi.org/10.1130/G46516.1>)
- 1419 Meyer, G., & Violay, V. (2023). Bounding the localized to ductile transition in  
 1420 porous rocks: implications for geo-reservoirs. *Geophysical Journal Interna-*  
 1421 *tional*, *235*, 2361-2371. (<https://doi.org/10.1093/gji/ggad377>)
- 1422 Michel, F., Allen, D., & Grant, M. (2002). Hydrogeochemistry and geothermal char-

- acteristics of the White Lake basin, South-central British Columbia, Canada. *Geothermics*, *31*, 169-194. ([https://doi.org/10.1016/S0375-6505\(01\)00009-8](https://doi.org/10.1016/S0375-6505(01)00009-8))
- Monger, J., & Irving, E. (1980). Northward displacement of north-central British Columbia. *Nature*, *285*, 289-294. (<https://doi.org/10.1038/285289a0>)
- Montgomery, D., & Runger, G. (2011). *Applied Statistics and Probability for Engineers* (Fifth ed.). John Wiley & Sons, Inc.
- Moore, D., & Lockner, D. (2004). Crystallographic controls on the frictional behavior of dry and water-saturated sheet structure minerals. *Journal of Geophysical Research*, *109*. (<https://doi.org/10.1029/2003JB002582>)
- Moore, D., & Lockner, D. (2007). Friction of the smectite clay montmorillonite. In T. Dixon & C. Moore (Eds.), *The seismogenic zone of subduction thrust faults* (p. 317-345). New York Chichester, West Sussex: Columbia University Press.
- Moore, D., Lockner, D., Shengli, M., Summers, R., & Byerlee, J. (1997). Strengths of serpentinite gouges at elevated temperatures. *Journal of Geophysical Research*, *102*, 14787-14801. (<https://doi.org/10.1029/97JB00995>)
- Morrow, C., Moore, D., & Lockner, D. (2000). The effect of mineral bond strength and absorbed water on fault gouge frictional strength. *Geophysical Research Letters*, *27*, 815-818. (<https://doi.org/10.1029/1999GL008401>)
- Morrow, C., Radney, B., & Byerlee, J. (1992). Frictional strength and the effective pressure law of Montmorillonite and Illite clays. *International Geophysics*, *51*, 69-88. ([https://doi.org/10.1016/S0074-6142\(08\)62815-6](https://doi.org/10.1016/S0074-6142(08)62815-6))
- Navelot, V., Géraud, Y., Favier, A., Diraison, M., Corsini, M., Lardeaux, J., ... Beauchamps, G. (2018). Petrophysical properties of volcanic rocks and impacts of hydrothermal alteration in the Guadeloupe Archipelago (West Indies). *Journal of Volcanology and Geothermal Research*, *360*, 1-21. (<https://doi.org/10.1016/j.jvolgeores.2018.07.004>)
- Niemeijer, A., & Spiers, C. (2006). Velocity dependence of strength and healing behaviour in simulated phyllosilicate-bearing fault gouge. *Tectonophysics*, *427*, 231-253. (<https://doi.org/10.1016/j.tecto.2006.03.048>)
- NOAA National Centers for Environmental Information. (2022). *ETOPO 2022 15 Arc-Second Global Relief Model*. (<https://doi.org/10.25921/fd45-gt74>)
- Noël, C., Baud, P., & Violay, M. (2021). Effect of water on sandstone's fracture toughness and frictional parameters: Brittle strength constraints. *International Journal of Rock Mechanics and Mining Sciences*, *147*. (<https://doi.org/10.1016/j.ijrmms.2021.104916>)
- Noël, C., Fryer, B., Baud, P., & Violay, V. (2024). Water weakening and the compressive brittle strength of carbonates: Influence of fracture toughness and static friction. *International Journal of Rock Mechanics and Mining Sciences*, *177*. (<https://doi.org/10.1016/j.ijrmms.2024.105736>)
- Noël, C., Giorgetti, C., Collettini, C., & Marone, C. (2024). The effect of shear strain and shear localization on fault healing. *Geophysical Journal International*, *236*, 1206-1215. (<https://doi.org/10.1093/gji/ggad486>)
- Noël, C., Giorgetti, C., Scuderi, M., Collettini, C., & Marone, C. (2023). The effect of shear displacement and wear on fault stability: Laboratory constraints. *Journal of Geophysical Research: Solid Earth*, *128*. (<https://doi.org/10.1029/2022JB026191>)
- Obermann, A., Kraft, T., Larose, E., & Weimer, S. (2015). Potential of ambient seismic noise techniques to monitor the St. Gallen geothermal site (Switzerland). *Journal of Geophysical Research: Solid Earth*, *120*, 4301-4316. (<https://doi.org/10.1002/2014JB011817>)
- Orellana, L., Scuderi, M., Collettini, C., & Violay, M. (2018). Frictional properties of Opalinus Clay: Implications for nuclear waste storage. *Journal of Geophysical Research: Solid Earth*. (<https://doi.org/10.1002/2017JB014931>)
- Paterson, M. (1958). Experimental deformation and faulting in Wombeyan marble. *Geological Society of America Bulletin*, *69*, 465-476.

- ([https://doi.org/10.1130/0016-7606\(1958\)69\[465:EDAFIW\]2.0.CO;2](https://doi.org/10.1130/0016-7606(1958)69[465:EDAFIW]2.0.CO;2))
- 1478 Paterson, M., & Wong, T. (2005). *Experimental Rock Deformation - The Brittle*  
1479 *Field*. Springer-Verlag.
- 1480
- 1481 Patrier, P., Beaufort, D., Bril, H., Bonhomme, M., Fouillac, A., & Aumàitre, R.  
1482 (1997). Alteration-mineralization at the Bernardan U Deposit (Western  
1483 Marche, France): The contribution of alteration petrology and crystal chem-  
1484 istry of secondary phases to a new genetic model. *Economic Geology*, *92*,  
1485 448-467. (<https://doi.org/10.2113/gsecongeo.92.4.448>)
- 1486 Phillips, N., Belzer, B., French, M., Rowe, C., & Ujiie, K. (2020). Fric-  
1487 tional strengths of subduction thrust rocks in the region of shallow  
1488 slow earthquakes. *Journal of Geophysical Research: Solid Earth*, *125*.  
1489 (<https://doi.org/10.1029/2019JB018888>)
- 1490 Pozzi, G., Collettini, C., Scuderi, M., Tesei, T., Marone, C., Amodio, A., & Cocco,  
1491 M. (2023). Fabric controls fault stability in serpentinite gouges. *Geophysical*  
1492 *Journal International*, *235*, 1778-1797. (<https://doi.org/10.1093/gji/ggad322>)
- 1493 Pozzi, G., Scuderi, M., Tinti, E., Nazzari, M., & Collettini, C. (2022). The role of  
1494 fault rock fabric in the dynamics of laboratory faults. *Journal of Geophysical*  
1495 *Research: Solid Earth*, *127*. (<https://doi.org/10.1029/2021JB023779>)
- 1496 Pramono, B., & Colombo, D. (2005). Microearthquake characteristics in Darajat  
1497 Geothermal Field, Indonesia. In *Proceedings World Geothermal Congress 2005*.  
1498 Antalya, Turkey.
- 1499 Ranalli, G., & Rybach, L. (2005). Heat flow, heat transfer and  
1500 lithosphere rheology in geothermal area: Features and exam-  
1501 ples. *Journal of Volcanology and Geothermal Research*, *148*, 3-19.  
1502 (<https://doi.org/10.1016/j.jvolgeores.2005.04.010>)
- 1503 Read, P. (1979). *Geology, Meager Creek Geothermal area, British Columbia; Geolog-*  
1504 *ical Survey of Canada, Open File 603, 1 .zip file. doi:10.4095/129507.*
- 1505 Rejeki, S., Rohrs, D., Nordquist, G., & Fitriyanto, A. (2010). Geologic concep-  
1506 tual model update of the Darajat Geothermal Field, Indonesia. In *Proceedings*  
1507 *World Geothermal Congress 2010*. Bali, Indonesia.
- 1508 Revil, A., & Gresse, M. (2021). Induced polarizatin as a tool to as-  
1509 sess alteration in geothermal systems: A review. *Minerals*, *11*.  
1510 (<https://doi.org/10.3390/min11090962>)
- 1511 Rice, J., & Ruina, A. (1983). Stability of steady frictional slipping. *Journal of Ap-*  
1512 *plied Mechanics*, *50*, 343-349. (<https://doi.org/10.1115/1.3167042>)
- 1513 Richards, J. (2011). Magmatic to hydrothermal metal fluxes in con-  
1514 vergent and collided margins. *Ore Geology Reviews*, *40*, 1-26.  
1515 (<https://doi.org/10.1016/j.oregeorev.2011.05.006>)
- 1516 Ruina, A. (1983). Slip instability and state variable friction  
1517 laws. *Journal of Geophysical Research*, *88*, 10359-10370.  
1518 (<https://doi.org/10.1029/JB088iB12p10359>)
- 1519 Rutter, E. (1986). On the nomenclature of mode of failure transitions in rocks.  
1520 *Tectonophysics*, *122*, 381-387. ([https://doi.org/10.1016/0040-1951\(86\)90153-8](https://doi.org/10.1016/0040-1951(86)90153-8))
- 1521 Saffer, D., Lockner, D., & McKiernan, A. (2012). Effects of smectite  
1522 to illite transformation on the frictional strength and sliding stabil-  
1523 ity of intact marine mudstones. *Geophysical Research Letters*, *39*.  
1524 (<https://doi.org/10.1029/2012GL051761>)
- 1525 Saffer, D., & Marone, C. (2003). Comparison of smectite- and illite-rich gouge fric-  
1526 tional properties: application to the updip limit of the seismogenic zone along  
1527 subduction megathrusts. *Earth and Planetary Science Letters*, *215*, 219-235.  
1528 ([https://doi.org/10.1016/S0012-821X\(03\)00424-2](https://doi.org/10.1016/S0012-821X(03)00424-2))
- 1529 Sanchez-Alfaro, P., Reich, M., Arancibia, G., Pérez-Flores, P., Cembrano, J.,  
1530 Driesner, T., . . . Campos, E. (2016). Physical, chemical and mineralog-  
1531 ical evolution of the Tolhuaca geothermal system, southern Andes, Chile:  
1532 Insights into the interplay between hydrothermal alteration and brittle de-

- 1533 formation. *Journal of Volcanology and Geothermal Research*, *324*, 88-104.  
 1534 (<https://dx.doi.org/10.1016/j.jvolgeores.2016.05.009>)
- 1535 Sanjuan, B., Genter, A., Correia, H., Girard, J., Roig, J., & Brach, M. (2002).  
 1536 *Travaux scientifiques associés à la réalisation des trois puits d'exploration*  
 1537 *géothermique dans la plaine du Lamentin (Martinique)* (No. BRGM/RP-51671-  
 1538 FR).
- 1539 Sanjuan, B., Traineau, H., Genter, A., Correia, H., Brach, M., & Degouy, M. (2002).  
 1540 Geochemical investigations during a new geothermal exploration phase in the  
 1541 Lamentin Plain (French West Indies, Martinique). In *Proceedings: Twenty-*  
 1542 *Seventh Workshop on Geothermal Reservoir Engineering Stanford University,*  
 1543 *Stanford, California, January 28-30, 2002.*
- 1544 Scholz, C. (2019). *The mechanics of earthquakes and faulting*. Cambridge University  
 1545 Press. Retrieved from <https://doi.org/10.1017/9781316681473>
- 1546 Scott, D., Marone, C., & Sammis, C. (1994). The apparent friction of granular  
 1547 fault gouge in sheared layers. *Journal of Geophysical Research*, *99*, 7231-7246.  
 1548 (<https://doi.org/10.1029/93JB03361>)
- 1549 Segall, P., & Rice, J. (1995). Dilatancy, compaction, and slip instability of a  
 1550 fluid-infiltrated fault. *Journal of Geophysical Research*, *100*, 22155-22171.  
 1551 (<https://doi.org/10.1029/95JB02403>)
- 1552 Shea, W., & Kronenberg, A. (1992). Rheology and deformation mechanisms of  
 1553 an isotropic mica schist. *Journal of Geophysical Research*, *97*, 15201-15237.  
 1554 (<https://doi.org/10.1029/92JB00620>)
- 1555 Shreedhara, S., Ikari, M., Wood, C., Saffer, D., Wallace, L., & Marone, C.  
 1556 (2022). Frictional and lithological controls on shallow slip at the North-  
 1557 ern Hikurangi Margin. *Geochemistry, Geophysics, Geosystems*, *23*.  
 1558 (<https://doi.org/10.1029/2021GC010107>)
- 1559 Siebert, L. (1984). Large volcanic debris avalanches: Characteristics of source areas,  
 1560 deposits, and associated eruptions. *Journal of Volcanology and Geothermal Re-*  
 1561 *search*, *22*, 163-197. ([https://doi.org/10.1016/0377-0273\(84\)90002-7](https://doi.org/10.1016/0377-0273(84)90002-7))
- 1562 Sillitoe, R. (2010). Porphyry copper systems. *Economic Geology*, *105*, 3-41.  
 1563 (<https://doi.org/10.2113/gsecongeo.105.1.3>)
- 1564 Skarbek, R., & Savage, H. (2019). RSFit3000: A MATLAB GUI-based program for  
 1565 determining rate and state frictional parameters from experimental data. *Geo-*  
 1566 *sphere*, *15*, 1665-1676. (<https://doi.org/10.1130/GES02122.1>)
- 1567 Skempton, A. (1964). Long-term stability of clay slopes. *Géotechnique*, *14*, 77-102.  
 1568 (<https://doi.org/10.1680/geot.1964.14.2.77>)
- 1569 Stelling, P., Shevenell, L., Hinz, N., Coolbaugh, M., Melosh, G., & Cumming, W.  
 1570 (2016). Geothermal systems in volcanic arcs: Volcanic characteristics and  
 1571 surface manifestations as indicators of geothermal potential and favorability  
 1572 worldwide. *Journal of Volcanology and Geothermal Research*, *324*, 57-72.  
 1573 (<https://dx.doi.org/10.1016/j.jvolgeores.2016.05.018>)
- 1574 Stimac, J., Goff, F., & Goff, C. (2015). Intrusion-related geothermal systems. In  
 1575 H. Sigurdsson (Ed.), *The Encyclopedia of Volcanoes* (p. 799-822). Academic  
 1576 Press.
- 1577 Stimac, J., Nordquist, G., Suminar, A., & Sirad-Azwar, L. (2008). An overview  
 1578 of the Awibengkok geothermal system, Indonesia. *Geothermics*, *37*, 300-331.  
 1579 (<https://dx.doi.org/10.1016/j.geothermics.2008.04.004>)
- 1580 Summers, R., & Byerlee, J. (1977). A note on the effect of fault gouge compo-  
 1581 sition on the stability of frictional sliding. *International Journal of Rock*  
 1582 *Mechanics and Mining Sciences & Geomechanics Abstracts*, *14*, 155-160.  
 1583 ([https://doi.org/10.1016/0148-9062\(77\)90007-9](https://doi.org/10.1016/0148-9062(77)90007-9))
- 1584 Tembe, S., Lockner, D., & Wong, T. (2010). Effect of clay content and mineralogy  
 1585 on frictional sliding behavior of simulated gouges: Binary and ternary mixtures  
 1586 of quartz, illite, and montmorillonite. *Journal of Geophysical Research*, *115*.  
 1587 (<https://doi.org/10.1029/2009JB006383>)

- 1588 Tesei, T., Carpenter, B., Giorgetti, C., Scuderi, M., Sagy, A., Scarlato, P., & Collet-  
1589 tini, C. (2017). Friction and scale-dependent deformation processes of large  
1590 experimental carbonate faults. *Journal of Structural Geology*, *100*, 12-23.  
1591 (<https://doi.org/10.1016/j.jsg.2017.05.008>)
- 1592 Tesei, T., Collettini, C., Carpenter, B., Viti, C., & Marone, C. (2012). Frictional  
1593 strength and healing behavior of phyllosilicate-rich faults. *Journal of Geophysi-  
1594 cal Research*, *117*. (<https://doi.org/10.1029/2012JB009204>)
- 1595 Teufel, L. (1989). *Influence of lithology and geologic structure on in situ stress: Ex-  
1596 amples of stress heterogeneity in reservoirs* (No. DE89 014692).
- 1597 Townend, J., & Zoback, M. (2000). How faulting keeps the crust  
1598 strong. *Geology*, *28*, 399-402. ([https://doi.org/10.1130/0091-  
7613\(2000\)28<399:HFKTCS>2.0.CO;2](https://doi.org/10.1130/0091-<br/>1599 7613(2000)28<399:HFKTCS>2.0.CO;2))
- 1600 Verati, C., Lardeaux, J., Favier, A., Corsini, M., Philippon, M., & Legendre, L.  
1601 (2018). Arc-related metamorphism in the Guadeloupe archipelago (Lesser An-  
1602 tilles active island arc): First report and consequences. *Lithos*, *320*, 592-598.  
1603 (<https://doi.org/10.1016/j.lithos.2018.08.005>)
- 1604 Verati, C., Mazabraud, Y., Lardeaux, J., Corsini, M., Schneider, D., Voituz,  
1605 E., & Zami, F. (2016). Tectonic evolution of Les Saintes archipelago  
1606 (Guadeloupe, French West Indies): Relation with the Lesser Antilles  
1607 arc system. *Bulletin de la Société Géologique de France*, *187*, 3-10.  
1608 (<https://doi.org/10.2113/gssgfbull.187.1.3>)
- 1609 Verati, C., Patrier-Mas, P., Lardeaux, J., & Bouchot, V. (2014). Timing of geother-  
1610 mal activity in an active island-arc volcanic setting: First  $^{40}\text{Ar}/^{39}\text{Ar}$  dat-  
1611 ing from Bouillante geothermal field (Guadeloupe, French West Indies). In  
1612 F. Jourdan, D. Mark, & C. Verati (Eds.), *Advances in  $^{40}\text{Ar}/^{39}\text{Ar}$  Dating: from  
1613 Archeology to Planetary Sciences* (p. 285-295). Geological Society.
- 1614 Violay, M., Gibert, B., Mainprice, D., Evans, B., Dautria, J., Azais, P., & Pezard,  
1615 P. (2012). An experimental study of the brittle-ductile transition of basalt  
1616 at oceanic crust pressure and temperature conditions. *Journal of Geophysical  
1617 Research*, *117*. (<https://doi.org/10.1029/2011JB008884>)
- 1618 Violay, M., Giorgetti, C., Cornelio, C., Aeschiman, F., Di Stefano, G., Gastaldo, L.,  
1619 & Wiemer, S. (2021). HighSTEPS: A high strain temperature pressure and  
1620 speed apparatus to study earthquake mechanics. *Rock Mechanics and Rock  
1621 Engineering*, *54*, 2039–2052. (<https://doi.org/10.1007/s00603-021-02362-w>)
- 1622 Volpe, G., Collettini, C., Taddeucci, J., Marone, C., & Pozzi, G. (2024). Fric-  
1623 tional instabilities in clay illuminate the origin of slow earthquakes. *Science  
1624 Advances*, *10*. (<https://doi.org/10.1126/sciadv.adn0869>)
- 1625 Volpe, G., Pozzi, G., & Collettini, C. (2022). Y-B-P-R or S-C-C'? Sug-  
1626 gestion for the nomenclature of experimental brittle fault fabric in  
1627 phyllosilicate-granular mixtures. *Journal of Structural Geology*, *165*.  
1628 (<https://doi.org/10.1016/j.jsg.2022.104743>)
- 1629 Walkey, W., & Swanberg, C. (1990). Newberry Volcano, Oregon: New data supports  
1630 conceptual hydrologic model. *Geothermal Resources Council Transactions*, *14*,  
1631 743-748.
- 1632 Wang, J., Jung, W., Li, Y., & Ghassemi, A. (2016). Geomechan-  
1633 ical characterization of Newberry Tuff. *Geothermics*, *63*, 74-96.  
1634 (<https://dx.doi.org/10.1016/j.geothermics.2016.01.016>)
- 1635 Wileveau, Y., Cornet, F., Desroches, J., & Blumling, P. (2007). Complete in situ  
1636 stress determination in an argillite sedimentary formation. *Physics and Chem-  
1637 istry of the Earth*, *32*, 866-878. (<https://dx.doi.org/10.1016/j.pce.2006.03.018>)
- 1638 Wong, I., Pezzopane, S., Dober, M., & Terra, F. (2010). *Evaluations of induced  
1639 seismicity/seismic hazards and risk for the Newberry Volcano EGS Demonstra-  
1640 tion*.
- 1641 Wyering, L., Villeneuve, M., Wallis, I., Siratovich, P., Kennedy, B., Grav-  
1642 ley, D., & Cant, J. (2014). Mechanical and physical proper-



- 1643 ties of hydrothermally altered rocks, Taupo Volcanic Zone, New  
1644 Zealand. *Journal of Volcanology and Geothermal Research*, 288, 76-93.  
1645 (<https://dx.doi.org/10.1016/j.jvolgeores.2014.10.008>)
- 1646 Yagupsky, D., Barcelona, H., Vigide, N., & Lossada, A. (2023). Effects  
1647 of structural zonation on fluids circulation of the Copahue geother-  
1648 mal system. *Journal of South American Earth Sciences*, 125.  
1649 (<https://doi.org/10.1016/j.jsames.2023.104310>)
- 1650 Yamaya, Y., Alanis, P., Takeuchi, A., Cordon, J., Mogi, T., Hashimoto, T., ... Na-  
1651 gao, T. (2013). A large hydrothermal reservoir beneath Taal Volcano (Philip-  
1652 pines) revealed by magnetotelluric resistivity survey: 2D resistivity modeling.  
1653 *Bulletin of Volcanology*, 75. (<https://doi.org/10.1007/s00445-013-0729-y>)
- 1654 Zaiss, R. (2014). *Project NumeriSud SPHAERA-GEO, Géoréférencement et*  
1655 *mosaïquage des cartes de l'IRD. Bondy, France.*
- 1656 Zhang, F., Huang, R., An, M., Min, K., Elsworth, D., Hofmann, H., & Wang, X.  
1657 (2022). Competing controls on effective stress variation and chloritization  
1658 on friction and stability of faults in granite: Implications for seismicity trig-  
1659 gered by fluid injection. *Journal of Geophysical Research: Solid Earth*, 127.  
1660 (<https://doi.org/10.1029/2022JB024310>)
- 1661 Zoback, M., & Townend, J. (2001). Implications of hydrostatic pore pressures and  
1662 high crustal strength for the deformation of intraplate lithosphere. *Tectono-*  
1663 *physics*, 336, 19-30. ([https://doi.org/10.1016/S0040-1951\(01\)00091-9](https://doi.org/10.1016/S0040-1951(01)00091-9))
- 1664 Zoback, M., Townend, J., & Grollmund, B. (2002). Steady-state failure equilib-  
1665 rium and deformation of intraplate lithosphere. *International Geology Review*,  
1666 44, 383-401. (<https://doi.org/10.2747/0020-6814.44.5.383>)